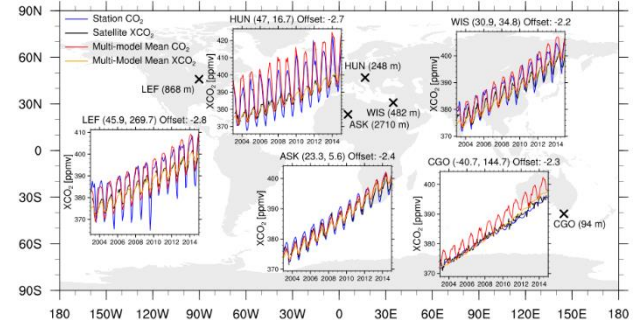
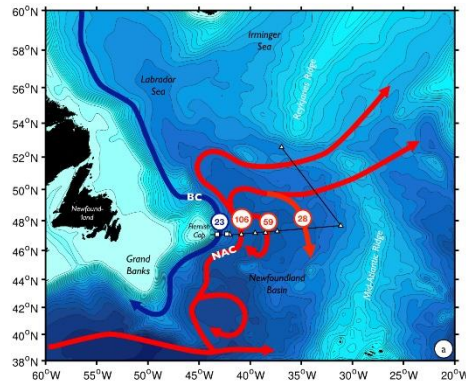
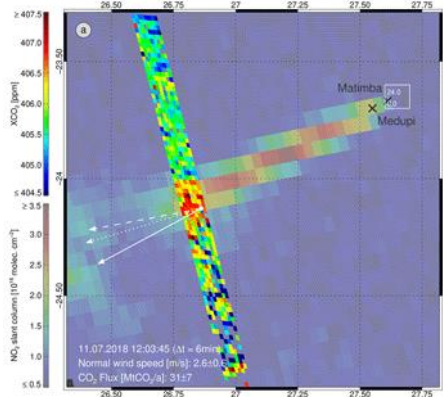
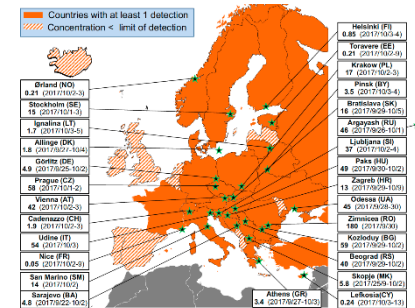
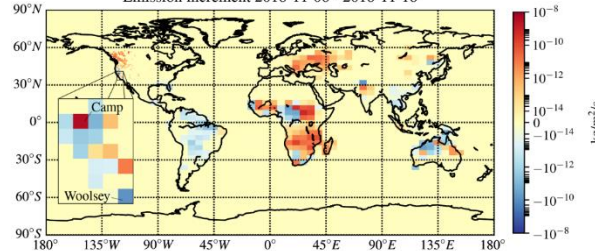


IUP Bremen Research Highlights 2019/2020



Emission increment 2018-11-06 - 2018-11-18



Institute of Environmental Physics (IUP)
 Institute of Remote Sensing (IFE)
 University of Bremen
 Otto-Hahn-Allee 1, 28359 Bremen, Germany

Table of Contents

| | |
|--|-----------|
| INTRODUCTION | 4 |
| REMOTE SENSING OF THE EARTH SYSTEM (PROF. DR. JUSTUS NOTHOLT) | 7 |
| THE TOTAL CARBON COLUMN OBSERVING NETWORK (TCCON) | 7 |
| PARTICIPATION IN EU INFRASTRUCTURE ACTRIS | 8 |
| INSTALLATION OF A NOVEL FTIR INSTRUMENT FOR EMISSION MEASUREMENTS IN NY-ÅLESUND | 9 |
| RIVERS IN THE CARBON CYCLE | 10 |
| MODEL STUDIES ON VIBRATIONALLY-ROTATIONALLY EXCITED HYDROXYL MOLECULES IN THE MESOPAUSE REGION | 11 |
| CHEMICAL IMPACT OF SPRITES | 12 |
| MOSAIC – THE INTERNATIONAL ARCTIC DRIFT EXPEDITION: REMOTE SENSING OF SEA ICE | 13 |
| JOINT RETRIEVAL OF EIGHT SEA ICE AND ATMOSPHERE PARAMETERS FOR THE UPCOMING COPERNICUS CIMR SATELLITE MISSION | 15 |
| SEA ICE TYPE IN THE ANTARCTIC | 17 |
| IMPROVED WATER VAPOUR RETRIEVAL FROM AMSU-B/MHS SATELLITE SENSORS IN THE ARCTIC | 19 |
| PHYSICS AND CHEMISTRY OF THE ATMOSPHERE (PROF. DR. JOHN P. BURROWS) | 21 |
| UNDERWATER LIGHT ATTENUATION IN THE GLOBAL OCEAN FOR THREE SPECTRAL REGIONS: ULTRAVIOLET TO BLUE | 21 |
| CARBON MONOXIDE FROM SENTINEL-5-PRECURSOR: CALIFORNIAN WILDFIRES IN NOVEMBER 2018 | 23 |
| METHANE LEAKAGE FROM NATURAL GAS AND OIL FIELDS | 24 |
| GLOBAL MONITORING OF ATMOSPHERIC CARBON DIOXIDE (CO ₂) | 25 |
| EMISSIONS FROM CO ₂ EMISSION HOT SPOTS SUCH AS POWER PLANTS AND CITIES | 26 |
| IUP-BREMEN CONTRIBUTIONS TO A FUTURE SYSTEM RELEVANT FOR THE PARIS CLIMATE AGREEMENT | 27 |
| UNEXPECTED LONG-RANGE TRANSPORT OF GLYOXAL AND HCHO FROM WILDFIRES OBSERVED BY TROPOMI | 28 |
| LONG-TERM TIME SERIES OF ARCTIC TROPOSPHERIC BRO AND ITS RELATION TO FIRST-YEAR SEA ICE | 30 |
| HORIZONTAL INHOMOGENEITIES IN NO ₂ CONCENTRATIONS ABOVE A SHIPPING LANE OBSERVED USING GROUND-BASED MAX-DOAS MEASUREMENTS | 32 |
| AMBAE VOLCANIC ERUPTION OBSERVED BY THE OMPS-LP INSTRUMENT | 34 |
| SOLAR VARIABILITY | 36 |
| THE UNUSUAL STRATOSPHERIC ARCTIC WINTER 2019/2020: RECORD OZONE LOSS | 38 |
| MOLECULAR SPECTROSCOPY IN SUPPORT OF EARTH REMOTE SENSING | 39 |
| DERIVATION OF STRATOSPHERIC AEROSOL EXTINCTION PROFILES FROM SCIAMACHY SOLAR OCCULTATION MEASUREMENTS | 42 |
| RETRIEVAL OF AEROSOL OPTICAL THICKNESS AND SURFACE PARAMETERS BASED ON MULTI-SPECTRAL AND MULTI-VIEWING SPACE-BORNE MEASUREMENTS | 44 |
| RETRIEVAL OF AEROSOL OPTICAL THICKNESS IN THE ARCTIC SNOW-COVERED REGIONS USING PASSIVE REMOTE SENSING | 45 |
| EXTENDING REMOTE SENSING RETRIEVALS TO AEROSOL AND CLOUD CONDITIONS | 46 |
| GREENHOUSE GAS OBSERVATIONS FROM AIRCRAFT: TOWARDS THE NEXT GENERATION OF THE METHANE AIRBORNE MAPPER | 47 |
| TRANSPORT OF ATMOSPHERIC POLLUTION ORIGINATING IN EUROPEAN MAJOR POPULATION CENTRES | 49 |

| | |
|---|-----------|
| INVERSE MODELLING OF THE EARTH SYSTEM (PROF. DR. MIHALIS VREKOUSSIS) | 51 |
| ASSESSING THE IMPACT OF NATURAL DUST ON AIR QUALITY USING TM4-ECPL..... | 51 |
| ASSESSMENT OF THE IMPACT OF OH'S TEMPORAL RESOLUTION ON THE GLOBAL ATMOSPHERE..... | 53 |
| ENHANCING CHEMICAL SCHEMES ACCOUNTED IN FLEXPART v10.4 TRANSPORT MODEL USING A KINETIC PRE-PROCESSOR..... | 55 |
| COMBINING HERMESv3 AND TM5-MP..... | 57 |
| TOP-DOWN CO EMISSION INVERSIONS USING TM5-4DVAR AND TROPOMI..... | 59 |
| CLIMATE MODELLING (PROF. DR. VERONIKA EYRING) | 61 |
| RELEASE OF THE EARTH SYSTEM MODEL EVALUATION TOOL (ESMVALTOOL) VERSION 2.0..... | 61 |
| SPATIALLY RESOLVED EVALUATION OF EARTH SYSTEM MODELS WITH SATELLITE COLUMN AVERAGED CO ₂ | 63 |
| MACHINE LEARNING FOR PROCESS-ORIENTED CLIMATE MODEL EVALUATION | 65 |
| PHYSICAL OCEANOGRAPHY (PROF. DR. MONIKA RHEIN) | 67 |
| HEAT AND FRESHWATER TRANSPORT BY MESOSCALE EDDIES IN THE SOUTHERN SUBPOLAR NORTH ATLANTIC | 67 |
| INTERANNUAL AND DECADEAL VARIABILITY OF VOLUME AND FRESHWATER TRANSPORT OF THE NAC IN THE SUBPOLAR GYR | 69 |
| WIND-DRIVEN INTERNAL GRAVITY WAVES..... | 71 |
| HYDROTHERMAL PLUME STUDIES USING NOBLE GAS ISOTOPES | 72 |
| SENSITIVITY OF LABRADOR SEA WATER FORMATION TO CHANGES IN MODEL RESOLUTION, ATMOSPHERIC FORCING, AND FRESHWATER INPUT | 74 |
| DECAY OF INTERNAL TIDES | 75 |
| OBSERVED TRANSPORT DECLINE AT 47°N IN THE WESTERN NORTH ATLANTIC..... | 78 |
| TERRESTRIAL ENVIRONMENTAL PHYSICS (DR. HELMUT FISCHER) | 80 |
| THE TERRESTRIAL ENVIRONMENTAL PHYSICS GROUP AT UNIVERSITY OF BREMEN | 80 |
| BLUE CARBON STUDIES IN INDONESIA | 80 |
| ORIGIN OF ATMOSPHERIC RU-106 OVER EUROPE | 81 |
| MODELLING THE PARTITIONING OF RADIONUCLIDES IN AGRICULTURAL SOILS | 83 |
| TEACHING ACTIVITIES | 85 |

Introduction

The IUP comprises six departments: Remote Sensing, Physics and Chemistry of the Atmosphere, Oceanography, Terrestrial Environmental Physics, Modelling and Observation of the Earth System and Climate Modelling.

The **Department of Remote Sensing (Prof. J. Notholt)** employs passive remote sensing instrumentation such as Fourier transform interferometers and microwave radiometers taking measurements in the spectral region from the infrared to the microwave. The instruments are located at various ground based sites ranging from the high Arctic (Svalbard) to the tropics (Suriname), as well as aboard research vessels (R.V. Polarstern) and aircraft. In addition, the gas exchange between rivers or the biosphere on land and the atmosphere is studied using spectroscopic methods. Furthermore, operational satellite instruments are used to monitor atmospheric and earth surface properties. Among them are sea ice coverage, water vapour and clouds. A further research focus is the investigation of stratospheric and mesospheric processes including solar effects on the terrestrial atmosphere. These activities are supported by atmospheric modelling.

The research activities carried out in the **Department of Physics and Chemistry of the Atmosphere (Prof. J.P. Burrows)** aim at improving the understanding of the complex physical chemical processes in the atmosphere and its interfaces to land, ocean, ice, and deep space. Emphasis is placed on the impact of anthropogenic and natural changes on the composition of the troposphere, stratosphere, and mesosphere, including greenhouse gases, pollutants and reactive gases. A particular focus has been the scientific development and support of satellite sensors to characterise the chemical composition of the atmosphere remotely by means of spectroscopy in the ultraviolet, visible and near-infrared spectral regions using grating spectrometers. The department pioneered this re-

search area with the GOME and SCIAMACHY sensors, as well as with the development of future satellite sensor concepts for geostationary air pollution observations (GeoSCIA, now Sentinel-4) and dedicated greenhouse gas sensors (CarbonSat, now COM2M). Similar instruments are operated from the ground (NDACC stations, BRE-DOM network), on ships (R.V. Polarstern), aircrafts and balloons. Remote sensing is complemented by in-situ experiments, laboratory work on spectroscopy and reaction kinetics, as well as modelling of physical and photochemical processes in the lower, middle and upper atmosphere.

Research of the **Department of Oceanography (Prof. M. Rhein)** focuses on climate relevant processes in the ocean. These encompass the circulation, formation, and transformation changes in key regions of the Atlantic and the associated changes in the storage of anthropogenic carbon. The identification and the role of submarine melt water from Greenland and Antarctic ice shelves for the ocean dynamics is an emerging research field as well as the energy transfer and mixing in the ocean through internal waves. We improve and develop methods to quantify the basin-wide current systems, and we improve trace gas analysis techniques and expand their interpretation in the ocean and in groundwater dating studies. The department mainly works with experimental methods and coordinates, leads, and participates in several research cruises per year mainly with the vessels MERIAN, METEOR, and POLARSTERN. The research is part of two Collaborative Research Centres (CRC 181

IUP Mission Statement

The overarching objective of the Institute of Environmental Physics is to understand the mechanisms controlling the Earth System and its response to change. This is achieved by using physical methods and research focuses on the sub systems atmosphere, ocean, cryosphere, and their interfaces. This requires the development and use of remote sensing techniques from the ground, from ships, aircraft and satellite platforms and in-situ measurements for process studies. The data are coupled with models to interpret the observations and improve the prediction of change.

and 172) and other national and European programmes (www.ocean.uni-bremen.de).

The **Department of Terrestrial Environmental Physics (Dr. H. Fischer)** investigates transport processes in porous systems and soils and conducts research in the fields of radioecology and sediment chronology. It takes advantage of the excellent equipment available in the Bremen State Radioactivity Measurements Lab (which forms part of the state and federal nuclear emergency management networks) and of a unique Earth Field NMR apparatus. Due to staff reduction and retirement of the leader, the group is currently inactive and its future is unclear.

Since 2016, the **Department of Inverse Modelling of the Earth System (Prof. M. Vrekoussis)** hosts the joint IUP-MARUM working group called LAMOS (Laboratory for Modelling and Observation of the Earth System). LAMOS aims at improving our understanding of the complex mechanisms controlling the emission, transport, transformation and deposition of atmospheric pollutants with the use of state-of-the-art numerical models and novel instrumentation. Special focus is given on the quantification of sources and sinks of long-lived and short-lived species using satellite observations as proxies.

The **Department of Climate Modelling (Prof. V. Eyring)** established at the IUP in 2017 develops innovative methods for the evaluation and analysis of Earth system models in comparison to observations. This enables synergies and direct collaboration with the observational departments of the IUP. The evaluation and ensemble analysis of Earth system models is crucial for model improvements and a prerequisite for reliable climate projections of the 21st century to be used as guidelines for climate policy. In collaboration with the Department on “Earth System Model Evaluation and Analysis” of the German Aerospace Centre’s Institute of Atmospheric Physics (DLR-IPA), the Climate Modelling Department provides major contributions to the Coupled Model Intercomparison Project (CMIP) and to the development of the Earth System Model Evaluation Tool

(ESMValTool). A new focus is the development and application of machine learning techniques to better understand and model the Earth system. This includes the development of machine learning based parameterisations for Earth system models that have hindered progress in climate modelling for decades. It also includes research to understand modes of climate variability and multivariate extremes with novel deep learning and causal discovery techniques, as well as research to constrain uncertainties in Earth system feedbacks and multi-model climate projections with observations.

The IUP is internationally well known for its initiation and participation in a number of advanced space-borne missions, in particular GOME and SCIAMACHY. Both sensors were proposed by the IUP, and the IUP acts as Principal Investigator. The Global Ozone Monitoring Experiment, GOME, which was the first satellite sensor to measure tropospheric trace constituents from space and has operated aboard ERS-2 for over 10 years. GOME is a smaller version of SCIAMACHY, which was launched successfully in 2002 and also has provided almost a decade of successful data. The GOME and SCIAMACHY data records are now continued by GOME-2, OMI, and Sentinel-5P/TROPOMI, as well as in the future by Sentinel-4 and Sentinel-5. IUP scientists are contributing actively to all those missions. The IUP is also involved in many international projects with space-borne instruments for remotely measuring greenhouse gases and surface parameter, such as sea ice, the Wadden Sea and land use. In addition, the IUP runs instrumentation at research measurement stations worldwide. It has participated in many national and international research campaigns using ships, aircrafts and ground-based instruments. Members of the IUP are actively involved in international scientific organisations like COSPAR, IGBP-IGAC, WCRP-SPARC, CACGP and WMO-IGACO.

The complexity of the environmental system on Earth requires a coordinated approach of various scientific disciplines. Special focus

is placed on investigations to quantify the impact of human activity on the Earth system and to separate it from natural effects.

More than 100 Ph.D. students and postdocs work at the IUP. Students in general physics have the option to specialize in environmental physics. A variety of courses, conducted in cooperation with colleagues from the Alfred-Wegener-Institute Helmholtz Centre for Polar and Maritime Research (AWI) in Bremerhaven is offered at the IUP. The aim of the environmental physics course is to provide a basic education in the areas of the ocean, the atmosphere and the solid Earth. Whereas other German universities cover parts of environmental physics, for example physical oceanography or meteorology, as independent subjects, Bremen addresses all of them within the physics course fully integrated into the general physics. The students even have the opportunity to participate in exciting expeditions worldwide. To strengthen environmental physics as a course of study in its own right and also to motivate students from abroad to study in Bremen, a four-semester international course leading to a Master of Science (M.Sc.) in Environmental Physics and a two-semester postgraduate course for the Certificate in Environmental Physics have been offered since autumn 2000. The IUP educational activities were further developed towards space applications with the new international and application oriented Masters Programme **Space Sciences and Technologies**. It covers the three basic technologies Remote Sensing, Processing and Communication. The Programme provides theoretical knowledge in the fields of Remote Sensing, Earth Observation, Retrieval Theory, Electronics and Communications a solid hands-on training.

This document provides an overview of selected research highlights achieved by the members of the five IUP departments during the period 2019/2020.

Department contacts



Physics and Chemistry of the Atmosphere
Prof. Dr. John P. Burrows FRS
+49-421-218 62100
burrows@iup.physik.uni-bremen.de



Remote Sensing
Prof. Dr. Justus Notholt
+49-421-218-62190
jnotholt@iup.physik.uni-bremen.de



Oceanography
Prof. Dr. Monika Rhein
+49-421-218-62160
mrhein@physik.uni-bremen.de



Terrestrial Environmental Physics
Dr. Helmut Fischer, retired
+49-421-218-62761
hfischer@physik.uni-bremen.de



Laboratory for Modelling and Observation
of the Earth System
Prof. Dr. Mihalis Vrekoussis
+49-421-218-62140
vrekoussis@iup.physik.uni-bremen.de



Climate Modelling
Prof. Dr. Veronika Eyring
+49-421-218-62733
Email: veronika.eyring@uni-bremen.de

The Total Carbon Column Observing Network (TCCON)

Thorsten Warneke, Christof Petri, Matthias Buschmann, Mihalis Vrekoussis, and Justus Notholt

The increase of the atmospheric greenhouse gases carbon dioxide (CO₂) and methane (CH₄) results in an increase of global surface temperatures. Consequences of the temperature increase are already visible and severe consequences are predicted for the future, among them sea level rise, change of weather patterns, extreme weather events, extinction of certain wildlife species and the spread of diseases.

The increase of CO₂ in the atmosphere can be directly assigned to anthropogenic activities. Each year several gigatons of CO₂ are emitted into the atmosphere by human activities. Fortunately, only about 50% of the emitted CO₂ remains in the atmosphere and thus contributes to global warming. The other 50% are taken up by natural sinks - the terrestrial biosphere and the ocean. Methane (CH₄), the second most important anthropogenic greenhouse gas after CO₂, is emitted from highly variable and not well understood sources such as

wetlands, rice fields, landfills, oil- and gas-exploration and ruminants.

In order to reliably predict the future climate of our planet, a good understanding of the sources and sinks of CO₂ and CH₄ is mandatory. Unfortunately, there are large gaps in our understanding of the natural sources and sinks of these gases. Key questions to be answered are: Where are the natural and anthropogenic sources and sinks? How strong are they? What are their characteristics? How will they respond to a changing climate?

The basis for understanding the atmospheric greenhouse gas budgets and answering the questions above are precise measurements of atmospheric CO₂ and CH₄. The global atmospheric observing system for greenhouse gases consists of in-situ measurements as well as ground-based and space-born remote sensing measurements. While high quality in-situ measurements are available since almost 60 years, the technically challenging remote sensing measurements of CO₂ and CH₄ became available only 10 years ago. In contrast to the in-situ measurements, remote sensing measurements measure through the whole atmosphere and satellites provide global coverage.

The Total Carbon Column Observing Network (TCCON) represents the ground-based remote-sensing component in the global atmospheric observing system for greenhouse gases. It has been established in 2004. At that time, it consisted of five sites: two in Europe, one in the US and two in Oceania. The only European founding member of TCCON was the Institute



Figure 1: TCCON-observatory at the University of Bremen



Figure 2: Installation of the TCCON instrument at the Cyprus Institute in Nicosia.

of Environmental Physics at the University of Bremen, operating the two European sites at Ny-Ålesund (Spitsbergen) and Bremen (Germany). Nowadays, the TCCON comprises more than 20 globally distributed sites and has established itself as a vital component in the global observing system for green-

house gases. The University of Bremen is currently operating four TCCON sites at the locations Ny-Ålesund (Spitsbergen), Bremen (Germany), Orleans (France) and Nicosia (Cyprus). The latter site has been installed in 2019 and is operated in a close collaboration with the Cyprus Institute.

Participation in EU infrastructure ACTRIS

Matthias Palm and Justus Notholt

The MIDIR (MID InfraRed) group of the AG Notholt of the IUP participates in the EU infrastructure ACTRIS (Aerosols Clouds Tracegases Research InfraStructure¹, www.actris.net). The aim of ACTRIS is to provide high quality data of short-lived atmospheric constituents. ACTRIS will provide effective access to a wide user community to its services and resources.

The MIDIR group is part of the ACTRIS topical centre CREGARS (Center for REactive trace GAses Remote Sensing) and will offer training in operation of FTIR instruments and take part in the quality management of ACTRIS facilities employing FTIR spectrometers.

The MIDIR group furthermore is part of the ACTRIS-D consortium with the planned installation or upgrading of three FTIR facilities:

The FT spectrometer Bremen will be upgraded to enable automatic measurements. This will increase the number of measurements considerably.

The FT spectrometer in Paramaribo, Suriname, will be upgraded and the measurement station will be renewed and upgraded.

A mobile facility will be newly built. The MIDIR group uses the rich body of experience available in the AG Notholt in the set up and operation of remote FT instrument stations.

The FTIR station in Ny-Ålesund will be labelled as a fully qualified station.

The data will be available via the ACTRIS data centre starting from 2025.

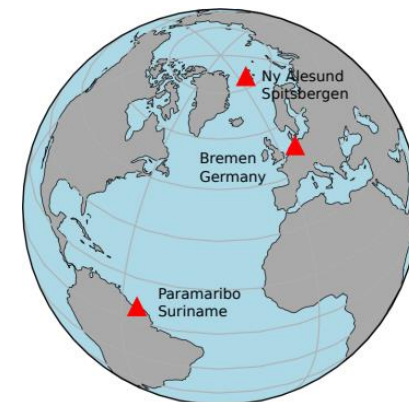


Figure 3: ACTRIS FTIR measurement stations operated by the University of Bremen in the EU infrastructure ACTRIS

Installation of a novel FTIR instrument for emission measurements in Ny-Ålesund

Mathias Palm, Matthias Buschmann, and Justus Notholt

In the AWIPEV research base (www.awipev.eu) in Ny-Ålesund, Spitzbergen the MIDIR group installed a novel FT instrument to measure downwelling infrared radiation.

The advantage of FTIR emission spectrometry is the ability to measure in the dark, i.e. during the polar night. Trace gas measurements of CO₂, CH₄ and O₃ will contribute to the understanding the seasonal cycle of those gases and fill the gaps in solar and lunar absorption measurements. Especially greenhouse gas measurements are still burdened by the lack of high quality total column measurements at the poles. CH₄ is

potent modulators of atmospheric and surface warming in the Arctic because of their ability to radiate back longwave radiation in the infrared. Thin clouds are known to have a large effect, but are still not well quantified. Emission FT spectrometry offers a way to permanently and automatically monitor the abundances of thin clouds.

This investigation will contribute to the DFG Transregio TR-172, "Arctic Amplification" (Wendisch et al., 2019) and the recorded data will be used in combination with data obtained during the MOSAIC campaign, which took place from August 2019 to August 2020.

References

Wendisch, M. et al., The Arctic Cloud Puzzle: Using ALOUD/PASCAL Multiplatform Observations to Unravel the Role of Clouds and Aerosol Particles in Arctic Amplification, BULLETIN OF THE AMERICAN METEOROLOGICAL SOCIETY, 2019, 100 841-872, 2019.

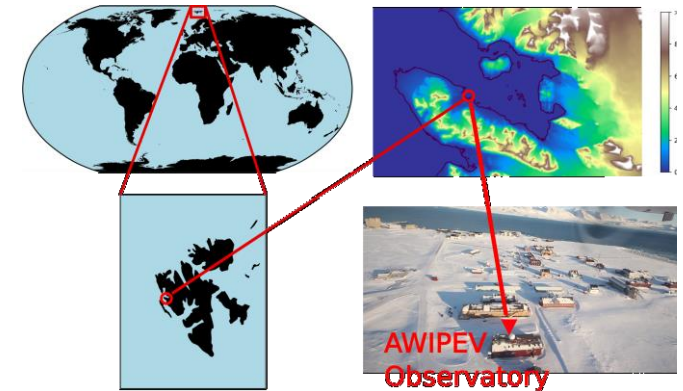


Figure 4: Location of the AWIPEV station in Ny-Ålesund

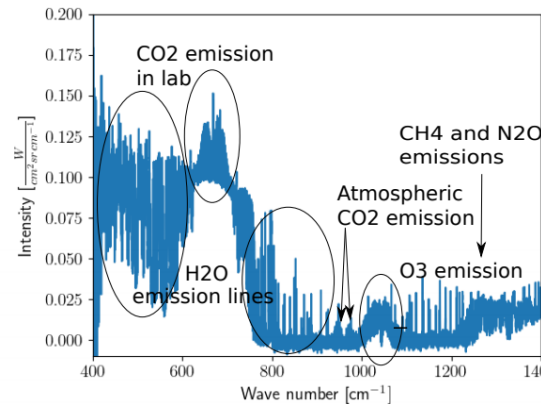


Figure 5: Atmospheric emission spectrum taken in Ny-Ålesund, Spitzbergen

potentially released in large quantities by thawing of the Permafrost and by the ocean.

Additionally the measurements will be used to infer thin cloud and aerosol properties. Clouds are

Rivers in the carbon cycle

Thorsten Warneke, Alexandra Klemme, Denise Müller, and Justus Notholt

The carbon cycle describes the exchange of carbon between different reservoirs. The fast component of the carbon cycle, which is relevant for the understanding of anthropogenic climate change, describes the exchange of carbon between the land, the ocean and the atmosphere. Rivers play an important role by transporting carbon from the land to the ocean. The processing of carbon in rivers as well as the exchange of carbon between the rivers and the atmosphere represent large uncertainties in carbon cycle modelling. Recent studies suggest that rivers play a crucial role for carbon processing and storage, as well as greenhouse gas emissions and are therefore highly important for the establishment of regional carbon balances.

One recent focus of our research are peat-draining rivers in Southeast Asia. Southeast Asian peatlands store about 68.5 gigatons of carbon, which corresponds roughly to the amount of carbon emitted to the atmosphere by fossil fuel burning within 8 years. This large carbon store is currently under high pressure due to anthropogenic activity. The conversion of tropical peat swamp forest to plantations (mainly oil palm) upsets both the water and the carbon balance in the peat soil. As a result, carbon that has been stored for centuries is lost to the atmosphere or the adjacent aquatic system. Consequently, rivers transporting peat-derived carbon might be a mirror of the degree of disturbance in tropical peat ecosystems.

Since the vast majority of peatlands in SE-Asia is located close to the coast and many peatlands are drained by short rivers, the carbon is rapidly transported to the coastal ocean. We have investigated a river that drains an intact peat dome in Sarawak (Borneo, Malaysia). The entire river catchment is

covered by peat swamp forest. Though such a scenario is relatively unique, it is ideally suited for a baseline study. Such baseline data is vital for the interpretation of carbon fluxes from disturbed peat areas.

The dissolved organic carbon concentrations in the river draining the undisturbed peatland are among the highest reported in the literature. The age of the dissolved organic carbon transported by the river was less than ten years, which shows that it is not derived from the peat-column, but from recently fixed biomass. Despite the very high organic carbon loads, the emission of CO₂ from the river to the atmosphere is not unusually high, but comparable to other tropical rivers. Most likely, this is a result of the short residence time of the carbon in the river, which is typical for peat-draining rivers in SE-Asia.

This research is done in close cooperation with the Leibniz Center for Tropical Marine Ecology (ZMT) in Bremen, because the study regions as well as the instrumentation from ZMT and IUP perfectly complement each other.

References

D. Müller, T. Warneke, T. Rixen, M. Müller, S. Jahari, N. Denis, A. Mujahid, and J. Notholt: Lateral carbon fluxes and CO₂ outgassing from a tropical peat-draining river. *Biogeosciences*, 12, 5967-5979, 2015. doi:10.5194/bg-12-5967-2015.

F. Wit, D. Müller, A. Baum, T. Warneke, W. Setiyo Pranowo, M. Müller, and T. Rixen. The impact of disturbed peatlands on river outgassing in Southeast Asia. *Nature Communications* 6, 10155, 2015. doi:10.1038/ncomms10155.

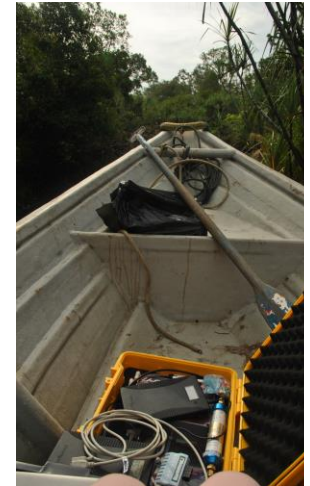


Figure 6: Sampling trip on a small peat-draining river in Sarawak (Borneo, Malaysia)

Model studies on vibrationally-rotationally excited hydroxyl molecules in the mesopause region

Holger Winkler and Justus Notholt

One of the standard methods to remotely sense the temperature of the mesopause region (80-90 km height region) is based on spectroscopic measurements of near-infrared emissions of vibrationally-rotationally excited hydroxyl (OH) molecules, and to calculate rotational temperatures. For the interpretation of the retrieved temperatures, the aspect of rotational thermalization is of great importance. We use a first-principle kinetic model of vibrationally-rotationally excited OH which accounts for chemical production and loss processes as well as radiative and collision-induced vibrational-rotational transitions. The model allows one to assess deviations of the rotational populations from local thermodynamic equilibrium, and to identify the key parameters, which control the rotational thermalization processes.

Figure 7 shows a comparison of model results and data originating from the UVES (Ultraviolet and Visual Echelle Spectrograph) at Cerro Paranal in Chile. The model simulations reproduce the observed bimodality in temperatures, i.e. a cold temperature component dominating the population of low rotational states, and a hot temperature component dominating higher states. Model-measurement comparisons can be used to determine unknown physical parameters. For instance, the best fit between model and measurement data in Figure 7 is obtained if the model allows for a change of the rotational quantum number in vibrational quenching processes.

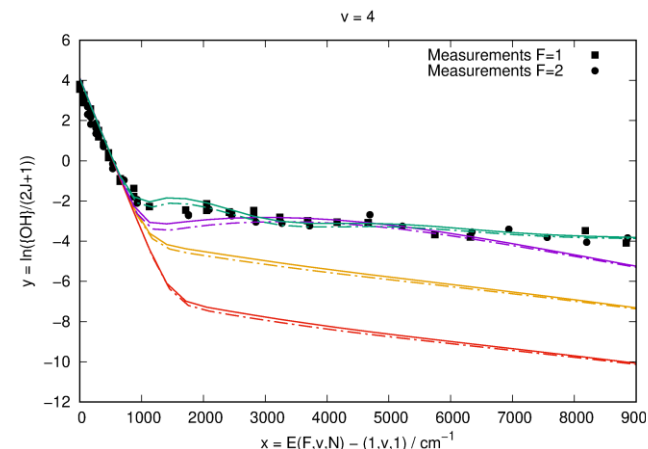


Figure 7: Logarithm of the rotational population (divided by the degeneracy $2J+1$ of the rotational state) as a function of rotational energy (for vibrational quantum number $v=4$; $F=1$ and $F=2$ depict the spin-doublet states). A thermal Boltzmann distribution would result in a straight line. Different lines show model results with different quenching parameters.

Reference

S. Noll, H. Winkler, O. Goussev, and B. Proxauf: OH level populations and accuracies of Einstein-A coefficients from hundreds of measured lines, *Atmos. Chem. Phys.*, 20, 5269–5292, <https://doi.org/10.5194/acp-20-5269-2020>, 2020.

Chemical impact of sprites

Holger Winkler and Justus Notholt

The so called sprites are large scale electrical discharges which occur above active thunderstorm clouds. The chemical effects of such events are not well understood. Recently, measurements by the SMILES (Superconducting Submillimeter-Wave Limb Emission Sounder) satellite instrument have shown an increase of mesospheric HO_2 above sprite producing thunderstorms. These are the first direct observations of chemical sprite effects, and provide an opportunity to test our understanding of the processes in sprites. We have developed a numerical model of the plasma chemical processes in electrical discharges. It was coupled to a one-dimensional transport module and used to simulate a downward propagating sprite streamer at altitudes 70-80 km corresponding to one of the sprite events observed by the SMILES instrument. The model simulations show a production of hydrogen radi-

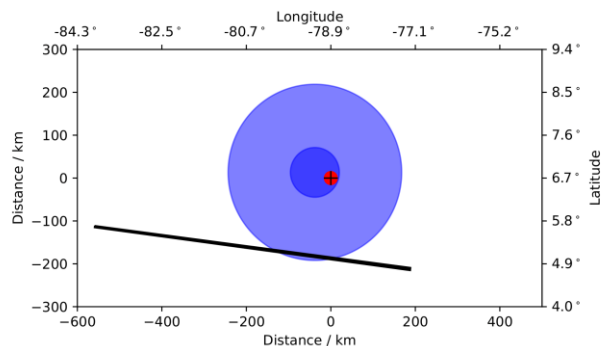


Figure 9: Results of a sprite transport and dispersion simulation. The red circle depict the initial sprite cross sections. The blue circles show the sprite cross sections at the times of the SMILES measurements. The large/small blue circles correspond to a fast/slow diffusion scenario. The black areas show the fields of view of the SMILES measurements.

icals mainly due to reactions of proton hydrates ($\text{H}^+(\text{H}_2\text{O})_n$) formed a few seconds after the electrical discharge. The net effect is a conversion of water molecules into $\text{H} + \text{OH}$. This leads to increasing HO_2 concentrations a few hours after the electric breakdown. However, the modelled total production of HO_2 by a single sprite is much too small to explain the measured HO_2 enhancements. Additionally, advection and dispersion simulations of the observed sprite bodies reveal that in most cases only little overlap of the expanded sprite volumes and the field of view of the SMILES measurements is expected. A possible explanation could be that there was an accumulation of HO_2 produced by a number of different sprites near the SMILES measurement volume. This is subject of ongoing research.

Reference:

Winkler, H., Yamada, T., Kasai, Y., Berger, U., and Notholt, J.: Model simulations of chemical effects of sprites in relation with satellite observations, *Atmos. Chem. Phys. Discuss.*, <https://doi.org/10.5194/acp-2020-1228>, 2021.

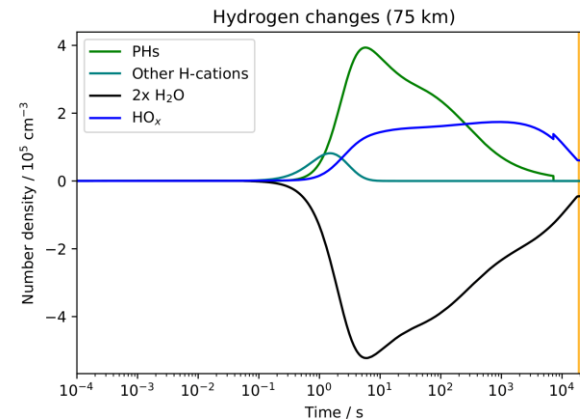


Figure 8: Evolution of the modelled amount of hydrogen atoms contained in selected species at 75 km altitude. Shown are differences between a sprite model run and a model run without electric discharge. PHs denotes all hydrogen atoms in proton hydrates. The teal solid line depicts all hydrogen-bearing positive ions except for proton hydrates

MOSAiC – The International Arctic Drift Expedition: Remote Sensing of Sea Ice

Gunnar Spreen, Marcus Huntemann, and Linda Thielke

For MOSAiC, the Multidisciplinary drifting Observatory for the Study of Arctic Climate, the research icebreaker Polarstern was frozen in the Arctic sea ice in October 2019 close to the North Pole north of the Laptev Sea and drifting with the sea ice for one complete year until September 2020. Compared to previous years the ice drift was fast and, in particular in winter, the drift trajectory was quite straight from the Russian Arctic towards Fram Strait. Thus, the MOSAiC floe disintegrated in Fram Strait end of July 2020 and Polarstern was relocated further north to finish the ice drift at a new floe. MOSAiC is an international Arctic drift expedition with more than 400 scientists, experts, and crew members on the ship and institutes from 20 nations involved. Research covered a wide range of topics from the atmosphere, sea ice and ocean domains and feedbacks with the ecological and biogeochemical systems. Interdisciplinarity is at the heart of MOSAiC with the overarching goal to improve Arctic and global climate models.

The one-year long drift, however, also presented an excellent opportunity to evaluate current satellite remote sensing observations and develop new remote sensing methods. While the research icebreaker Polarstern was drifting with the sea ice several remote sensing instruments designed for observing the sea ice and its snow cover were installed on the ice floe next to Polarstern and on the vessel itself. This, for the first time, allowed the monitoring of the freeze-up to melt onset cycle and different ice types with the suite of instruments. The remote sensing instruments have counterparts in space, and their

measurements are designed to enhance understanding of the interaction of electromagnetic waves with snow and sea ice. Satellite measurements constitute a few of the most important climate data records for polar regions, e.g., the more than 40-year long record of global sea ice area from space-borne microwave radiometers, which shows its unprecedented decline in the Arctic in recent decades.

The IUP has a long-standing history in satellite sea ice remote sensing of sea ice, especially with microwave radiometers. The working group for *Remote Sensing of Polar Regions* joined the expedition with three group members on legs 1, 2 and 5 (Figure 10). Dr. Gunnar Spreen is member of the MOSAiC project board and coordinator of the remote sensing activities. Other groups at IUP were involved in the oceanographic and atmosphere measurements. The IUP sea ice remote sensing program consisted of helicopter-borne and on-ice infrared thermal imaging systems, hyperspectral and optical cameras and, in collaboration with ESA and other partners, the HUTRAD multi-frequency, dual polarization microwave radiometer. HUTRAD will help to develop sea ice remote sensing methods for the upcoming Copernicus CIMR satellite mission, which the IUP is involved in.



Figure 10: Linda Thielke and Gunnar Spreen waving to a passing group of scientists while making L-band microwave and infrared radiometer measurements together with the according ice thickness on thin ice on 30 September 2020 (photo: Jan Rhode).

In addition, several institutions from Spain, Canada, UK, Switzerland, Finland, and the US provided instrumentation in collaboration with space agencies ESA, NASA, and EUMETSAT. The combination of the MOSAiC remote sensing experiments will help to improve the quality and better assess the uncertainties of satellite observations. In particular the following measurements were performed during MOSAiC on the ice floe: (i) microwave radiometer observations at 0.5–2, 1.4, 7, 11, 19, 37, and 89 GHz frequencies in dual polarization, (ii) fully-polarimetric, microwave radar scatterometer observations at L-, C-, X-, Ku-, and Ka-band frequencies, (iii) reflected single- and dual-polarized GNSS measurements from snow and ice, and (iv) infrared, visual, and hyperspectral cameras. This is the largest

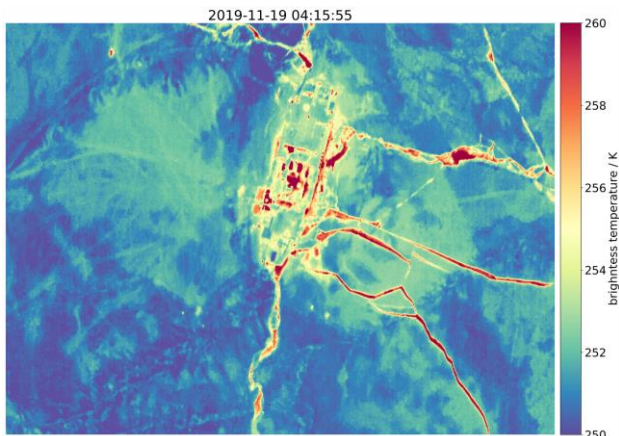


Figure 12: Infrared-Camera image during the helicopter flight on 19 November 2019. The colors show the measured infrared brightness temperature. The ship is clearly visible from its warmer structures. Cracks in the ice with warmer temperatures are caused by a storm on Nov 17. Dark blue, colder areas show thicker and ridged ice. In the vicinity of the ship features like snow mobile tracks with slightly higher temperature occur due to snow compaction.

collection of remote sensing instruments ever brought out on sea. Figure 11 shows the Remote Sensing Site at the beginning and end of the expedition. The instruments on the ice floe were oriented to observe

similar snow and ice conditions. The remote sensing measurements were accompanied by extensive measurements of snow and ice properties in the vicinity of the measurement field. By having these coincident multi-frequency remote sensing and in-situ observations and as well the environmental conditions measured by other MOSAiC teams, factors influencing the emission, reflection, and scattering of microwaves in sea ice and snow can be better understood so that new remote sensing methods can be developed.

Two helicopters were available on Polarstern throughout the campaign. Their measurements will help to better understand the regional characteristics of the sea ice and snow surrounding Polarstern and help to upscale the local on-ice measurement to a satellite footprint size. The primary helicopter instruments were an airborne laser scanner to observe the ice topography and freeboard height and an infrared camera (provided by IUP; Figure 12) to observe the ice surface temperature distribution and development of cracks and leads in the ice pack. After day-light came back also ice thickness measurements by electromagnetic induction and a hyperspectral camera were operated.

All these measurements will not only help to better understand climate changes in the Arctic but will also help to improve current and contribute to new and upcoming satellite missions.



Figure 11 The MOSAiC Remote Sensing Site at the beginning of the experiment on 8th December 2019 (top; photo: Stefan Hendricks) and at the end on 8th September 2020 (bottom; photo: Gunnar Spreen). In between several relocations of the site took place, e.g., because of sea ice dynamics and destruction of the site. However, some of the instruments were operational almost the complete year.

Joint Retrieval of Eight Sea Ice and Atmosphere Parameters for the Upcoming Copernicus CIMR Satellite Mission observations

Raul Scarlat, Gunnar Spreen, Georg Heygster, Marcus Huntemann, Cătălin Pațilea, Leif Toudal Pedersen, and Roberto Saldo

Most current sea ice satellite retrievals provide one specific parameter like ice concentration, ice type, or ice thickness. Combining them is often difficult because they are not consistent between each other. However, multi-frequency satellite microwave radiometers offer the opportunity to retrieve these parameters simultaneously taking also atmospheric parameters like water vapour and cloud liquid water into account. Such consistent multi-parameter observational datasets are especially useful for initializing and tuning climate models. This is especially true in the Polar Regions where uncertainties about the interactions between sea ice, ocean, and atmosphere are large. Here we combine observations of the existing AMSR2 and SMOS microwave radiometers. In future, a new Sentinel satellite series with the Copernicus Imaging Microwave Radiometer (CIMR) on board will provide high resolution, low uncertainty observation capabilities at the same 1.4, 6.9, 10.65, 18.7, and 36.5 GHz frequencies.

An optimal estimation retrieval method (OEM) is used (Scarlat et al., 2020) which can use input from different AMSR2 channel combinations to retrieve seven geophysical parameters (sea ice concentration [SIC], multi-year ice fraction [MYIF], ice [IST] and sea [SST] surface temperatures, columnar water vapour [TWV], liquid water path [LWP], and wind speed [WSP]) (Figure 13). After we evaluated the original seven parameter OEM, we extended it by thin sea ice thickness (SIT) as eighth parameter using SMOS L-band observations (Figure 13).

The sea ice concentration (SIC) OEM retrieval performance of different channel combinations was tested over a dataset of validated SIC conditions (Figure 14).

The 6.9 GHz based retrieval offers with about 2% the lowest possible retrieval standard deviation (STD) over both 100% SIC (SIC1) and open water scenes (SIC0) but also has the lowest spatial resolution. The 18.7+36.5 GHz combination achieves less than 5% mean STD. The CIMR 18.7+36.5 GHz channels will have a similar spatial resolution of about 5 km as the 89 GHz channels of AMSR2, which is the highest spatial resolution for SIC retrieval today. However, the 89 GHz mean STD

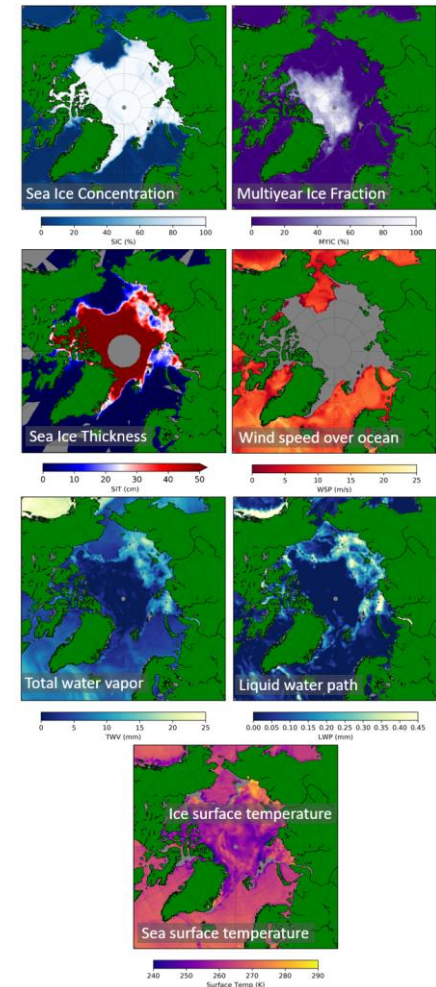


Figure 13: Example result for multi-parameter AMSR2 based OEM (06.11.2019; mind that IST and SST are combined in one map). The sea ice thickness shown here is retrieved from SMOS directly, but in future will also be part of the operational OEM output.

of 12% is much higher for AMSR2 compared to the <5% for CIMR (Figure 14). This is mainly due to the stronger atmospheric influence at 89 GHz.

The 18.7+36.5 GHz version offers a 70% to 30% split between surface (SIC, MYIF) and atmospheric parameters, i.e., overall a good compromise between information content and resolution. The higher spatial resolution of the low frequency CIMR channels allow for unprecedented detail to be achieved in Arctic passive microwave sea ice retrievals.

The presence of 1.4 GHz channels on board CIMR opens up the possibility for thin sea ice thickness (SIT) retrieval. A combination of collocated AMSR2 and SMOS observations is used to simulate a full CIMR suite of measurements, and the OEM is modified to include SIT as a retrieval parameter. The output from different retrieval configurations is compared with an operational SMOS SIT (Hunte-

mann et al., 2014).

Empirical functions are developed and implemented in the OEM forward model for connecting SIT with brightness temperatures for all CIMR channels. This allows SIT to be retrieved after inverting the forward model. One disadvantage of current SMOS only SIT retrievals is the missing sea ice concentration (SIC) information, which can affect the SIT retrieval. If only the SMOS 1.4 GHz channels are used in the OEM the comparison (Figure 16, left) shows a negative SIC bias for low SIT pixels (thin sea ice mistaken for thick ice and a larger open water fraction). Using all channels in the OEM configuration shows better agreement (Figure 16, right) with the operational product than 1.4 GHz alone (while also retrieving the other seven OEM parameters at the same time including SIC).

In summary, the future Copernicus Sentinel CIMR satellite mission will provide increased accuracy for sea ice concentration retrieval at high spatial resolutions of 5 km with a combination of the 18.7 and 36.5 GHz channels while also maintaining sensitivity for atmospheric water vapour retrieval. In combination with the on-board 1.4 GHz channels, thin ice thickness can be added as an eighth retrieval parameter with performance on par with existing operational products.

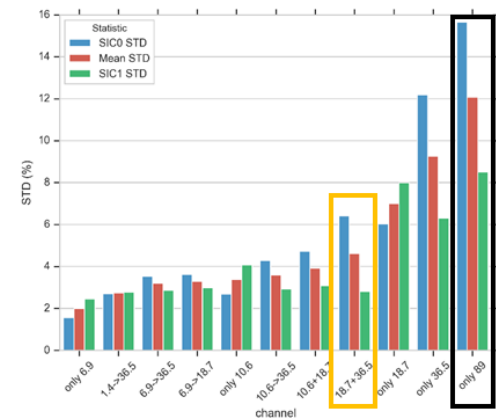


Figure 14: Ranking by SIC retrieval uncertainty (expressed by the STD) of different channel combinations. At 5 km spatial resolution current SIC retrievals have an uncertainty of about 12% using the 89 GHz channels (black box) while the future CIMR mission can provide SIC with <5% uncertainty based on the 18.7 and 36.5 GHz channels (orange box). Note the maximum ice thickness retrieved is 50 cm and for dates when that thickness is reached the actual mean thickness is likely to be higher.

Information content comparison for four OEM versions

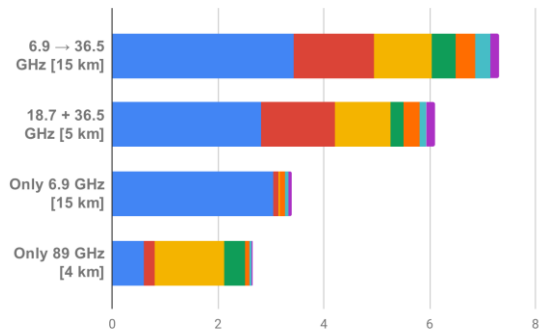


Figure 15: Information content for retrievals using four different channel combinations. The total length of the bars indicates total information content, while the length of individual color sections shows information content for a single parameter. The spatial resolution for the future CIMR is noted in square brackets, at 89 GHz the current AMSR2 resolution is given.

References

Scarlat, R. C., Spreen, G., Heygster, G., Huntemann, M., Patilea, C., Pedersen, L. T., Saldo, R., Sea ice and atmospheric parameter retrieval from satellite microwave radiometers: Synergy of AMSR2 and SMOS compared with the CIMR candidate mission. *Journal of Geophysical Research: Oceans*, 125, e2019JC015749. doi:10.1029/2019JC015749, 2020.

Huntemann, M., Heygster, G., Kaleschke, L., Krumpen, T., Mäkynen, M., Drusch, M., Empirical sea ice thickness retrieval during the freeze-up period from SMOS high incident angle observations, *The Cryosphere*, 8, 439–451, doi:10.5194/tc-8-439-2014, 2014

Sea ice type in the Antarctic

Christian Melsheimer and Gunnar Spreen

Sea ice is one of the Earth's climate components that has shown the greatest change during the last decades. As sea ice has high albedo, its changes affect the global radiation balance. Furthermore, sea ice controls energy and gas fluxes between ocean and atmosphere in Polar Regions, and it is an important part of the polar marine ecosystem. Satellite observations, which start in the 1970s, show that while the sea ice area in the Arctic is decreasing at a rate of about -4% per decade, the sea ice area in the Antarctic has slowly increased by about 1% per decade. However, in order to understand the ongoing and possibly future changes, it is not sufficient to just monitor the sea ice area or extent because sea ice comes in different types which have quite different physical properties and which can react differently to changes. The three major types are young ice (YI; newly formed and thin), first-year ice (FYI; formed during one freezing season) and multiyear ice (MYI; having survived at least one melt season). In the Arctic, the sea ice decline has been particularly drastic for MYI, at about -13% per decade. For the Antarctic, however, not much is known about the different ice

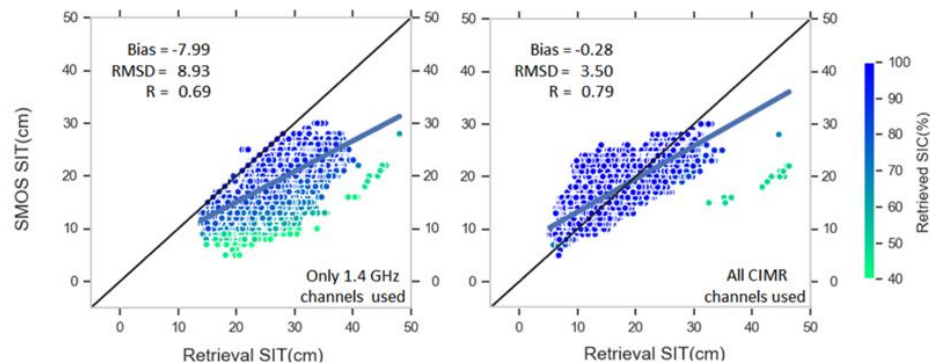


Figure 16: OEM retrieved SIT using only 1.4 GHz channels (left) and all CIMR equivalent channels (right), respectively, compared with the operational SMOS SIT product (x-axis). The marker color represents the simultaneously retrieved SIC value.

types. Therefore, we have adapted a recent satellite-based retrieval of sea-ice types, originally developed for the Arctic [Ye et al., 2016a,b], for use in Antarctic conditions. This retrieval can distinguish YI, FYI and MYI during the freezing season.

The retrieval uses input data from radar scatterometer and microwave radiometers and in addition corrects for the effects of melt–refreeze cycles during the transition seasons, snow metamorphosis and sea-ice drift. In order to distinguish the ice types, the algorithm needs information on their typical emission and backscatter behaviour in the channels used. For this, areas of known ice type were analysed. The input channels used are the radar backscatter (C-Band, VV polarisation) of the scatterometer ASCAT on the European Metop satellites and the brightness temperature (radiance) at three channels of the microwave radiometer AMSR2 on the Japanese satellite GCOM-W1, namely, at 37 GHz V and H polarisation, and 19 GHz, V polarisation. The above-mentioned corrections use, in addition, the air temperature near the ground from meteorological reanalysis data and sea ice drift data from satellite.

With this algorithm, the first circumpolar, long-term time series of Antarctic sea ice types (MYI, first-year ice and young ice) is being established, so far covering the years 2013-2020. As an example, the concentrations (i.e., area fractions) of the three ice types are shown early in the freezing season (3 March 2016, Figure 17) and late in the freezing season (11 August 2016, Figure 18). The figures show how the ice that remained at the end of the melting season, mainly in the Southern Weddell Sea, is MYI at the beginning of the freezing season (Figure 17, left). Figure 18 shows that the MYI has now drifted northwards and that Antarctica is surrounded by mainly FYI that has formed since the beginning of the freezing season. YI ice can be seen at the outer edge of the ice where there is ice growth, and in some places along the coast where it forms on polynyas, i.e. opening in the sea ice caused by strong katabatic winds blowing offshore from the continent. In addition, there is a large area of YI (and a large “gap” in the FYI) in the Eastern Weddell Sea, where in 2016, the unusual Weddell Sea polynya had just occurred in the weeks before that day.

The new retrieval for the first time allows insight into the evolution and dynamics of Antarctic sea ice types. The current time series can be extended backwards to the year 2002 and can be continued with current and future sensors.

References

Ye, Y., M. Shokr, G. Heygster, G. Spreen, Improving multiyear ice concentration estimates with ice drift. *Remote Sens.*, 8(5), 397, doi:10.3390/rs8050397, 2016a.

Ye, Y., G. Heygster, M. Shokr, Improving multiyear ice concentration estimates with air temperatures. *IEEE Trans. Geosci. Remote Sens.*, 54(5), 2602–2614, doi:10.1109/TGRS.2015.2503884, 2016b.

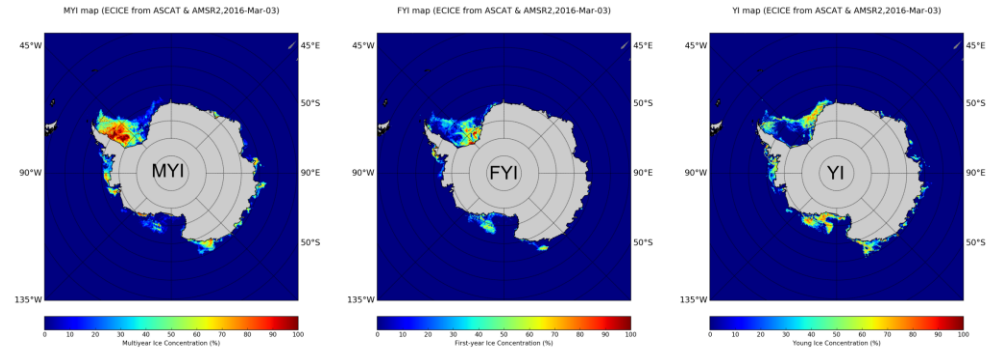


Figure 17: Maps of the Antarctic sea ice type concentrations on 3 March, 2016, i.e., beginning of freezing season. Left: multiyear (MYI), middle: first-year (FYI), right: young ice (YI).

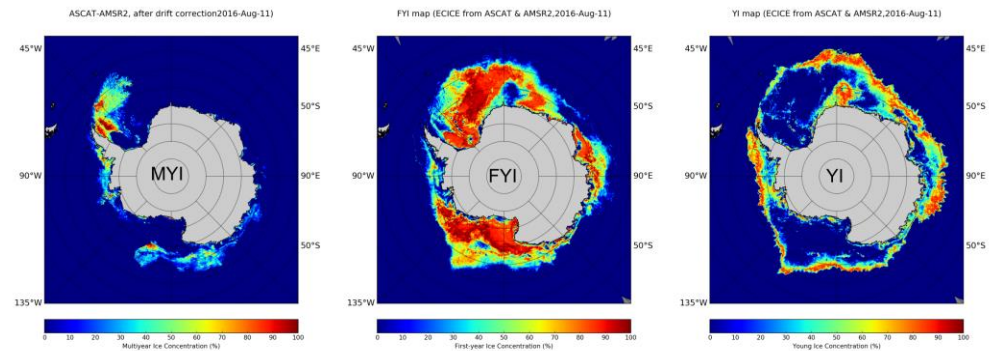


Figure 18: Maps of the Antarctic sea ice type concentrations on 11 August, 2016, i.e., late in the freezing season. Left: corrected MYI, middle: FYI, right: YI. Note that the large “hole” in the FYI (middle) in the Eastern Weddell Sea (on the top side of the continent) and the large are of YI at the same location marks the unique 2016 Weddell Sea Polynya.

Improved Water Vapour Retrieval from AMSU-B/MHS Satellite Sensors in the Arctic

Arantxa M. Triana-Gómez, Georg Heygster, Christian Melsheimer, and Gunnar Spreen

Monitoring of water vapour in the Arctic on long time scales is essential for predicting Arctic weather and understanding climate trends, as well as addressing its influence in the positive feedback loop contributing to Arctic Amplification. However, standard in-situ measurements such as radiosondes are sparse in the region, and standard satellite remote-sensing retrieval methods for total water vapour (TWV) face several problems in Arctic conditions: cloud cover, which restricts infrared measurements, and incomplete understanding of the high and highly variable sea-ice emissivity, which challenges microwave measurements.

A step forward for Arctic water vapour retrieval was achieved by Melsheimer and Heygster (2008) and recently Triana-Gómez et al. (2020). The algorithm uses microwave radiometer satellite measurements from humidity sounders such as AMSU-B or MHS on board the NOAA (National Oceanic and Atmospheric Administration) 15 to 19 satellites and EUMETSAT (European Organisation for the Exploitation of Meteorological Satellites) Metop-A, Metop-B and Metop-C satellites. The key concept of this method is the use of several microwave channels with similar surface emissivity but different water vapour absorption. These are the three channels near the 183.31 GHz water absorption line (183.31 1, 3 and 7 GHz), which, together with the channels at the 89 GHz and 150 GHz window frequencies, allows the retrieval to function up to the saturation limit of the 183.31 7 GHz channel, about 20 kg/m². However, the original AMSU-B algorithm is not without problem: while the frequency range allows it to bypass most clouds, the AMSU-B sen-

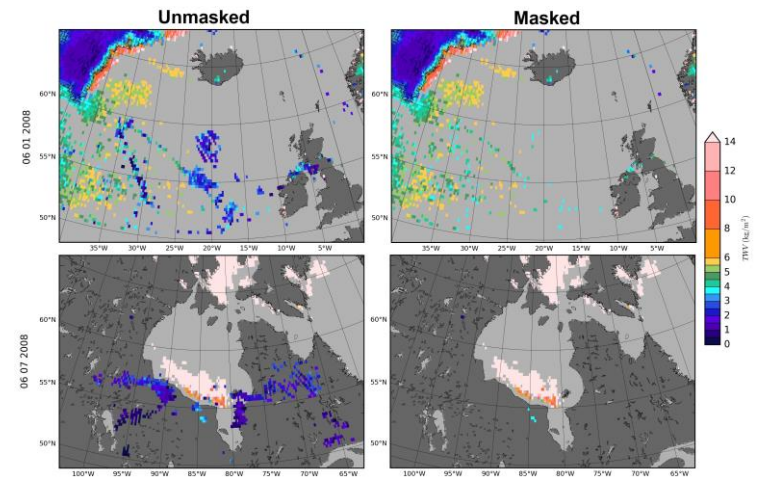


Figure 19: Unmasked (left) and masked (right) AMSU-B TWV retrieval for different showcased areas of four days through 2008: 6 January (top), 2 April (middle up), 6 July (middle down) and 14 October (bottom). Please note the different location in each case.

sor is still sensitive to convective clouds with high ice content. A method to filter these artefacts has been developed by Triana-Gómez et al. (2020). Additionally, the algorithm originally used as input only microwave humidity sounder data from AMSU-B. The updated algorithm can now also use data from MHS, the successor instrument of AMSU-B.

Since cloud ice particles are strong scatterers in the used microwave range, the radiation from below the clouds is scattered strongly and hardly reaches the sensor, so that the AMSU-B retrieval is only sensitive to atmospheric water vapour above such clouds and retrieves erroneously low TWV. Cloud ice contents high enough to affect our TWV retrieval are almost entirely caused by strong convective clouds, which are typically organised in rather small-scale cells (tens of kilometres to at maximum of a few hundred kilometres for polar lows). Therefore, image-processing methods that rely on the size of ice cloud artefacts can be used: Our approach for eliminating the affected TWV is to find connected areas of low TWV (<4 kg/m²) which are surrounded by higher TWV

values. Then, we remove these connected areas with a succession of morphological image processing operations. To visualize the areas affected by the ice cloud artefact Figure 19 shows different areas of interest before (left) and after (right) filtering, for two days in 2008: 6th of January and 6th of July. These areas have been chosen as representative cases for the season. Most features – small regions of low TWV surrounded by high TWV – are removed. We confirmed by comparison to ERA5 atmospheric reanalysis that the remaining high TWV values are within the expected range. Also the high, $>14 \text{ kg/m}^2$, TWV values on 6th July 2008 in the Hudson Bay area are in agreement with ERA5.

We have investigated the impact of differences between the AMSU-B and MHS sensor on the retrieved TWV and have found the differences to be negligible. This means that a consistent continuous data set for the years 1999 until now can be generated from combining AMSU-B and MHS data. Figure 20 shows daily averaged TWV maps – with the ice cloud filtering already applied – for the AMSU-B/MHS algorithm (top and second row), as well as from a different data product based on AMSR-E observations over open ocean (third row) and ERA5 reanalysis daily mean (bottom) in winter (6 January, left) and summer (6 July, right) 2008. The first thing to notice is the difference in spatial coverage of AMSU-B/MHS retrieved TWV between winter and summer. As AMSU-B/MHS retrieval is restricted to the drier regions, in summer retrieval is basically only possible over sea ice and over Greenland (the upper limit of the retrieval is usually about 15 kg/m^2 for sea ice surfaces). In winter, the retrieval is possible over most of the land, sea ice, and some open water areas. The TWV from the ERA5 reanalysis (bottom) agrees well with both AMSU-B/MHS and AMSR-E: all have similar patterns, particularly in winter. Comparison to in-situ TWV measurements using GPS and radiosondes in 2008, 2009, and 2015 show overall good performance of the updated TWV retrieval in Triana-Gómez et al. (2020).

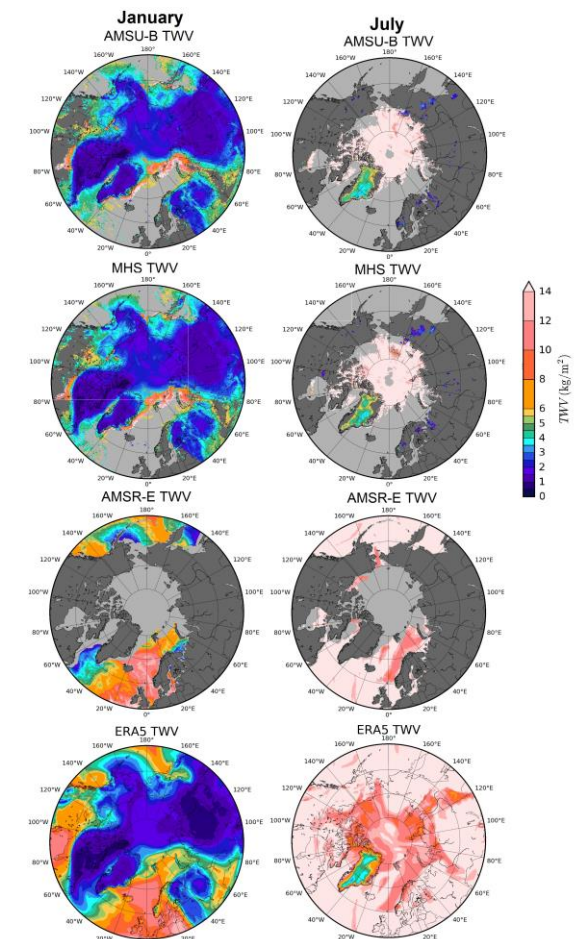


Figure 20: AMSU-B (top), MHS (second row), AMSR-E (third row) and ERA5 (bottom) TWV retrievals for (left) winter (6 January 2008), and (right) summer (6 July 2008)

References

Melsheimer, C. and Heygster, G.: Improved Retrieval of Total Water Vapor Over Polar Regions from AMSU-B Microwave Radiometer Data, *IEEE Trans. Geosci. Rem. Sens.*, 46, 2307–2322, 2008.

Triana-Gómez, A. M., Heygster, G., Melsheimer, C., Spreen, G., Negusini, M., and Petkov, B. H.: Improved water vapour retrieval from AMSU-B and MHS in the Arctic, *Atmospheric Measurement Techniques*, 13, 3697–3715, doi:10.5194/amt-13-3697-2020, <https://amt.copernicus.org/articles/13/3697/2020/>, 2020.

Underwater light attenuation in the global ocean for three spectral regions: ultraviolet to blue

Julia Oelker, Svetlana N. Losa, Andreas Richter, and Astrid Bracher

Solar radiation drives many biological, chemical, and physical processes in the ocean. Ultraviolet (UV) radiation can have both, damaging and beneficial, effects on marine organisms and their interaction within the ocean system is generally complex. Most processes feedback with global warming. Satellite-based observations of light penetration into the ocean in combination with modelling are used to understand these processes and make predictions for the future ocean and climate scenarios in general. Traditional satellite instruments, so-called ocean colour sensors, do not take measurements in the ultraviolet range. From these data sets information on UV light penetration is inferred only indirectly, from measurements in the visible wavelength range which introduces further large uncertainty.

As a cooperation between the Alfred-Wegener-Institute Helmholtz Centre for Polar and Marine Research and the Institute of Environmental Physics at the University Bremen, within the joint ESA Sentinel-5P+ Innovation activity S5POC (Exploitation of Sentinel-5P for Ocean Colour Products), the UV and blue bands of the TROPOMI sensor on board Sentinel-5P were exploited to directly infer diffuse attenuation coefficients of underwater radiation (K_d) in the UV and blue spectral range. Earlier studies applied to similar sensors (SCIAMACHY, GOME-2, OMI – see Vountas et al. 2003, 2007, Dinter et al. 2015, Oelker et al. 2019) have successfully derived K_d in the blue range from the signal caused by inelastic scattering of photons on water molecules. This signal can be detected as filling-in of Fraunhofer lines in

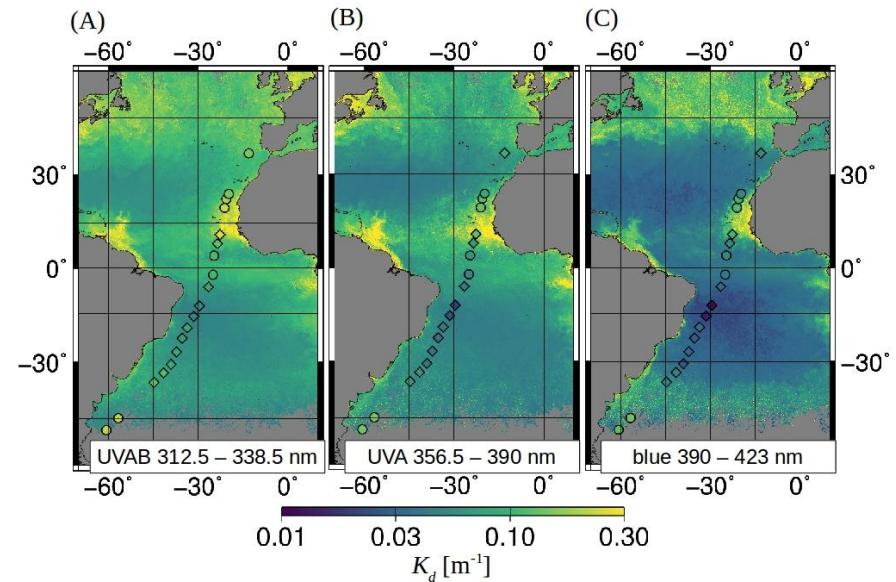


Figure 21: Underwater light attenuation in the Atlantic Ocean retrieved from backscattered radiances of the satellite sensor TROPOMI on board the Sentinel-5 Precursor satellite for three spectral regions: (A) K_d -UVAB (312.5 to 338.5 nm), (B) K_d -UVA (356.5 to 390 nm), and (C) K_d -blue (390 to 423 nm). Data are gridded at 0.083° as mean for the duration of the R/V Polarstern expedition. Overlaid as symbols are the K_d -UVAB, K_d -UVA, and K_d -blue measured in-situ at 19 stations during this expedition. Figure from Oelker et al. (submitted to FMARS).

backscattered radiances recorded at a spectral resolution of around 0.5 nm by TROPOMI-like sensors for targeting atmospheric trace gas concentrations. The approach is based on Differential Optical Absorption Spectroscopy. In combination with simulations by the IUP radiative transfer model SCIATRAN, this method was adapted for the TROPOMI sensor and other spectral regions to obtain two novel K_d products in the UV range (312.5 to 338.5 nm and 356.5 to 390 nm), additionally to the blue K_d (390 to 423 nm). First results for one month of satellite-derived data could be presented which compare well to spectral K_d values measured in-situ during a transatlantic cruise with R/V Polarstern in 2018 by AWI (Figure 21). TROPOMI K_d -blue was compared to wavelength-converted K_d at 490 nm products

from operational ocean colour products (OLCI/Sentinel-3 and the merged data set from the Ocean Colour ESA Climate Change Initiative, OC-CCI). Differences between the three data sets are within uncertainties given for the OC-CCI product.

These new TROPOMI shortwave diffuse attenuation products are provided with spatial resolution and coverage which meets requirements for estimating at global scale heat budget, primary productivity, photochemical reaction rates of climatically important compounds, and UV dose rates as an indicator for damaging effects on aquatic organisms.

References

Oelker J., Losa S. N., Richter A., Bracher A., TROPOMI-retrieved underwater light attenuation in three spectral regions: ultraviolet to blue. Submitted to *Frontiers in Marine Science*, 16 Dec 2020.

Dinter T., Rozanov V., Burrows, J. P., Bracher A., Retrieval of light availability in ocean waters utilizing signatures of vibrational Raman scattering in hyper-spectral satellite measurements. *Ocean Science* 11: 373-389, 2015.

Oelker J., Richter A., Dinter T., Rozanov V. V., Burrows J. P., Bracher A., Global diffuse attenuation coefficient derived from vibrational Raman scattering detected in hyperspectral backscattered satellite spectra. *Optics Express* 27 (12), A829-A855 DOI: 10.1364/OE.27.00A829, 2019.

Vountas, M., Richter, A., Wittrock, F., and Burrows, J. P. , Inelastic scattering in ocean water and its impact on trace gas retrievals from satellite data, *Atmos. Chem. Phys.* 3: 1365-1375, 2003.

Vountas M., Dinter T., Bracher A., Burrows J.P., Sierk B., Spectral Studies of Ocean Water with Space-borne Sensor SCIAMACHY using Differential Optical Absorption Spectroscopy (DOAS). *Ocean Science* 3: 429-440, 2007.

Carbon monoxide from Sentinel-5- Precursor: Californian wildfires in November 2018

Oliver Schneising, Michael Buchwitz, Maximilian Reuter, Heinrich Bovensmann, and John P. Burrows

November 2018 turned into one of the most severe wildfire episodes on record in California, with two particularly destructive wildfires spreading concurrently through the northern and the southern part of California. Both fires ignited at the wildland–urban interface and caused many civilian fatalities, forcing the total evacuation of several cities and communities. We have analysed IUP-Bremen S5P/TROPOMI retrievals of carbon monoxide (CO) (Schneising et al., 2019) to find out to what extent CO emission of these wildfires can be observed and how these observations can be interpreted (Schneising et al., 2020). The derived CO distributions (Figure 22) have been used to assess the corresponding air quality burden in major Californian cities.

References

Schneising, O., Buchwitz, M., Reuter, M., Bovensmann, H., Burrows, J. P., Borsdorff, T., Deutscher, N. M., Feist, D. G., Griffith, D. W. T., Hase, F., Hermans, C., Iraci, L. T., Kivi, R., Landgraf, J., Morino, I., Notholt, J., Petri, C., Pollard, D. F., Roche, S., Shiomi, K., Strong, K., Sussmann, R., Velasco, V. A., Warneke, T., and Wunch, D.: A scientific algorithm to simultaneously retrieve carbon monoxide and methane from TROPOMI onboard Sentinel-5 Precursor, *Atmos. Meas. Tech.*, 12, 6771–6802, <https://doi.org/10.5194/amt-12-6771-2019>, 2019.

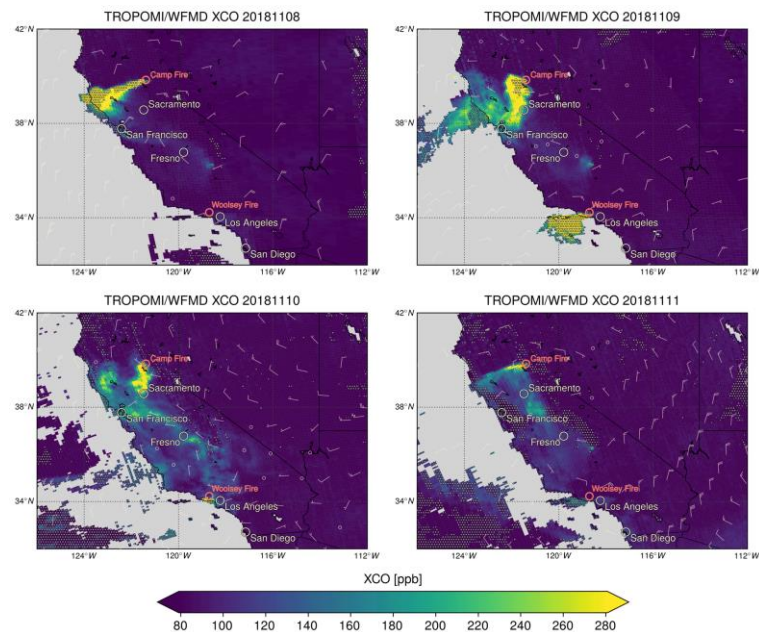


Figure 22: Column-averaged mole fraction of CO, XCO, as retrieved from S5P/TROPOMI for four days in November 2018 over California (source: Schneising et al., 2020).

Schneising, O., Buchwitz, M., Reuter, M., Bovensmann, H., and Burrows, J. P.: Severe Californian wildfires in November 2018 observed from space: the carbon monoxide perspective, *Atmos. Chem. Phys.*, 20, 3317–3332, <https://doi.org/10.5194/acp-20-3317-2020>, 2020.

Methane leakage from natural gas and oil fields

Oliver Schneising, Michael Buchwitz, Maximilian Reuter, Stefan Vanselow, Heinrich Bovensmann, and John P. Burrows

The switch from the use of coal to natural gas or oil for energy generation potentially reduces greenhouse gas emissions and thus the impact of energy production on global warming and climate change because of the higher energy creation per CO₂ molecule emitted. However, the climate benefit of oil and gas over coal is partly offset by methane (CH₄) leakage from natural gas and petroleum systems, which reverses the climate impact mitigation if the rate of fugitive emissions exceeds the compensation point at which the global warming resulting from the leakage and the benefit from the reduction of coal combustion coincide. Consequently, an accurate quantification of CH₄ emissions from the oil and gas industry is essential to evaluate the suitability of natural gas and petroleum as bridging fuels on the way to a carbon-neutral future. We have analysed IUP-Bremen retrievals of column-averaged dry-air mole fractions of CH₄, XCH₄ (Schneising et al., 2020) from the TROPospheric Monitoring Instrument (TROPOMI) onboard the Sentinel-5 Precursor (S5P) satellite to quantify methane emissions and leakage rates from major gas and oil fields as located in the United States and in Turkmenistan (Figure 23).

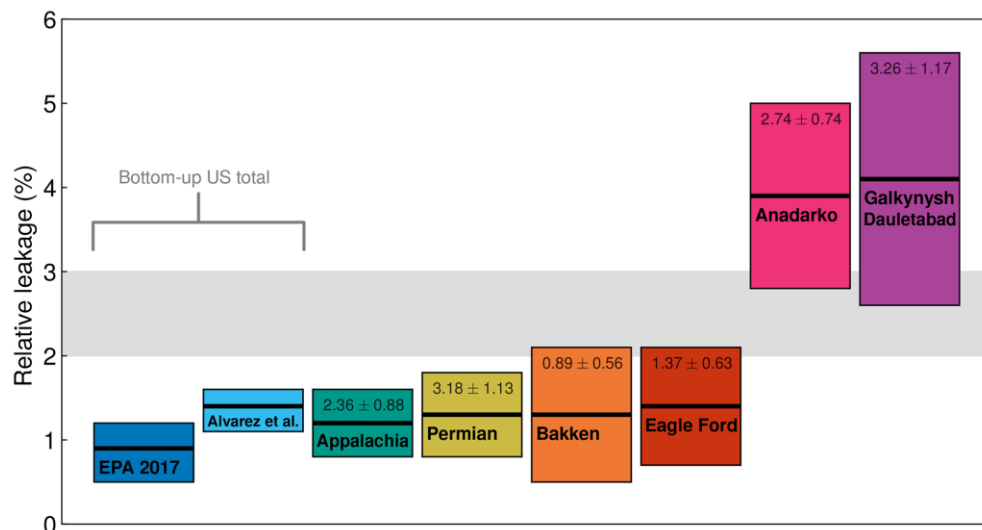


Figure 23: Summary of the results for the different regions analysed in Schneising et al., 2020, and a comparison to bottom-up estimates for the entire United States. All leakage rates are calculated relative to combined oil and gas production in terms of energy content. The respective absolute emissions (MtCH₄/year) are shown in the upper area of the bars for the individual regions. The assumed break-even range for immediate climate benefit is shown in grey (source: Schneising et al., 2020).

Reference

Schneising, O., Buchwitz, M., Reuter, M., Vanselow, S., Bovensmann, H., and Burrows, J. P.: Remote sensing of methane leakage from natural gas and petroleum systems revisited, *Atmos. Chem. Phys.*, 20, 9169–9182, <https://doi.org/10.5194/acp-20-9169-2020>, 2020.

Global monitoring of atmospheric carbon dioxide (CO₂)

Maximilian Reuter, Michael Buchwitz, Oliver Schneising, Stefan Noël, Heinrich Bovensmann, and John P. Burrows

Carbon dioxide (CO₂) is the most important anthropogenic greenhouse gas and the driver for global warming. Atmospheric observations of CO₂ are required for monitoring purposes and to use these observations in combination with inverse modelling to obtain information on natural and anthropogenic CO₂ sources (emissions) and sinks. At IUP-Bremen, several satellite-derived CO₂ data products are generated. Most of these products are near surface sensitive column-averaged dry air mole fractions of CO₂ denoted XCO₂. These products are generated for scientific purposes and for operational services. For example, IUP-Bremen generates XCO₂ from data of the Japanese GOSAT satellite in near-real time for the European Copernicus Atmosphere Monitoring Service (<https://atmosphere.copernicus.eu/>, CAMS) and also generates a multi-satellite merged data product for the Copernicus Climate Change Service (C3S, <https://climate.copernicus.eu/>). The C3S product (Figure 24) can be obtained from the Copernicus Climate Data Store (CDS, <https://cds.climate.copernicus.eu/>), a data base which holds a large number of climate relevant data sets called Essential Climate Variables (ECVs).

The IUP of the University of Bremen is also strongly involved in the specification of improved future satellites in particular for anthropogenic CO₂ monitoring. In this context, the IUP is providing expertise to the European Space Agency (ESA) and the European Commission (EC) for the planned Copernicus candidate CO₂ monitoring (CO2M) mission and IUP member Dr. M. Buchwitz has been selected to be a member of the

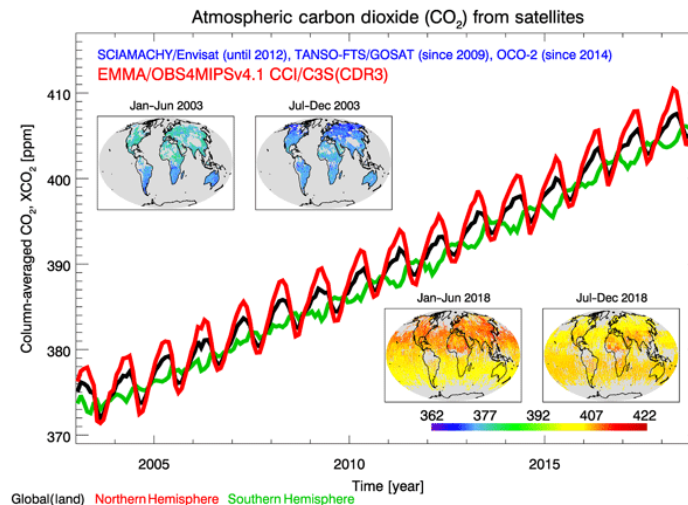


Figure 24: Time series and maps of column-averaged CO₂, XCO₂, as generated at IUP-Bremen for the Copernicus Climate Change Service (C3S) (source: Reuter et al., 2020).

ESA/EU CO2M Mission Advisory Group (MAG). The CO2M mission evolves from the IUP lead CarbonSat initiative.

Reference

Reuter, M., Buchwitz, M., Schneising, O., Noel, S., Bovensmann, H., Burrows, J. P., Boesch, H., Di Noia, A., Anand, J., Parker, R. J., Somkuti, P., Wu, L., Hasekamp, O. P., Aben, I., Kuze, A., Suto, H., Shiomi, K., Yoshida, Y., Morino, I., Crisp, D., O'Dell, C. W., Notholt, J., Petri, C., Warneke, T., Velazco, V. A., Deutscher, N. M., Griffith, D. W. T., Kivi, R., Pollard, D. F., Hase, F., Sussmann, R., Te, Y. V., Strong, K., Roche, S., Sha, M. K., De Maziere, M., Feist, D. G., Iraci, L. T., Roehl, C. M., Retscher, C., and Schepers, D.: Ensemble-based satellite-derived carbon dioxide and methane column-averaged dry-air mole fraction data sets (2003-2018) for carbon and climate applications, *Atmos. Meas. Tech.*, 13, 789-819, <https://doi.org/10.5194/amt-13-789-2020>, 2020.

Emissions from CO₂ emission hot spots such as power plants and cities

Maximilian Reuter, Michael Buchwitz, Oliver Schneising, Sven Krautwurst, Andreas Richter, Heinrich Bovensmann, and John P. Burrows

Despite its key role in climate change, large uncertainties persist in our knowledge of the anthropogenic emissions of carbon dioxide (CO₂) and no global observing system exists that allows us to monitor emissions from localized CO₂ sources with sufficient accuracy. The Orbiting Carbon Observatory-2 (OCO-2) satellite allows retrievals of the column-average dry-air mole fractions of CO₂ (XCO₂). However, regional column-average enhancements of individual point sources are usually small, compared to the background concentration and its natural variability, and often not much larger than the satellite's measurement noise. This makes the unambiguous identification and quantification of anthropogenic emission plume signals challenging. Nitrogen dioxide (NO₂) is co-emitted with CO₂ when fossil fuels are combusted at high temperatures. It has a short lifetime on the order of hours so that NO₂ columns often greatly exceed background and noise levels of modern satellite sensors near sources, which makes it a suitable tracer of recently emitted CO₂. At IUP-Bremen a method has been developed to obtain information on CO₂ emissions from localized emission sources such as coal-fired power plants and cities by combining OCO-2 XCO₂ retrievals with Sentinel-5-Precursor (S5P) NO₂ column retrievals. Figure 25 shows results obtained for the Medupi and Matimba power plants in South Africa on 11 July 2018.

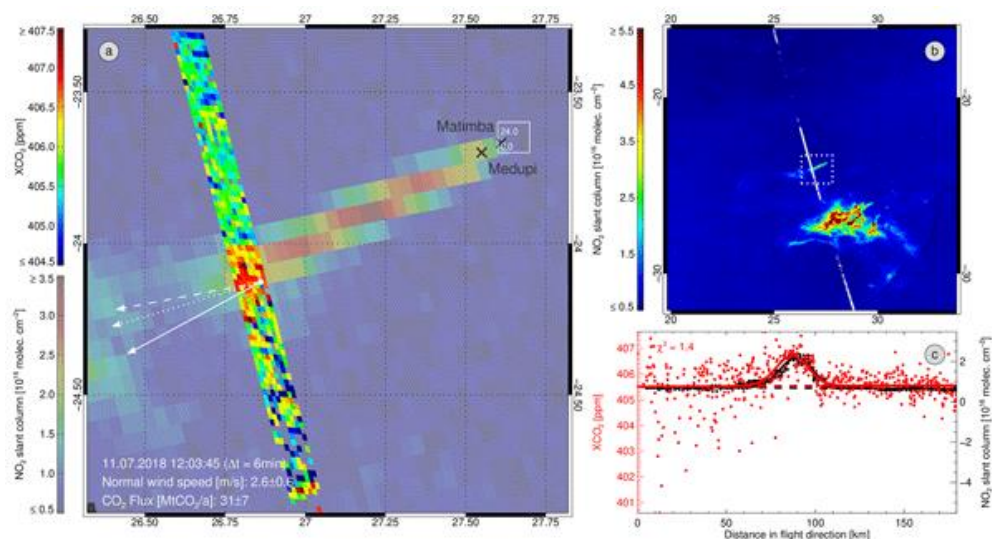


Figure 25: OCO-2 XCO₂ and S5P NO₂ (see colour bars on the left hand side) along with wind information and the location of the Medupi and Matimba power plants (black crosses). The NO₂ emission plume originating at the power plants is clearly visible and also the elevated XCO₂ along the OCO-2 orbit track. The derived CO₂ flux is shown in the bottom left of this figure. The surrounding area is shown in the top right map and the bottom left figure shows XCO₂ and NO₂ columns along the OCO-2 orbit track (source: Reuter et al., 2019).

Reference

Reuter, M., Buchwitz, M., Schneising, O., Krautwurst, S., O'Dell, C. W., Richter, A., Bovensmann, H., and Burrows, J. P.: Towards monitoring localized CO₂ emissions from space: co-located regional CO₂ and NO₂ enhancements observed by the OCO-2 and S5P satellites, *Atmos. Chem. Phys.*, <https://www.atmos-chem-phys.net/19/9371/2019/>, 19, 9371-9383, 2019.

IUP-Bremen contributions to a future system relevant for the Paris Climate Agreement

Michael Buchwitz, Maximilian Reuter, Oliver Schneising, Heinrich Bovensmann, and John P. Burrows

Under the Paris Agreement, progress of emission reduction efforts is tracked on the basis of regular updates to national greenhouse gas (GHG) inventories, referred to as bottom-up estimates. However, only top-down estimates based on atmospheric measurements can provide observation-based evidence of emission trends. Today, there is no internationally agreed, operational capacity to monitor anthropogenic GHG emission trends using atmospheric measurements to complement national bottom-up inventories. The European Commission (EC), ESA, ECMWF, EUMETSAT, and experts, for example from IUP-Bremen, are joining forces to develop such an operational capacity for monitoring anthropogenic CO₂ emissions as a new CO₂ service under the EC's Copernicus program. Design studies have been used to translate identified needs into defined requirements and functionalities of this anthropogenic CO₂ emissions Monitoring and Verification Support (CO₂MVS) capacity (Figure 26). A key component of this system is a constellation of CO₂ monitoring satellites, called CO₂M (or CO₂ Sentinel), which are based on the IUP-Bremen CarbonSat concept.

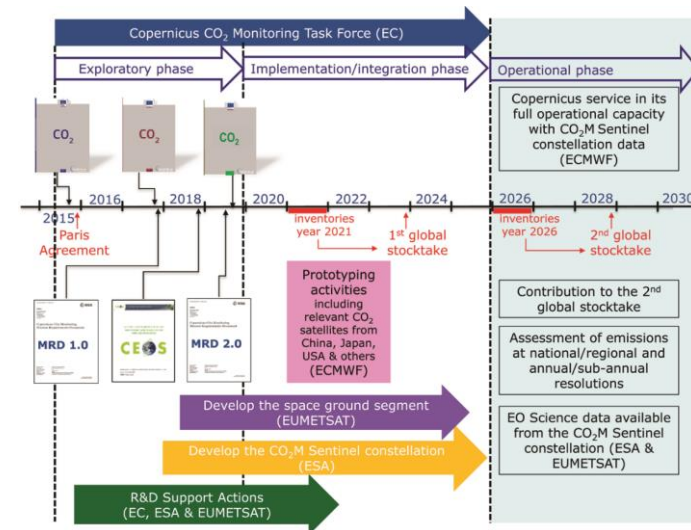


Figure 26: Time schedule and activities related to the development of a future European CO₂ Monitoring and Verification Support (MVS) capacity (source: Janssens-Maenhout et al., 2020).

Reference

Janssens-Maenhout, G., B. Pinty, M. Dowell, H. Zunker, E. Andersson, G. Balsamo, J.-L. Bezy, T. Brunhes, H. Boesch, B. Bojkov, D. Brunner, M. Buchwitz, D. Crisp, P. Ciais, P. Counet, D. Dee, H. Denier van der Gon, H. Dolman, M. Drinkwater, O. Dubovik, R. Engelen, T. Fehr, V. Fernandez, M. Heimann, K. Holmlund, S. Houweling, R. Husband, O. Juvyns, A. Kentarchos, J. Landgraf, R. Lang, A. Loeschner, J. Marshall, Y. Meijer, M. Nakajima, P.I. Palmer, P. Peylin, P. Rayner, M. Scholze, B. Sierk, J. Tamminen, and P. Veefkind, Towards an operational anthropogenic CO₂ emissions monitoring and verification support capacity, *Bulletin of the American Meteorological Society (BAMS)*, 10.1175/BAMS-D-19-0017.1, <https://doi.org/10.1175/BAMS-D-19-0017.1>, pp. 13, 2020.

Unexpected long-range transport of glyoxal and HCHO from wildfires observed by TROPOMI

Leonardo M. A. Alvarado, Andreas Richter, Mihalis Vrekoussis, Andreas Hilboll, Anna B. Kalisz Hedegaard, Oliver Schneising, and John P. Burrows

In August 2018, a high-temperature anomaly led to the outbreak of many fires in the Canadian western province of British Columbia, resulting in the emission of large quantities of particles and trace gases that in turn affected air quality in the region. Because of the magnitude and duration of the fires, large plumes of pollutants developed, which are readily seen as haze in RGB images taken by hyperspectral imagers from space (Figure 27).

Using optical absorption spectroscopy in the UV, visible and NIR wavelength region, the amounts of several trace gases released by the fires can also be determined from space. Using data from the TROPOMI instrument on board the Copernicus Sentinel-5 precursor satellite, carbon monoxide (CO), nitrogen dioxide (NO_2), formaldehyde (HCHO) and glyoxal column amounts could be retrieved for several days during the 2018 fire season (see Figure 27). The large extent of the observed plumes and the high values found for all trace gases illustrates the large impact these fires were having on atmospheric composition.

How far trace gases are transported in a smoke plume depends on their removal rate or atmospheric lifetime. CO has a comparatively long lifetime, and therefore, CO plumes from wild fires can be detected over long distances and even after many days of transport. NO_2 on the other hand has a lifetime of only a few hours, and therefore is mainly found close to the fires. This difference is clearly visible from the maps in Figure 27.

HCHO and CHOCHO are two volatile organic compounds (VOCs) which can be detected using absorption spectroscopy from

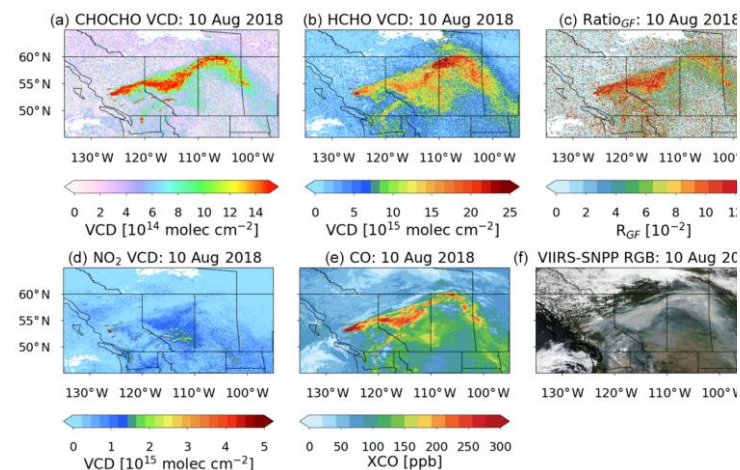


Figure 27: TROPOMI trace gas observations for the plume of the wild fires taken on August 10, 2018. Panels (a), (b), (d), and (e) show the CHOCHO, HCHO, NO_2 , and CO columns, respectively, using aerosol settings appropriate for the plume. Panel (f) shows the VIIRS RGB image with the fire locations overlaid.

space. They are both mainly formed in the atmosphere in the oxidation of other VOCs such as biogenically emitted isoprenes. CHOCHO is however also directly emitted by fires, and it is thus not surprising that high CHOCHO columns are found close to the fires in August 2018. As can be seen in Figure 27, both HCHO and CHOCHO are however found also in other parts of the plume, many hundred kilometres downwind of the fires. This is surprising as the atmospheric lifetimes of both VOCs are short and of the order of a few hours.

In order to investigate this observation in more detail, forward calculations have been performed with the Lagrangian particle dispersion model FLEXPART. In this model, removal of particles from the atmosphere is simulated by a simple exponential de-

cay with a pre-set lifetime. As emission rates from wildfires are highly uncertain, the emission fluxes from the Canadian wildfires are assumed to be proportional to fire radiative power (FRP). The emissions, prescribed in the model, are taken from the Global Fire Assimilation System (GFAS) daily FRP and plume height data. The model was then run forward in time for 120 h, releasing the tracer for the first 24 h (the full UTC day), assuming no temporal variation throughout the day. Vertically, the emissions were evenly distributed over the range of mean altitude of maximum injection heights given by the GFAS data for the respective location. The output of the simulation contains gridded mass concentrations for each time step. Here, a grid with a horizontal resolution of 0.03125° was chosen to match the resolution of the gridded satellite observations. Hourly output from the simulation was recorded and then vertically integrated to yield simulated tracer columns. This was repeated for a series of runs assuming different lifetimes for the tracer.

While the absolute tracer column density from the model output cannot be simply compared to the measurements, a comparison of the plume patterns and relative distribution between satellite observation and model output gives an indication about the meaningfulness of the prescribed mean lifetime. The results of such a comparison are shown in Figure 28, where contour lines of three FLEXPART runs with different lifetimes are overlaid on the TROPOMI CHOCHO observations. As can be seen, a lifetime of 2.9 hours does not reproduce observations at all. However, assuming 14.4 hours leads to remarkably good agreement between the simple forward calculation and the satellite measurements.

Different explanations are possible for the apparent contradiction between the short photochemical lifetime of CHOCHO and HCHO and the observed long-range transport. In principle, the complex photochemistry in the plume could lead to an extended lifetime of the two VOCs, but based on the expected high OH

concentrations, the opposite should be the case. A second explanation could be an efficient recycling process via the aerosol phase, and this has been reported for glyoxal in some studies in the past. However, no such recycling mechanism is known for HCHO, which shows similar behaviour. The most probable explanation is therefore that

other VOCs having longer atmospheric lifetimes are also emitted by the fires, and CHOCHO and HCHO observed in the fire plumes are formed secondarily during transport instead of being emitted directly by the fires.

In order to better understand the processes in the plume, chemical modelling is needed to fully represent the complexity of photochemistry, multi-phase chemistry and mixing in these fire plumes.

Reference

Alvarado, L. M. A., Richter, A., Vrekoussis, M., Hilboll, A., Kalisz Hede-gard, A. B., Schneising, O., and Burrows, J. P.: Unexpected long-range transport of glyoxal and formaldehyde observed from the Copernicus Sentinel-5 Precursor satellite during the 2018 Canadian wildfires, *Atmos. Chem. Phys.*, **20**, 2057–2072, <https://doi.org/10.5194/acp-20-2057-2020>, 2020.

Comparison with model lifetimes - CHOCHO: 10 Aug 2018

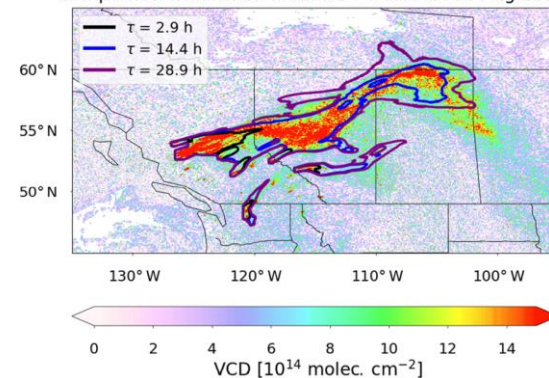


Figure 28: Comparison of glyoxal columns observed by TROPOMI and the results of FLEXPART forward calculations from fire hotspots assuming different lifetimes for a tracer. The best agreement between model and measurements is found for a lifetime of 14.4 hours.

Long-term time series of Arctic tropospheric BrO and its relation to first-year sea ice

Ilias Bougoudis, Anne-Marlene Blechschmidt, Andreas Richter, Sora Seo, and John P. Burrows

Bromine monoxide (BrO) plays a significant role in the atmospheric chemistry of the Arctic. During polar springtime, episodes of strongly enhanced amounts of BrO have been observed in the boundary layer for many years. The formation of these intense plumes of BrO results in tropospheric ozone depletion, affecting the oxidizing capacity of the troposphere. The rapid and sudden appearance of BrO plumes over the Polar Regions has been called the “bromine explosion” and is explained by an autocatalytic multiphase chemical cycle, which occurs on cold saline surfaces such as first year ice, snowpack or blowing snow.

While the first bromine explosions were detected using in-situ and ground-based spectroscopic measurements, satellite observations have now become a much-used tool to monitor the BrO distribution and its changes over time on a regular basis in both the Arctic and Antarctic. The first BrO measurements from space were possible with the GOME instrument in 1996, followed by the SCIAMACHY, OMI, GOME-2 and most recently TROPOMI instruments, which all provide data that can be used to retrieve BrO columns. Combining these observations results in a long-term dataset now covering more than 20 years that can be used to evaluate long-term trends and the effects of Arctic Amplification.

While the basic measurement principle is the same for all these satellite instruments, they differ in spatial resolution, overpass time and also in their instrumental characteristics. Therefore, creation of a consistent data set has to be based on carefully chosen retrieval settings and evaluation of time periods where

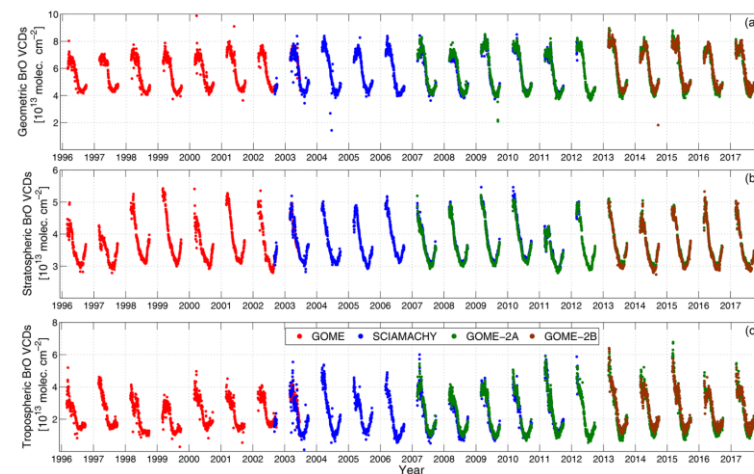


Figure 29: Long-term BrO time series over the Arctic region: (a) daily geometric BrO VCDs (10^{13} molec cm^{-2}), (b) daily stratospheric BrO VCDs (10^{13} molec cm^{-2}) and (c) daily tropospheric BrO VCDs (10^{13} molec cm^{-2}). All figures show daily averages $\geq 70.0^\circ\text{N}$. GOME data are coloured in red, SCIAMACHY in blue, GOME-2A in green and GOME-2B in brown.

measurements from two instruments are available in order to create a seamless data set.

In this study, data from the GOME, SCIAMACHY, GOME-2A and GOME-2B instruments have been unified and merged to one consistent time series (Figure 29). From the spectroscopic retrieval, column amounts integrated along the light path through the atmosphere are produced. These need to be corrected for the stratospheric contribution, which here is done with the help of a model based parametrisation using ozone and NO_2 measurements from the same sensor, and tropopause height from meteorological analysis as input (Theys et al., 2009). The resulting tropospheric columns are finally converted to vertical tropospheric columns by applying an air mass factor, which is determined from radiative transfer calculations. The resulting time series are shown in Figure 29.

For any trend analysis based on merged datasets, it is important to know how consistent the data set is between the individual time series from the different instruments. How good the agreement is in the merged BrO satellite data set is demonstrated in Figure 30, where data for the three time periods with overlapping measurements are shown.

Using this long-term data set, a trend analysis can be performed to investigate, whether or not Arctic springtime BrO has been constant or changing over time. As can be seen in Figure 31, a clear upward trend in BrO columns is observed with about 1.5% increase per year. In addition to the upward trend, there is large interannual variability, arguably as result of differences in meteorology and sea-ice coverage.

The significant and systematic increase in BrO could be linked to recent changes in Arctic climate, which include a marked decrease in multiyear sea ice, increasing temperatures, and changes in cyclone occurrence frequencies. A detailed statistical analysis between sea ice and meteorological parameters and the BrO timeseries revealed, that there is a general correlation with the area of first-year sea ice (see Figure 31). This correla-

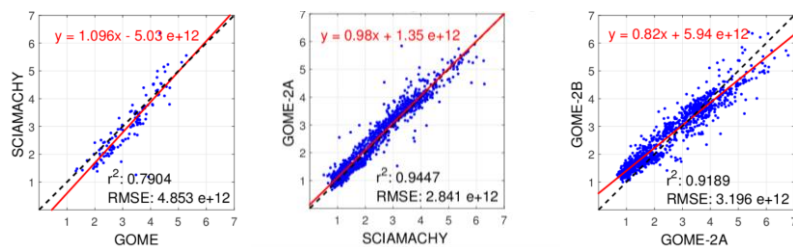


Figure 30: Scatterplots of tropospheric BrO VCDs for (left) GOME against SCIAMACHY (August 2002 to June 2003), (middle) SCIAMACHY against GOME-2A (March 2007 to March 2012) and (right) GOME-2A against GOME-2B (March 2013 to September 2017). The dashed black line in each scatterplot is the reference line, and the red one is the linear regression line. The units for all scatterplots are (10^{13} molec cm^{-2}).

tion appears reasonable as first year sea ice is more saline than multiyear ice, and thus favours bromine release. However, evaluation of the spatial correlation between the change in first year sea ice coverage and BrO columns showed inconsistent results and an overall correlation coefficient of only 0.32 for daily data, indicating that other parameters such as meteorology also play a role. In particular the long-range transport of BrO by cyclones and the deposition and re-emission of bromine on snow are mechanisms that may interfere with a simple correlation analysis and need to be studied in more detail in the future.

References

- Bougoudis, I., Blechschmidt, A.-M., Richter, A., Seo, S., Burrows, J. P., Theys, N., and Rinke, A.: Long-term time series of Arctic tropospheric BrO derived from UV–VIS satellite remote sensing and its relation to first-year sea ice, *Atmos. Chem. Phys.*, 20, 11869–11892, <https://doi.org/10.5194/acp-20-11869-2020>, 2020.
- Theys, N., Van Roozendael, M., Errera, Q., Hendrick, F., Daerden, F., Chabrilat, S., Dorf, M., Pfeilsticker, K., Rozanov, A., Lotz, W., Burrows, J. P., Lambert, J.-C., Goutail, F., Roscoe, H. K., and De Mazière, M.: A global stratospheric bromine monoxide climatology based on the BASCOE chemical transport model, *Atmos. Chem. Phys.*, 9, 831–848, <https://doi.org/10.5194/acp-9-831-2009>, 2009.

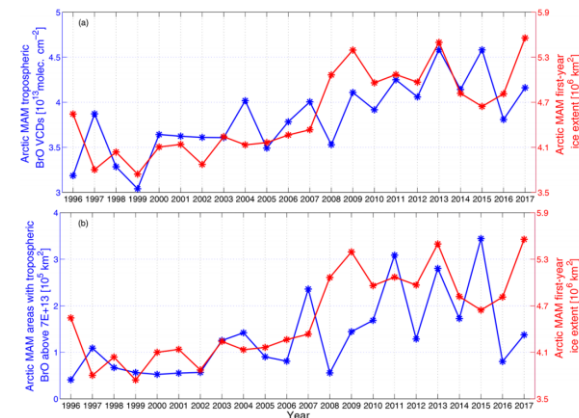


Figure 31: (a) Polar spring (MAM) mean time series of tropospheric BrO VCDs over sea ice and first-year sea ice extent over the Arctic, (b) polar spring (MAM) mean time series of areas with BrO VCDs above the threshold of 7×10^{13} molec cm^{-2} and first-year sea ice extent over the Arctic.

Horizontal inhomogeneities in NO₂ concentrations above a shipping lane observed using ground-based MAX-DOAS measurements

André Seyler, Andreas C. Meier, Folkard Wittrock, Lisa Kattner, Barbara Mathieu-Üffing, Enno Peters, Andreas Richter, Anja Schönhardt, and John P. Burrows

Over the last decades, there has been a strong increase in ship traffic and shipping emissions of gas-phase pollutants, leading to an increasing contribution of shipping emissions to air pollution in coastal regions. Consequently, emission reduction measures have been enacted by the International Maritime Organization (IMO) globally as well as, more stringently, locally in so-called emission control areas (ECAs) like the North and Baltic seas. For NO_x, the allowed emission rate depends on the rated rotational speed of the engine crankshaft (engine power and fuel efficiency) and is implemented in three tiers: Tier I (globally) for ships built between 2000 and 2010, Tier II (globally) for ships built from 2011 onwards, and Tier III (locally in ECAs) for ships built from 2016 onwards, with the last one not yet implemented in the North and Baltic seas, shifted to 2021. In order to monitor the effectiveness of these measures as well as the overall impact of ship emissions on air quality, measurements of air pollution from ships are required.

One way of taking such measurements is by remote sensing using ground-based MAX-DOAS measurements from a station close to a shipping lane. Such measurements were performed from July 2013 to July 2016 on Neuwerk, an Island close to the shipping lane entering the river Elbe towards Hamburg harbour, measuring the shipping lane at 1° elevation under five different viewing azimuths (see Figure 33). The advantage of MAX-DOAS measurements is that in contrast to in-situ observations, they do not depend on emissions being transported to the instru-

ment. A disadvantage is that usually, the distance to the ship plume cannot be determined, making assignment to individual ships difficult.

This problem has been addressed by combining measurements of NO₂ taken simultaneously in the UV and visible spectral range. Due to increased Rayleigh scattering in the UV, the length of the light path is reduced as compared to measurements in the visible, and combination of the two measurements enables separation of close and more distant plumes (see Figure 32). This Onion Peeling approach was used to separate the measurements into two regions at different distance from the instrument. In Figure 33, two exemplary situations are shown where wind direction led to different distances of the emission plumes from the instrument. A rough estimate of plume position is modelled by assuming constant emission from the moving ship and dispersion of a Gaussian plume (shown in grey). The light path averaged NO₂ mixing ratios for the five viewing directions and the two segments are shown in colour, nicely reflecting the position of the ship plumes. The in-situ instrument operating close to the MAX-DOAS measurements picked up the signal only on the first day when wind brought emissions to the measurement site, but not on the second, when wind direction was less favourable.

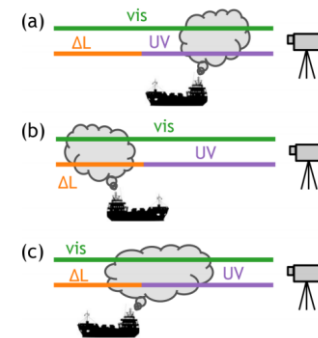


Figure 32: Plume–light path geometry for three possible cases: when the plume is close to the instrument and completely covered by the UV path (a), when the plume is further away from the instrument than the UV scattering point and is only covered by the visible path (and ΔL) (b), and when the plume is located around the UV scattering point (c).

The plume model also can be used to improve the estimate of the NO₂ mixing ratio in the emission plume. While the MAX-DOAS measurements only provide the NO₂ column integrated along the (partial) light path, the plume model can give an estimate of the plume width, which can be used to derive an estimate of the in-plume mixing ratio.

The values derived by this method can be validated by comparison with measurements from the airborne AirMAP instrument, which flew several transects along MAX-DOAS viewing directions in August 2013. The AirMAP is an imaging spectrometer, measuring NO₂ with the same absorption spectroscopy method as MAX-DOAS. Thanks to its nadir-viewing geometry and the ability to simultaneously observe several positions across-track, it creates a map of the spatial distribution of NO₂ along its track, which can be compared to the MAX-DOAS retrievals. An example of such a comparison is shown in Figure 34. As can be seen, the NO₂ enhancements observed by AirMAP nicely fit to the

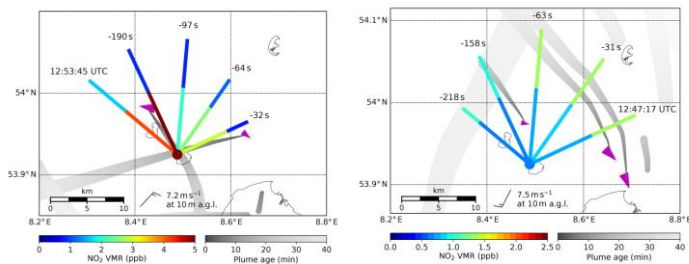


Figure 33: Comparison of two situations with ship emissions being close to the instrument (left) and farther away (right). Horizontal light path lengths and corresponding path-averaged volume mixing ratios of NO₂ for five viewing directions are shown as coloured lines and the in situ NO₂ VMR as a coloured dot at the location of the instrument. Magenta triangles show the ship position and course, with larger triangles for larger ships. The modelled plumes are shown in grey, with the lightness of the grey shading representing the plume age. The broader plume in the eastern part of the right map originates from the Wilhelmshaven power plants.

plume positions derived with the plume model. Small offsets are due to the time differences between measurements and model as indicated in the figure. The NO₂ distribution observed by AirMAP confirms the two-segment NO₂ distribution from the MAX-DOAS measurements.

A more quantitative comparison can be obtained if both MAX-DOAS and AirMAP measurements are converted to in-plume mixing ratios. This conversion can be based on either the modelled plume position and size, or on an estimate of both combining AirMAP and MAX-DOAS geometrical information. The two approaches lead to very similar estimates in the AirMAP-measurements (4.7 ± 3.0 ppb and 4.5 ± 2.7 ppb), in good agreement with the MAX-DOAS estimate of 3.6 ± 1.8 ppb.

Reference

Seyler, A., Meier, A. C., Wittrock, F., Kattner, L., Mathieu-Üffing, B., Peters, E., Richter, A., Ruhtz, T., Schönhardt, A., Schmolke, S., and Burrows, J. P.: Studies of the horizontal inhomogeneities in NO₂ concentrations above a shipping lane using ground-based multi-axis differential optical absorption spectroscopy (MAX-DOAS) measurements and validation with airborne imaging DOAS measurements, *Atmos. Meas. Tech.*, 12, 5959–5977, <https://doi.org/10.5194/amt-12-5959-2019>, 2019.

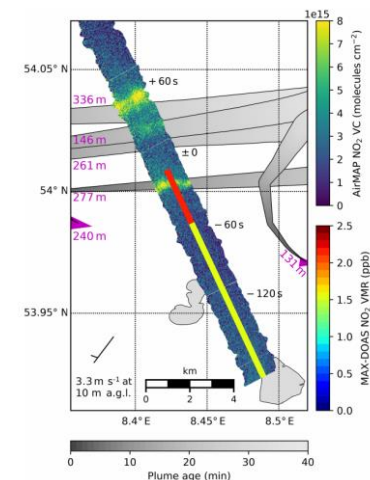


Figure 34: Map showing the MAX-DOAS path-averaged VMRs (coloured lines) and AirMAP vertical columns of NO₂ (broad image stripe beneath) on 21 August 2013 around 9:53 UTC (11:53 LT). Magenta triangles show current ship positions and course, and magenta numbers denote the ship length. The modelled plumes (for the MAX-DOAS measurement time) are shown in grey, with the lightness of the grey shading representing the plume age. The time difference between AirMAP and MAX-DOAS measurements is indicated in the map at specific parts of the flight track. Wind direction and speed are shown with a meteorological wind barb.

Ambae volcanic eruption observed by the OMPS-LP instrument

Alexei Rozanov, Elizaveta Malinina-Rieger, and John P. Burrows

Stratospheric aerosols play an important role in the Earth system and in climate. Through the scattering of solar radiation back to space and by heating the stratosphere through the absorption of thermal infrared radiation upwelling from the troposphere, stratospheric aerosols impact the radiative forcing and thus the energy balance of the Earth's atmosphere. By providing a surface for heterogeneous reactions, which release reactive halogens, stratospheric aerosols contribute to the catalytic depletion of ozone.

The background state of stratospheric aerosols is formed by the upwelling of the source gases such as carbonyl sulphide and dimethyl sulphide. Large-scale changes to the stratospheric aerosol layer are primarily driven by moderate and large volcanic eruptions, which emit sulphur dioxide directly into the upper troposphere lower stratosphere (UTLS) region. The most prominent volcanic eruptions during the last years were those of Ambae and Raikoke volcanos, occurring in 2018 and 2019, respectively. Other relevant mechanisms perturbing the background state of the stratospheric aerosols are the transport of biomass burning products by convective clouds and transport of sulphur from anthropogenic fossil fuel combustion with the Asian Monsoon.

One of the widely used sources of information on stratospheric aerosol characteristics is the retrieval of aerosol extinction coefficients from space-borne measurements in the visible and near-infrared spectral range of solar light, scattered by or transmitted through the Earth's atmosphere.

To resolve the vertical structure of the aerosol extinction coefficient, measurements in limb or occultation viewing geometry (i.e. when instrument looks tangentially through the atmosphere) are used. From the satellite instruments capable of performing this kind of measurements, only three are currently in operation: OSIRIS on Odin (Llewellyn et al., 1997), OMPS-LP on Suomi-NPP (Flynn et al., 2014) and SAGE III on ISS (Cisewski et al., 2014). From these, the OMPS-LP instrument features the best spatial and temporal coverage.

The IUP Bremen team has developed an algorithm to retrieve vertical profiles of the aerosol extinction coefficient from OMPS-LP measurements at a wavelength of 869 nm. The retrieval is done between 10.5 and 33.5 km using the measurement at 34.5 km tangent height as the reference (i.e. measurements at tangent heights between 10.5 and 33.5 km are normalized by the measurement at 34 km tangent height). An effective Lambertian albedo is simultaneously retrieved using the sun-normalized

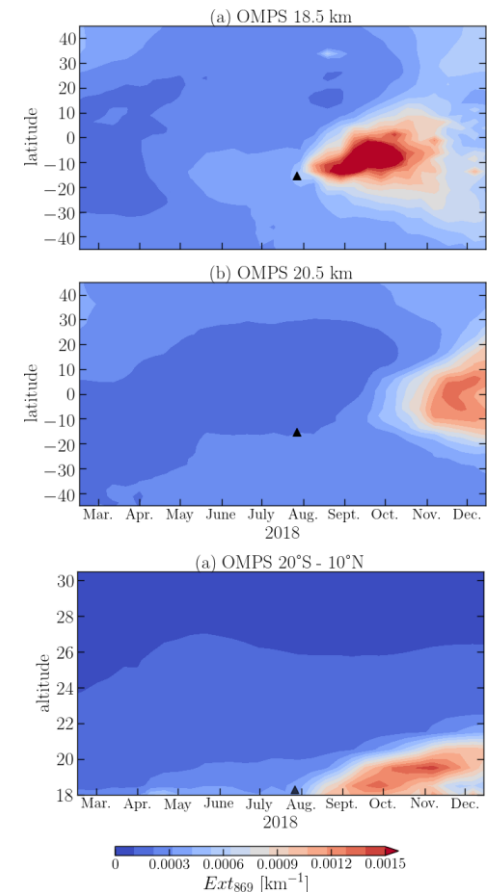


Figure 35: Evolution of the stratospheric aerosol extinction coefficient before and after the Ambae eruption as seen by the OMPS-LP instrument. Upper panel: extinction coefficient as a function of the latitude and time at the altitude of 18.5 km. Middle panel: same as the upper panel but for the altitude of 20.5 km. Lower panel: vertical distribution of the Ambae plume integrated over the tropics. The black triangle marks the location of the Ambae volcano and time of the strongest eruption.

spectrum at 34.5 km. Further details on the retrieval algorithms can be found in (Malinina et al., 2020).

The database of the aerosol extinction coefficients retrieved from OMPS-LP measurements at IUP Bremen was used to investigate the evolution of the volcanic plume after the eruption of Ambae in July 2018. Ambae (or Aoba) island is located in the South Pacific in Vanuatu (15.39°S, 167.84°E) being a shield volcano with three lakes in its caldera. According to the Smithsonian Institution (2019) database, the active period of 2017-2018 was the strongest ever for this volcano. This period started on the 6 September 2017 and lasted over a year ending on the 30 October 2018. For the stratospheric aerosol community, the most essential are the eruption phases when SO₂ was injected above the tropopause. The most severe was the eruption on the 27 July 2018 injecting SO₂ and volcanic ash into the UTLS region (at about 17 km altitude).

To evaluate the plume evolution after the Ambae eruption, we analyse the extinction coefficients of the stratospheric aerosol averaged over 10-day periods and over all longitudes. The upper two panels of Figure 35 show the plume development at altitude levels of 18.5 and 20.5 km, respectively. In early May 2018, the plume from the previous, weaker eruption occurring on the 6th of April becomes apparent at 18.5 km. The perturbation of the aerosol load at 20.5 km from this eruption is rather negligible. After the eruption in late July 2018, the aerosol extinction increases at the source location without any significant time lag. This is most probably caused by the volcanic ash erupted directly to this altitude. In about two weeks, the volcanic plume starts to spread both northwards and southwards and is located between the equator and 35°S in early September, reaching 45°N in November – December 2018. In the southern hemisphere, the plume at 18 km mixes with that from the previ-

ous weaker eruption. An increased aerosol loading is observed south of 35°S in September intensifying further with time. By the middle of October, the plume starts to vanish around the equator and continues weakening over time. At 20.5km, the plume appears in mid-September at around 10°S, spreads then both northwards and southwards and reaches its maximum in November 2018.

The vertical distribution of the aerosol plume is presented in the bottom panel of Figure 35. Since most of the plume stayed in the tropical region, the stratospheric aerosol extinction data were averaged between 20°S and 10°N. It is seen that the perturbation of the aerosol extinction after the Ambae eruption reached the altitude of about 23.5km and the plume started relaxing towards the end of 2018. It is worth noting that the vertical lofting of the volcanic plume is related to the Brewer-Dobson Circulation with the upward branch in the tropics. The patterns seen in the bottom panel of Figure 35 are a prime example of the stratospheric tape-recorder effect.

In Malinina et al. (2020), the volcanic plume evolution was compared to simulations with the MECHAM5-HAM model (Stier et al., 2005) and a good agreement in the shape and intensity of the observed and modelled plumes was found. However, the vertical transport in MECAM5-HAM was found to be slightly weaker. The tropical radiative forcing caused by the increase in stratospheric aerosols due to the Ambae eruption was estimated to be about -0.13 W/m².

References

Cisewski, M., Zawodny, J., Gasbarre, J., Eckman, R., Topiwala, N., Rodriguez-Alvarez, O., Cheek, D., and Hall, S.: The Stratospheric Aerosol and Gas Experiment (SAGE III) on the International Space Station (ISS) Mission, in: Sensors, Systems, and Next-Generation Satellites XVIII, vol. 9241, p. 924107, International Society for Optics and Photonics, 2014.

Flynn, L., Long, C., Wu, X., Evans, R., Beck, C., Petropavlovskikh, I., McConville, G., Yu, W., Zhang, Z., Niu, J., Beach, E., Hao, Y., Pan, C., Sen, B., Novicki, M., Zhou, S., and Seftor, C.: Performance of the ozone mapping and profiler suite (OMPS) products, *J. Geophys. Res.-Atmos.*, 119, 6181–6195, 2014.

Llewellyn, E. J., Degenstein, D. A., McDade, I. C., Gattinger, R. L., King, R., Buckingham, R., Richardson, E. H., Murtagh, D. P., Evans, W. F. J., Solheim, B. H., Strong, K., and McConnell, J. C.: Osiris – An Application of Tomography for Absorbed Emissions in Remote Sensing, in: *Applications of Photonic Technology* 2, 627–632, Springer, 1997.

Malinina, E., Rozanov, A., Niemeier, U., Peglow, S., Arosio, C., Wrana, F., Timmreck, C., von Savigny, C., and Burrows, J. P.: Changes in stratospheric aerosol extinction coefficient after the 2018 Ambae eruption as seen by OMPS-LP and ECHAM5-HAM, *Atmos.*

Solar Variability

Mark Weber, Tina Hilbig, Klaus Bramstedt, Stefan Noë, I and John P. Burrows

Space-borne UV spectrometers dedicated for atmospheric measurements usually also take regular observations of the sun. The daily solar spectral irradiance (SSI), itself, is also of large scientific interest as it allows us to investigate irradiance variability due to solar magnetic activity on daily to decadal time scales. Daily SSI irradiance data from space are now available going back to the late 1970s from several atmospheric sounders in combination with dedicated solar missions.

A big challenge for space UV spectral measurements is the optical degradation due to harmful UV radiation and polymerisation of optical surfaces that lead to blinding of the instruments. Complex degradation corrections must be applied to obtain reliable time series. Particularly in the visible spectral range, large uncertainties still exist. Considerable efforts were undertaken to recalibrate SCIAMACHY

Chem. Phys. Discuss., <https://doi.org/10.5194/acp-2020-749>, in review, 2020.

Smithsonian Institution: Global Volcanism Program Database, http://volcano.si.edu/search_eruption.cfm, 2019.

Stier, P., Feichter, J., Kinne, S., Kloster, S., Vignati, E., Wilson, J., Ganzeveld, L., Tegen, I., Werner, M., Balkanski, Y., Schulz, M., Boucher, O., Minikin, A., and Petzold, A.: The aerosol–climate model ECHAM5–HAM, *Atmos. Chem. Phys.*, 5, 1125–1156, 2005.

solar irradiance data using an optical bench simulator and a mirror model that accounts for contamination of the external mirror surface. An improved solar reference spectrum from SCIAMACHY covering the optical spectral range from UV to SWIR spectral was established (Hilbig et al. 2018). Recent research focused on improving irradiance time series from SCIAMACHY (Hilbig et al., 2020).

Improvements in the radiometric calibration were achieved by proper calibration of the azimuthal scan mechanism containing a diffuser

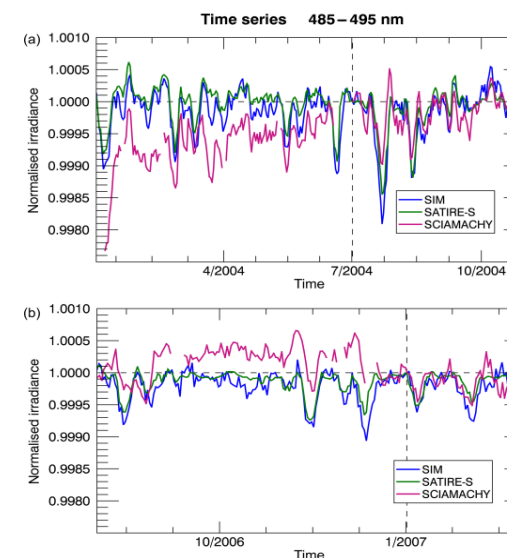


Figure 36: SCIAMACHY irradiance variations in various time periods and comparison with SIM/SOLSTICE and the empirical model SATIRE-S (Hilbig et al., 2020). Periodic signals show variations in the solar radiation with the solar rotation of approximately 27 days. Variations are on the order of a few tenths of a percent.

and by use of the internal white-light-source (WLS). An example of SCIAMACHY irradiance time series at about 490 nm is shown in Figure 36, demonstrating good agreement with other data.

From the solar data of UV atmospheric sounders like GOME, GOME-2, and SCIAMACHY as well as other satellite missions, solar proxies can be derived that are largely insensitive to instrument degradation. A popular such proxy is the Mg II core-to-wing ratio (Mg II index) which is derived from the Mg II doublet observed at 280 nm. This index is often used for SSI reconstruction in solar or climate models to investigate the atmospheric effects from direct solar radiation. We derive the Mg II indices from GOME, SCIAMACHY, and GOME-2 observations and combine them with other available datasets to create the Bremen Composite Mg II index (Snow et al., 2014, 2019). This index shows the changes with the Schwabe (11-year magnetic activity) and Carrington (27-day solar rotation) cycles and now spans more than 40 years (Figure 37). The last solar cycle (SC24) was less active and its duration (slightly above 9 years) shorter than the three solar cycles before. The current solar activity is now at a raise again after a quite prolonged solar minimum.

References

Hilbig, T., M. Weber, K. Bramstedt, S. Noël, J. P. Burrows, J. M. Krijger, R. Snel, M. Meftah, L. Dame, S. Bekki, D. Bolsee, N. Pereira, D. Sluse: The new SCIAMACHY reference solar spectral irradiance and its validation, *Sol. Phys.*, 293, 121, doi:10.1007/s11207-018-1339-9, 2018.

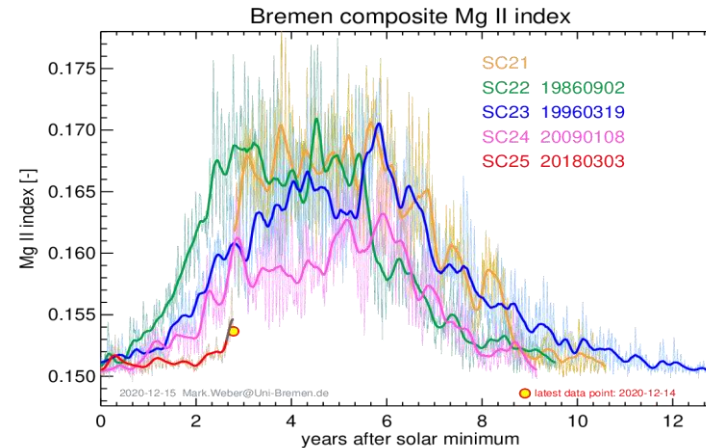


Figure 37: Comparisons of solar activity in solar cycles 21 to 24 using the Bremen Mg II Composite Index. The thick curves show the Mg II index time series twice smoothed with a 55-day boxcar. Dates of minima of solar cycles (YYYYMMDD) were determined from the smoothed Mg II index. UV solar activity was lower in solar cycle 24 compared to the three previous cycles (Daily updates available from <http://www.iup.uni-bremen.de/UVSAT/Datasets/mgii>).

Hilbig, T., Bramstedt, K., Weber, M., Burrows, J. P., and Krijger, M.: Optimised degradation correction for SCIAMACHY satellite solar measurements from 330 to 1600 nm by using the internal white light source, *Atmos. Meas. Tech.*, 13, 3893–3907, doi:10.5194/amt-13-3893-2020, 2020.

Snow, M., Machol, J., Viereck, R., Woods, T., Weber, M., Woodraska, D., and Elliott, J.: A revised Magnesium II core-to-wing ratio from SOLSTICE. *Earth Space Sci.*, 2, doi:10.1029/2019EA000652, 2019.

The unusual stratospheric Arctic winter 2019/2020: Record ozone loss

Mark Weber, Carlo Arosio, Alexei Rozanov, Andreas Meier, Andreas Richter, Kai-Uwe Eichmann, and John P. Burrows

Satellite observations of relevant trace gases, together with meteorological data from ERA5, were used to describe the dynamics and chemistry of the spectacular Arctic 2019/20 winter/spring season. Exceptionally low total ozone

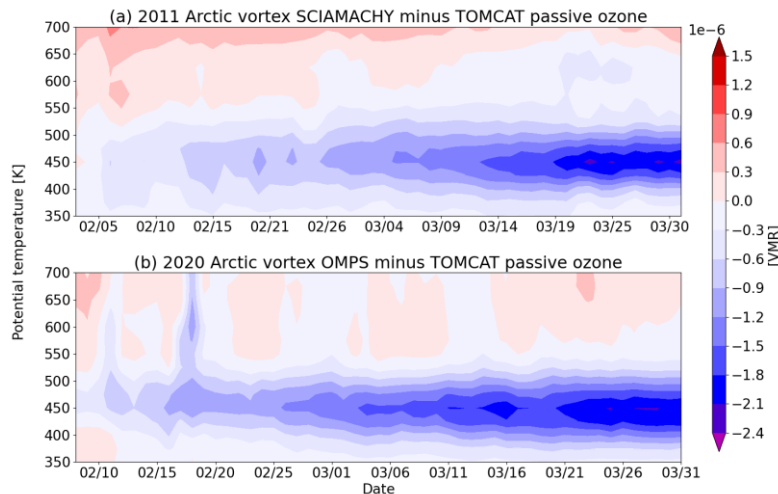


Figure 39: Time-altitude cross-section of estimated ozone loss in late Arctic winter and early spring (a) from SCIAMACHY in 2011 and (b) from OMPS-LP in 2020. The daily ozone loss was determined from the difference between Arctic vortex-mean passive ozone profile from TOMCAT and observed ozone profiles. The mean ozone loss was slightly above 2.1 ppmv (80%) at the potential temperature level 450 K (~18 km altitude) by the end of March. Polar-vortex averaged zone losses were of comparable magnitude in Arctic winter 2010/11 and 2019/20.

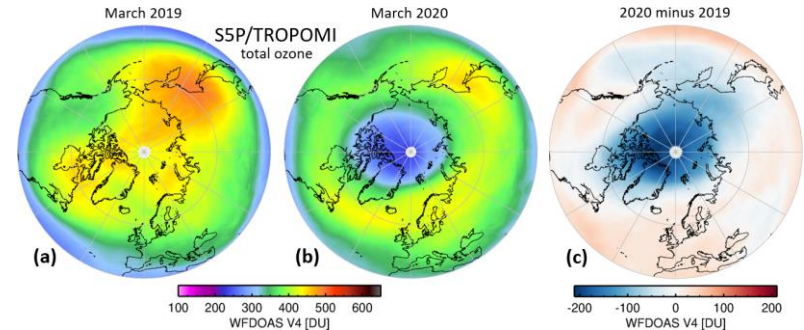


Figure 38: Arctic March mean total ozone (DU) from TROPOMI in (a) 2019 and (b) 2020, representative for years with average conditions and above-average-sized polar vortices, respectively. (c) Difference (DU) between mean March 2020 and 2019 total ozone. The total ozone was retrieved using WFOAS (weighting function DOAS) V4

values of slightly less than 220 DU were observed within an unusually large stratospheric polar vortex in mid-March (see also Figure 38). This was associated with very low temperatures and extensive polar stratospheric cloud formation, a prerequisite for substantial springtime ozone depletion. Very high OClO and very low NO₂ column amounts observed by GOME-2A were indicative of unusually large active chlorine levels and significant denitrification, which likely contributed to large chemical ozone loss.

Using results from the TOMCAT chemical transport model (CTM) and ozone observations from S5P/TROPOMI, GOME-2 (total column), SCIAMACHY and OMPS-LP (vertical profiles) chemical ozone loss was evaluated and compared with the previous record Arctic winter 2010/11. The polar-vortex-averaged total column ozone loss in 2019/20 reached 88 DU (23%) and 106 DU (28%) based upon observations and model, respectively, by the end of March, which was similar to that derived for 2010/11. The total column ozone loss is in agreement with OMPS-LP-derived partial column loss between 350 K and 550 K to within the uncertainty. The maximum ozone loss (~80%) observed by OMPS-LP was near the

450K potential temperature level (~18 km altitude, see Figure 39). Because of the larger polar vortex area in March 2020 compared to March 2011 (about 25% at 450 K), ozone mass loss was larger in Arctic winter 2019/20.

March-mean polar-cap-mean modelled chemical column ozone loss reached 78 DU similar to that in 2011. However, weak dynamical replenishment of only 59 DU from December to March was key to producing the very low (<220 DU) column ozone values. A model simulation with peak observed stratospheric total chlorine and bromine loading (from the mid-1990s) shows that gradual recovery of the ozone layer over the past two decades ameliorated the polar cap ozone depletion in March 2020 by about 20 DU

Molecular spectroscopy in support of earth remote sensing

Victor Gorshlev, Mark Weber, Heinrich Bovensmann, and John P. Burrows

Algorithms that retrieve trace gas amounts from remotely sensed spectral data rely, among others, on spectroscopic data characterizing the molecular absorption. Errors and uncertainties in spectroscopic data often limit the accuracy of the retrieval results.

Although numerous spectroscopic datasets based on laboratory measurements and theoretical considerations are already available, in many cases they are not of sufficient quality and there is still room for improvements that benefit the retrieval accuracy.

Advances in experimental instrumentation and setups allow us to produce spectroscopic parameters with lower uncertainties. Acquisition of high-quality spectroscopic data for remote sensing applications is an essential part of the experimental activity at our Molecular Spectroscopy Laboratory. In our laboratory, we perform spectroscopic measurements

References

Feng, W., Dhomse, S., Arosio, C., Weber, M., Burrows, J. P., Santee, M. L. and Chipperfield, M. P.: Arctic ozone depletion in 2019/20: Roles of chemistry, dynamics and the Montreal Protocol, *Earth Sp. Sci. Open Arch.*, 15, doi:10.1002/essoar.10505119.1, 2020 (Preprint submitted to *Geophys. Res. Lett.*).

Weber, M., Arosio, C., Feng, W., Dhomse, S., Chipperfield, M. P., Meier, A., Burrows, J. P., Eichmann, K.-U., Richter, A. and Rozanov, A.: The unusual stratospheric Arctic winter 2019/20: Chemical ozone loss from satellite observations and TOMCAT chemical transport model, *Earth Sp. Sci. Open Arch.*, 17, doi:10.1002/essoar.10505224.1, 2020 (Preprint submitted to *J. Geophys. Res. Atmos.*).

using an Echelle spectrometer covering the UV spectral region and a Fourier transform spectrometer (FTS) encompassing the near UV, visible, and near IR. Several absorption cell setups with extended cooling capacities allow us to measure molecular absorption cross-sections at atmospher-

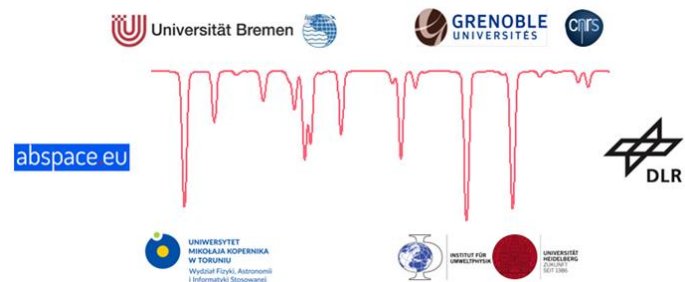


Figure 40: Participants of the ISOGG (Improved Spectroscopy for satellite measurements Of Greenhouse Gases) research

ically relevant temperatures ranging from -80°C to room temperature.

Several research projects are currently ongoing in the Molecular Spectroscopy Laboratory.

In late 2020 the ISOGG (Improved Spectroscopy for satellite measurements Of Greenhouse Gases) was started. It is a joint international effort of several research groups (Figure 40). The goals and objectives of this project include the provision of improved spectroscopic data of CO_2 , O_2 , and possibly H_2O and CH_4 required for the currently operational and upcoming remote sensing missions (CarbonSat/ CO_2M , Sentinel-5P/TROPOMI, and Sentinel-5/UVNS).

Following tasks are planned to achieve the project goals:

1. Perform literature survey and determine the requirements for spectroscopic data. The resulting work plan for new spectroscopic measurements will fill the gap between the existing spectroscopic data and the requirements.
2. Perform spectroscopic measurements of relevant species in several laboratories with extensive experience in quantitative spectroscopy.
3. Investigate whether combined analysis including spectra from other sources is beneficial. Other spectroscopic data products may also be merged in.
4. Perform validation of the new spectroscopic data using high resolution ground-based solar occultation instruments.

Current primary research activity is dedicated to MERLIN (Methane Remote Sensing LIDAR Mission) which is a joint French - German mission facilitating methane observations in the Earth atmosphere. Destined to launch in 2024, MERLIN will use a LIDAR Instrument (Light Detection and Rang-

ing) to track and observe the greenhouse gas from an orbit at 500 km altitude (Figure 41). The mission goal is the generation of global maps of methane concentration distribution. In addition, MERLIN will allow us to determine which regions act as methane sources and sinks.

Within the SMERLIN (Spectroscopy for MERLIN) project, laboratory measurements and corresponding data analysis involving advanced absorption line shape profiles are being performed in order to determine line parameters for CH_4 in the spectral region used by MERLIN ($6074\text{--}6078\text{ cm}^{-1}$, focus on the vicinity of $R(6)$ manifold at 6077 cm^{-1} , or $1.64\text{ }\mu\text{m}$) (Figure 42).

Other recent measurement campaigns of the Molecular Spectroscopy Laboratory include the acquisition of ozone absorption cross-sections in the UV-VIS-IR spectral range from 210 to 1100 nm at an unprecedentedly large number of temperatures and selected methane absorption lines and bands in the short-wave infrared (SWIR).

The Molecular Spectroscopy Laboratory is also involved in several educational projects, introducing the basic practical concepts of absorption spectroscopy to high school students and participating in the international postgraduate programme in Environmental Physics.

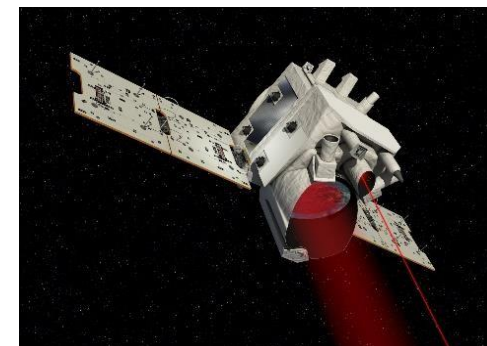


Figure 41: Artist's conception of the MERLIN satellite, which will monitor atmospheric methane using a lidar instrument. (CNES/Illustration D. Ducros).

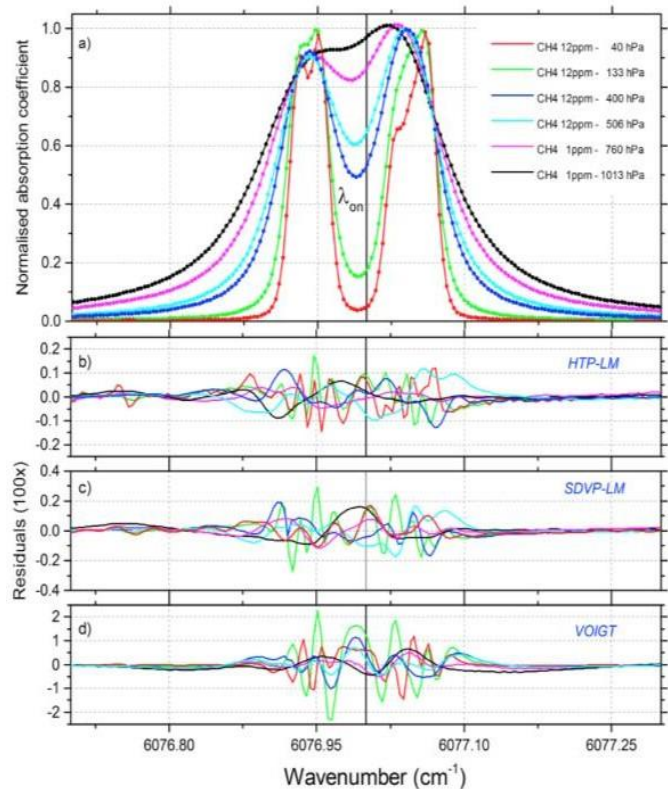


Figure 42: Multispectrum fit results of the six air-broadened spectra in the $2\nu_3 R(6)$ ^{12}CH manifold region. (a) All the spectra (normalized to their peak absorption) considered. Measurements are represented using dots while lines are for the modelled absorptions. (b) The fit residuals (observed minus calculated) using the first-order line-mixing HTP (expanded scale $\times 100$); (c) those obtained using the first-order line-mixing speed-dependent Voigt profile; (d) the fit residuals obtained with the VP. The wavenumber position of the MERLIN “online” position is indicated as a thick black line. (Source: Delahaye et al, 2016).

References

Gorshelev V., Serdyuchenko A., Weber M., and Burrows J.P.: High spectral resolution ozone absorption cross-sections: Part I. Measurements, data analysis and comparison around 293 K, *Atmos. Meas. Tech.*, 7, 609–624, 2014.

Serdyuchenko A., Gorshelev V., Weber M., Chehade W., and Burrows J.P.: New high-resolution ozone absorption cross-sections in UV, visible and near infra red: Part II. Temperature dependence, *Atmos. Meas. Tech.*, 7, 625–636, 2014.

Weber, M., Gorshelev, V., and Serdyuchenko, A.: Uncertainty budgets of major ozone absorption cross-sections used in UV remote sensing applications, *Atmos. Meas. Tech.*, 9, 4459–4470, doi:10.5194/amt-9-4459-2016, 2016.

Delahaye, T., S. E. Maxwell, Z. D. Reed, H. Lin, J. T. Hodges, K. Sung, V. M. Devi, T. Warneke, P. Spietz, and H. Tran: Precise methane absorption measurements in the $1.64\mu\text{m}$ spectral region for the MERLIN mission, *J. Geophys. Res. Atmos.*, 121, 7360–7370, doi:10.1002/2016JD025024, 2016.

Derivation of Stratospheric Aerosol Extinction Profiles from SCIAMACHY Solar Occultation Measurements

Stefan Noël, Klaus Bramstedt, Alexei Rozanov, Elizaveta Malinina, Heinrich Bovensmann, and John P. Burrows

Between 2002 and 2012, the SCanning Imaging Absorption spectroMeter for Atmospheric CHartography (SCIAMACHY) on Envisat provided measurements of a large number of atmospheric constituents in different viewing geometries.

Here, we present results for stratospheric aerosol extinctions based on the analysis of SCIAMACHY solar occultation measurements at about 50-70°N (see Noël et al., 2020, for details).

The basic input for the aerosol retrieval are transmission spectra for different tangent altitudes. The derivation and calibration of these spectra is a complex task, mainly because the SCIAMACHY solar occultation measurements involve continuous vertical scans over the sun disk. This results in a variation of the measured signal, which needs to be corrected considering e.g. also effects of atmospheric refraction.

The retrieval method is a two-step approach, which consists of (1) an onion-peeling DOAS (Differential Optical Absorption Spectroscopy) retrieval (see e.g. Noël et al. 2018) to remove contributions of Rayleigh scattering and trace gas absorptions, and (2) a subsequent (also onion-peeling based) aerosol profile retrieval using as main input the transmissions at a given wavelength derived from the background polynomial fitted in step (1), see Figure 43.

The extinction retrieval method is in principle applicable to all measured wavelengths. Currently, we concentrate on 452, 525 and 750 nm, for which also correlative data sets are available.

Reasonable results are obtained between about 15 and 30 km altitude, see Figure 44. Collocated SAGE-II data (obtained from NASA-Langley) and results from the SCIAMACHY limb aerosol product V1.4 (see Rieger et al., 2018) are also shown.

Further comparisons (see Noël et al., 2020 for details) involving also other data sets reveal in general a very good agreement of extinctions at 452 and 525 nm. For 750 nm, the results of the comparisons are less conclusive as different offsets are observed for different instruments. A common feature of the SCIAMACHY solar occultation data is however the appearance of small vertical oscillations, which was also seen in corresponding trace gas products.

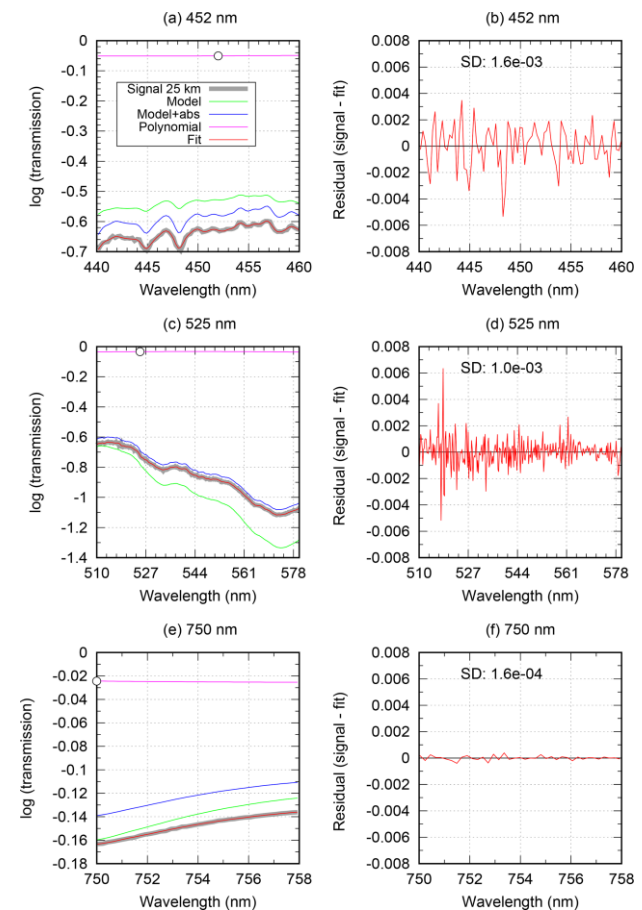


Figure 43: Onion peeling DOAS fit results for orbit 8014 (11 September 2003) (from Noël et al., 2020). The circle in the left plots marks the transmission value used in the subsequent extinction retrieval for the specific wavelength.

For the analysis of time series these oscillations are of minor importance, because they vanish after the computation of monthly anomalies, see Figure 45. These anomalies show at the lower altitudes clearly the increasing extinctions after major volcanic eruptions impacting higher latitudes and occurrences of polar stratospheric clouds (PSCs). Above 25 km a regular variation of extinctions is observed, which can be attributed to dynamical effects caused by the quasi-biennial oscillation (QBO).

References

Noël, S., K. Weigel, K. Bramstedt, A. Rozanov, M. Weber, H. Bovensmann and J. P. Burrows, Water vapour and methane coupling in the stratosphere observed using SCIAMACHY solar occultation measurements, *Atmos. Chem. Phys.*, 18(7), 4463-4476, 2018, doi: 10.5194/acp-18-4463-2018.

Noël, S., K. Bramstedt, A. Rozanov, E. Malinina, H. Bovensmann and J. P. Burrows, Stratospheric aerosol extinction profiles from SCIAMACHY solar occultation, *Atmos. Meas. Tech.*, 13(10), 5643-5666, 2020, doi: rm10.5194/amt-13-5643-2020.

Rieger, L. A., Malinina, E. P., Rozanov, A. V., Burrows, J. P., Bourassa, A. E., and Degenstein, D. A.: A study of the approaches used to retrieve aerosol extinction, as applied to limb observations made by OSIRIS and SCIAMACHY, *Atmos. Meas. Tech.*, 11, 3433–3445, <https://doi.org/10.5194/amt-11-3433-2018>, 2018.

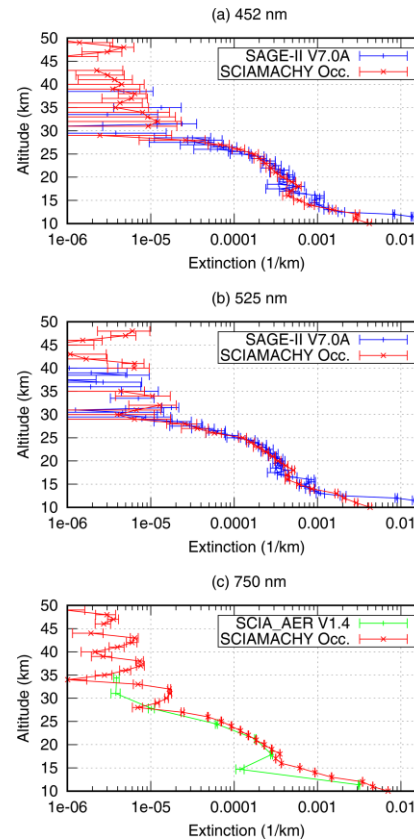


Figure 44: SCIAMACHY aerosol extinction profiles for orbit 8014 (from Noël et al., 2020).

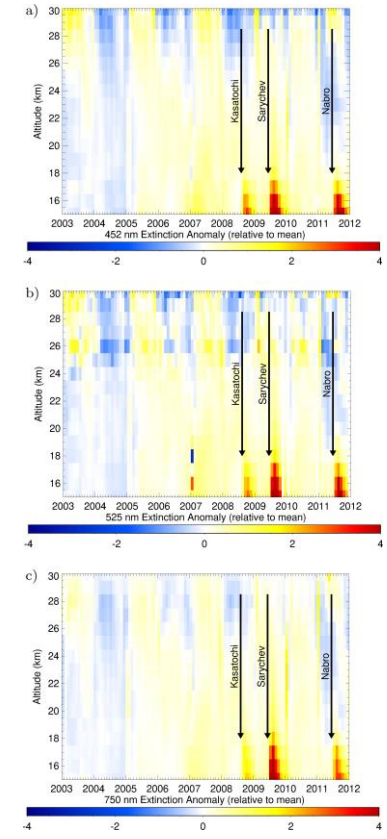


Figure 45: Time series of relative aerosol extinction anomalies from SCIAMACHY solar occultation for 452, 525 and 750 nm (from Noël et al., 2020).

Retrieval of aerosol optical thickness and surface parameters based on multi-spectral and multi-viewing space-borne measurements

Marco Vountas, Linlu Mei, and John P. Burrows

Aerosols in the terrestrial atmosphere play an important role at various levels. When extracted from their gaseous medium, they are frequently measured as particulate matter and are important air quality agents. Being able to reduce the visibility significantly, they also have an impact on aviation security. Moreover, they have a direct climate effect due to their ability to backscatter and absorb solar radiation. Furthermore, cloud-aerosol interaction remains a large uncertainty in predicting future climate. In this context, the Aerosol Optical Thickness (AOT) is an important parameter describing the overall atmospheric aerosol burden.

Several approaches are used to retrieve Aerosol Optical Thickness from satellite measurements. Different approaches provide different accuracies depending on the quality of the underlying retrieval assumptions and the quality of the underlying satellite data. Another aspect which governs the quality of the AOT retrieval is the overall information content provided by the satellite instrument.

Recent work at the Institute of Environmental Physics exploits the potential of the satellite instrument POLDER which used multi-spectral and multi-viewing capabilities for the retrieval of suspended liquid or solid particles in air (also known as aerosols), as well as surface properties. This instrument provides significant inherent information and is thought to be one of the best available choices for accurate AOT retrievals. This study aims at retrieving AOT and surface reflectance at high quality,

which are important quantities for the modelling community as well as crucial parameters for air quality assessment from space. The agreement of the first results with ground-based measurements, as shown in Figure 46 is very promising: the color-coded points at the centre of each station representing the ground-truth are close to the retrieved values based on satellite data shown in the surrounding.

Research in this area is of particular relevance because within the next decade, a fleet of upcoming satellite instruments will provide measurements similar to POLDER, which can be evaluated with the newly developed methodology.

Reference

Vountas, M., Belinska, K., Rozanov, V.V., Lelli, L., Mei, L., Jafarisera-jehlou, L., Burrow, J.P., Retrieval of aerosol optical thickness and surface parameters based on multi-spectral and multi-viewing space-borne measurements, *Journal of Quantitative Spectroscopy and Radiative Transfer*, 256, 2020, <https://doi.org/10.1016/j.jqsrt.2020.107311>

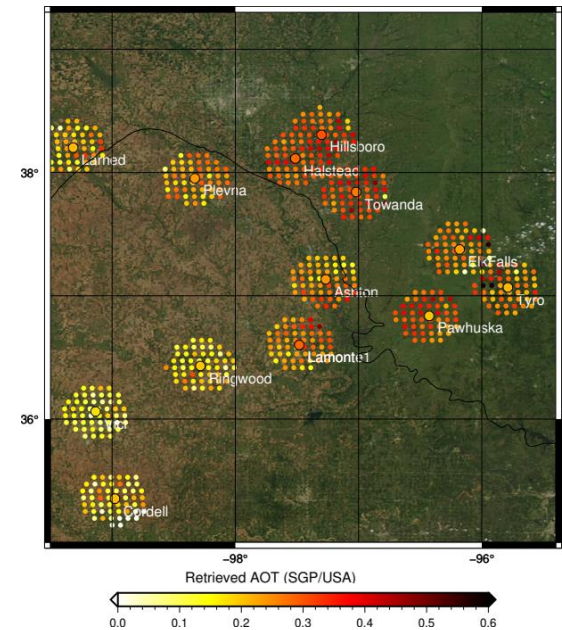


Figure 46: AOT retrieved using satellite data (POLDER) and ground-based measurements of AOT from ARM stations over central US.

Retrieval of Aerosol Optical Thickness in the Arctic Snow-Covered Regions Using Passive Remote Sensing: Impact of Aerosol Typing and Surface Reflection Model

Linlu Mei, Vladimir Rozanov, Marco Vountas, and John P. Burrows

In parallel but not methodologically identical to the study described in the previous section, an approach was developed which retrieves the AOT over snow and ice covered regions. Here, as well as in the above-mentioned companion study, data of POLDER have been used because of the high intrinsic information content of the instrument. The task of retrieving AOT over the cryosphere is even more challenging than for the mid- and low latitudes as the bright surface is highly variable and not well characterized. The cryosphere in the Arctic is of special importance because the Arctic environment faces rapid changes in many ways. One of the most important changes is Arctic Amplification, which refers to a recent surface air temperature increase in the Arctic, which is approximately twice as large as the global average. The reasons for this temperature change are thought to be dominated by atmospheric processes and a change in Arctic aerosols might play a subtle role.

Figure 47 shows the comparison of the retrievals with this novel approach compared to ground based measurements of AOT in the Arctic for the whole year of 2006. According to the figure, several features of the temporal evolution of the AOT over ground-based stations are well captured. Especially the so called Arctic Haze is retrieved very well using the new approach for POLDER data.

Reference

Mei, LinLu, Rozanov, V., Ritter, C., Heinold, B., Jiao, Z., Vountas, M., Burrows, J.P., Retrieval of Aerosol Optical Thickness in the Arctic Snow-Covered Regions Using Passive Remote Sensing: Impact of Aerosol Typing and Surface Reflection Model, in IEEE Transactions on Geoscience and Remote Sensing, vol. 58, no. 7, pp. 5117-5131, July 2020, <https://doi.org/10.1109/TGRS.2020.2972339>

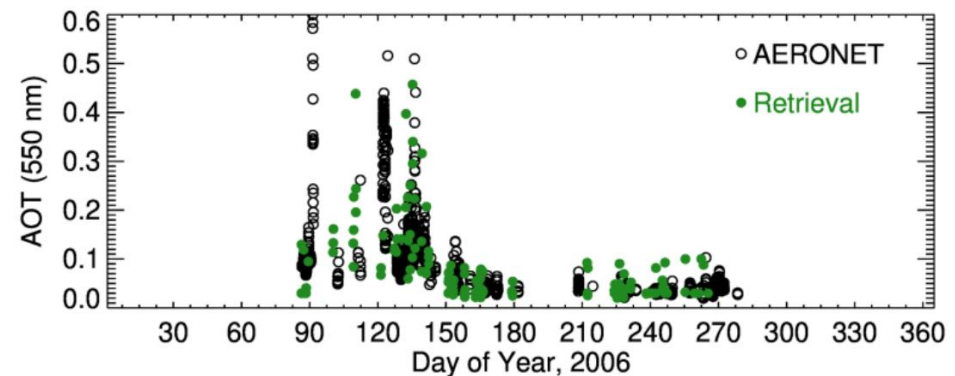


Figure 47: AOT retrieved using satellite data (POLDER) and compared to ground-based measurements of AOT from AERONET (a federated aerosol measurement network).

Extending Remote Sensing retrievals to Aerosol and Cloud Conditions

Marco Vountas, Vladimir Rozanov, Luca Lelli, Linlu Mei, and John P. Burrows

Aerosols may change cloud properties and their radiative properties, as well as perturb cloud lifetime, and the cloud precipitation efficiency. Therefore, aerosol particles are important players with respect to climatological considerations and within the hydrological cycle, mediated by the clouds, which act as water reservoirs in the atmosphere.

However, the satellite-based retrieval of cloud optical properties for aerosol contaminated water cloud is challenging. Conventionally, cloud optical data products are derived, ignoring the aerosol impacts on radiative transfer in the retrieval process. This is problematic in regions where aerosol is advected towards clouds. A region relevant for such mixed scenes is Western Africa where aerosol and clouds coexist. For example, about 80% of Saharan and Namibian dust aerosol cases are located above clouds, while about 60% of biomass burning aerosols are located within cloud. A new approach has thus been proposed which was validated and used over the Atlantic Ocean close to the dust and biomass burning sources.

Case studies illustrate that the retrieval algorithm shows reasonable and promising cloud and aerosol properties for the case when both cloud and aerosol exist. The consistent patterns (see Figure 48) compared to standard cloud products (which are typically not accounting for aerosol contamination) demonstrate that aerosol effects must be considered properly in the cloud retrieval to avoid biases in satellite-derived cloud properties.

Reference

Mei, L., Rozanov, V., Jethva, H., Meyer, K.G., Lelli, L., Vountas, M., Burrows, J.P., Extending XBAER Algorithm to Aerosol and Cloud Condition, in IEEE Transactions on Geoscience and Remote Sensing, vol. 57, no. 10, pp. 8262-8275, Oct. 2019, <https://doi.org/10.1109/TGRS.2019.2919910>.

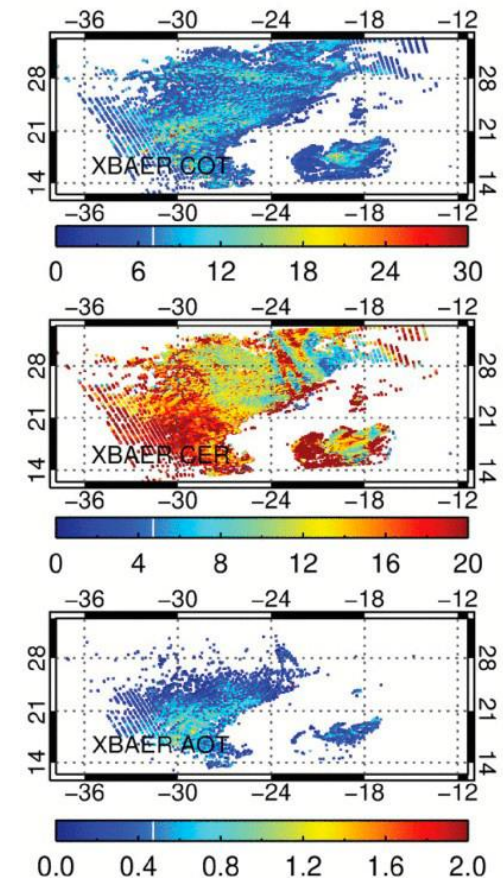


Figure 48: Retrievals of Cloud Optical Thickness (COT) and Cloud Effective Radius (CER) accounting for aerosol contamination and the retrieved Aerosol Optical Thickness (AOT) above the cloud.

Greenhouse gas observations from aircraft: Towards the next generation of the Methane Airborne Mapper

Konstantin Gerilowski, Sven Krautwurst, Jakob Borchardt, Michael Buchwitz, John P. Burrows, and Heinrich Bovensmann

Implementation of political measures for a global reduction of greenhouse gas emissions of carbon dioxide (CO₂) and methane (CH₄) necessitates an effective monitoring of these gases. Both, CO₂ and CH₄ have strong sources on small spatial scales (point sources to a few km). These include for example CO₂ from power plants, volcanoes and cities, or CH₄ from fossil fuel production (coal, gas, oil), landfills and geological seeps. Airborne remote sensing of atmospheric GHG distributions, so-called greenhouse gas imaging, could close an important information gap on small spatial scales. At IUP Bremen, the development and application of the airborne spectrometer system called MAMAP (Methane Airborne Mapper) demonstrated that imaging the spatial distribution of atmospheric GHG concentrations in the vicinity of strong sources can be used to infer the emission strength of the sources. The spectrometer uses solar absorption spectroscopy in the near and short-wave infrared, similar to the satellite sensors SCIAMACHY, GOSAT, or Sentinel-5P to derive very accurate (precision better < 0.3%) gradients in atmospheric CO₂ and CH₄ with a spatial resolution of approx. 50 m over spatial scales of several km.

During the years 2019 – 2020, the main focus of the MAMAP group at IUP Bremen was the data analysis of the COMET measurement campaign in Upper Silesian Basin (Poland) in

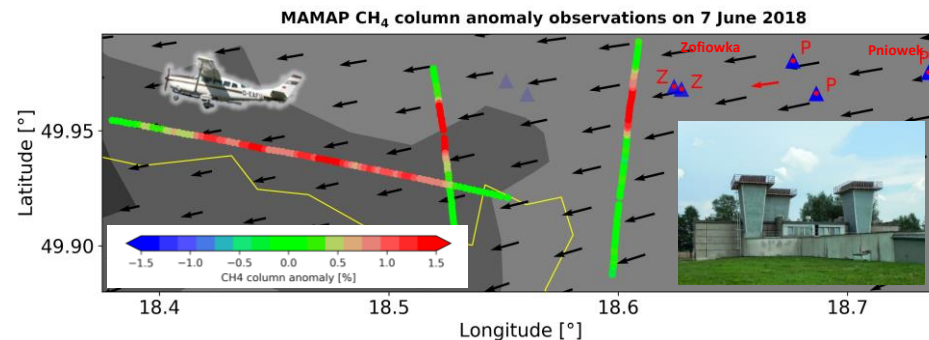


Figure 49: CH₄ plume as measured by MAMAP during the COMET campaign. The plume is originating from a cluster of coalmine ventilations shafts (blue triangles). Emissions of approx. 9.2 tCH₄/hr were derived from the data, which agree within their error bars with the reported emissions of 9.7 tCH₄/hr (Krautwurst et al., 2020).

2018 and the development of the successor of MAMAP, the MAMAP2D system.

The coal mining area in the Upper Silesian Basin around the city of Katowice, Poland, is the largest sources of methane gas emissions in Europe and was the focus of the COMET (Carbon dioxide and Methane Mission) measurement campaign in May/June 2018. The IUP instrument MAMAP was flown on board the Cessna aircraft owned by the Free University of Berlin, to collect data on CH₄ emissions from coalmine ventilation shafts. We use these airborne remote sensing observations in combination with wind field data to assess bottom-up estimates of coal mining emissions. The analysis reveals that emissions from small groups of shafts can be disentangled (see Figure 49). Comparison to known hourly emissions, where available, shows good agreement with the computed fluxes within the uncertainties (Krautwurst et al., 2020).

Beside the analysis of the data from the COMET campaign, the team at IUP Bremen also prepared for a new campaign (HALO COMET 2.0 Arctic) in late summer 2022 and continued

the development of the 2-dimensional imaging sensor for CH₄ and CO₂ quantification, MAMAP2D. Despite the difficulties encountered as result of the measures taken to limit the spread of the COVID-19 pandemic, some good progress was made in the areas of 2D data analysis using AVIRIS-NG data (Borchardt et al., 2020) and integration of the MAMAP2D prototype sensor (see Figure 50). MAMAP2D will allow to perform similar measurements as MAMAP (1D), but on time scales of approx. 10 minutes instead to several hours. This will improve the detection limit for small sources by nearly an order of magnitude, thereby opening new application areas for the instrument.

The activities of the IUP MAMAP team are funded by the DFG (COMET), the BMBF (via DLR-PT, AIRSPACE project) and the University of Bremen.

References

Borchardt, J., Gerilowski, K., Krautwurst, S., Bovensmann, H., Thorpe, A. K., Thompson, D. R., Frankenberg, C., Miller, C. E., Duran, R. M., and Burrows, J. P.: Detection and Quantification of CH₄ Plumes using the WFM-DOAS retrieval on AVIRIS-NG hyperspectral data, *Atmos. Meas. Tech. Discuss.*, <https://doi.org/10.5194/amt-2020-275>, in review, 2020.

Krautwurst, S., Gerilowski, K., Borchardt, J., Wildmann, N., Galkowski, M., Swolkien, J., Marshall, J., Fiehn, A., Roiger, A., Ruhtz, T., Gerbig, C., Necki, J., Burrows, J.P., Fix, A., Bovensmann, H., Quantification of CH₄ coal mining emissions in Upper Silesia by passive airborne remote sensing observations with the MAMAP instrument during CoMet, submitted to *Atmospheric Chemistry and Physics (ACP)*, MS No.: acp-2020-1014, 2020.

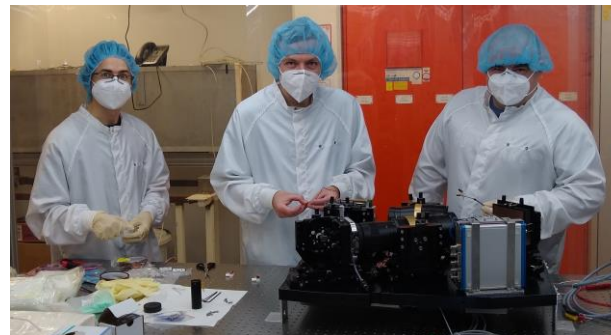


Figure 50: MAMAP Team during integration of the MAMAP2D prototype sensor.

Transport of atmospheric pollution originating in European major population centres

Maria Dolores Andrés Hernández, Midhun George, Yangzhuoran Liu, John P. Burrows, and the EMeRGe team.

The atmospheric effect of pollutants originating in large urban conurbations and megacities is a central point of investigation of the DFG project EMeRGe (Effect of Megacities on the Transport and Transformation of Pollutants on the Regional to Global scales, www.iup.uni-bremen.de/emerge/). EMeRGe is a German consortium of five universities and five research centres under the scientific coordination of IUP at the University of Bremen. In addition, 50 other institutions from 16 countries are currently involved in the international research partnership named EMeRGe international for facilitating a comprehensive integrated analysis of complementary observations.

The EMeRGe intensive observational period in July 2017 focused on the investigation of European major population centres (MPCs). Overall, EMeRGe strives for the identification of MPCs as pollution hotspots and of emission signatures in MPC plumes. With this purpose, seven scientific flights on board of the research aircraft HALO (www.halo.dlr.de) were carried out over Europe from the German DLR HALO base in Oberpfaffenhofen. For the interpretation of results, the HALO airborne measurements of trace gases and aerosol particles are combined with satellite and ground-based observations and modelling.

In Europe, the level of urbanisation is presently at 74% and is expected to further increase by 10% until the mid of the century (United Nations, 2019). Generally, the MPCs are large urban conur-

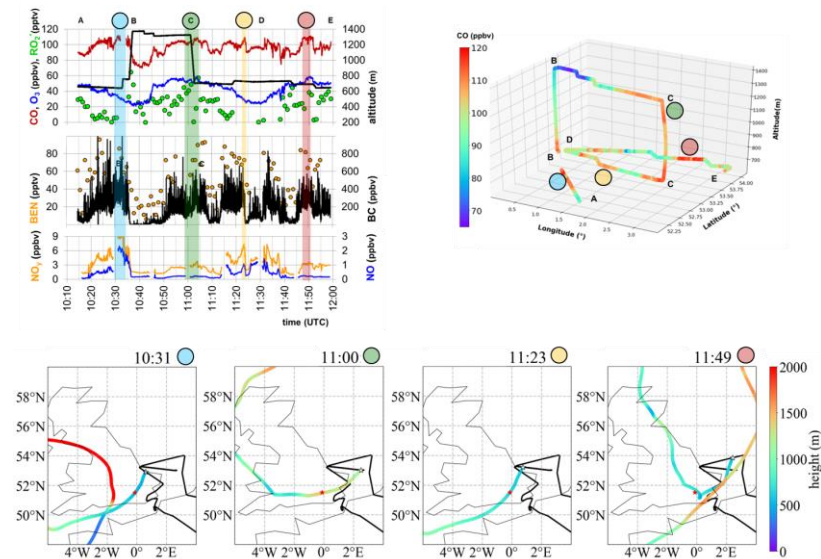


Figure 51: Example of pollution plumes probed during the EMeRGe flight on 26.07.2017. The backward trajectories (bottom) confirm the contact of the probed air masses with the outflow of London (red star). The position of HALO over the flight track (in black) is indicated (white star). Mixing ratios measured by IPA-DLR (CO, O₃, NO and NO_y), IUP-UB (sum of peroxy radicals, RO₂*), KIT (benzene, BEN) and MPIC (black carbon, BC) are depicted (top left). On the top right, this part of the 3-D flight track, colour coded with measured CO mixing ratios, is also shown. Capital letters indicate main track changes.

bations and the number of European megacities, such as London and Paris, still remains scarce.

Figure 51 shows an example of pollution plumes with origin in the London megacity, probed during the EMeRGe flight on 26.07.2017. The HALO aircraft carried out a shuttle at two altitudes (600m and 1200m) to determine the vertical extension of the transported pollution. Air mass backward trajectories support the identification of the London outflow.

Pollutants originating in MPCs can heterogeneously mix during transport with biomass burning (BB) and mineral dust plumes. BB events from agriculture or wildland fires present a strong seasonal pattern (Barnaba et al., 2011). Similarly to MPCs, wildfires emit large amounts of pollutants such as black carbon (BC), nitrogen oxides (NO_x) carbon monoxide (CO) and volatile organic compounds (VOC). In addition, plumes of mineral dust originating in North Africa are frequently reaching the Mediterranean facilitating loss processes and heterogeneous reactions at the dust surface (Pey et al., 2013). Therefore, BB and dust have a variable impact on the total European burden of atmospheric aerosol and trace gases, increase the chemical complexity of the air masses and can therefore significantly affect the chemical processing of pollution plumes of MPC origin.

Urban plumes with BB signatures were frequently probed during EMeRGe in Europe as shown in Figure 52 for the HALO flight on 24.07.2017. Emissions from forest fires located between Nice and Marseille mixed with urban pollution at the coast. The concentration of most of the trace gases observed in different polluted plumes is of a similar order of magnitude. Therefore, different indicators for BB and anthropogenic pollution such as acetonitrile (ACN), black carbon (BC), and benzene (BEN) must be used to classify the air masses.

References

United Nations, Department of Economic and Social Affairs, Population Division World Urbanization Prospects: The 2018 Revision (ST/ESA/SER.A/420). New York: United Nations, 2019.

Barnaba, F., Angelini, F., Curci, G., and Gobbi, G.P.: An important fingerprint of wildfires on the European aerosol load, *Atmos. Chem. Phys.*, 11, 10487–10501, doi: 105194/acp-11-10487-2011, 2011.

Pey, J., Querol, X., Alastuey, A., Forastiere, F., and Stafoggia, M.: African dust outbreaks over the Mediterranean Basin during 2001–2011: PM₁₀ concentrations, phenomenology and trends, and its relation with synoptic

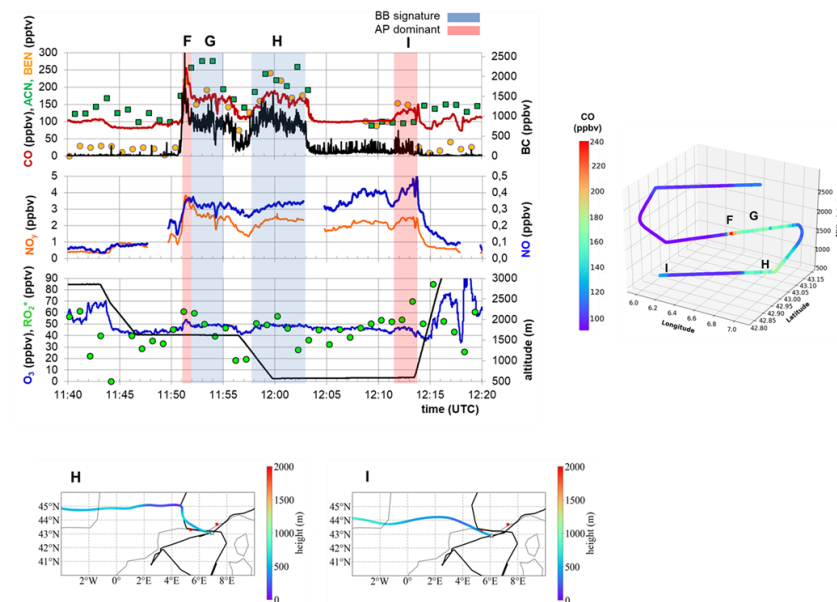


Figure 52: Example of plumes with anthropogenic (AP) and biomass burning (BB) signatures probed during the EMeRGe flight on 24.07.2017. Mixing ratios measured by IPA-DLR (CO, O₃, NO and NO_y), IUP-UB (sum of peroxy radicals, RO₂*), KIT (acetonitrile, ACN, benzene, BEN) and MPIC (black carbon, BC) are shown (top left). The threshold for ACN and BEN are 184 pptv and 53 pptv respectively. In the bottom plots, back trajectories of the H and I plumes probed along the flight track (in black) confirm that emissions from fires between Nice and Marseille (red stars) were probed at 1500 and 500 m at the coast. On the top right, this part of the 3-D flight track, colour coded with measured CO mixing ratios, is also depicted. Capital letters indicate the plumes investigated.

and mesoscale meteorology, *Atmos. Chem. Phys.*, 13, 1395–1410, doi: 10.5194/acp-13-1395-2013, 2013.

Acknowledgments

The authors acknowledge funding by the University of Bremen, the state of Bremen, and the HALO SPP 1294 grant from the DFG. Special thanks to Helmut Ziereis, Eric Förster, Bruna Holanda, Ovid Krüger, Andreas Hilboll and Anna Hedegaard for facilitating the EMeRGe data shown in this contribution.

Assessing the impact of natural dust on air quality using TM4-ECPL

Medea Zanolì, Nikos Daskalakis, and Mihalis Vrekoussis

The world's large arid and semi-arid regions emit every year into the atmosphere great quantities of particulate matter in the form of natural dust, which, entrained by the winds, can travel thousands of kilometres from their sources before being removed. Mineral dust can cause significant damage to human health: during major dust events, the amount of deposited PM in the human lungs can be comparable to that experienced in heavily polluted urban areas, increasing the risk of respiratory diseases, cardiovascular complications and premature death (Mitsakou et al., 2008).

Dust emissions are highly sensitive to climate change and have been consistently rising during the last decade (Prospero et al., 2003). The ongoing desertification in many areas of the world is predicted to increase the future atmospheric dust load (Grin et al., 2001). Thus, the study of the transport of natural dust from the world's dry regions and the estimate of its contribution to the total PM₁₀ is nowadays of particular interest for policymakers and scientists.

For this study, we use the well-documented TM4-ECPL model (Myriokefalitakis et al., 2016). TM4-ECPL is an Eulerian chemistry and transport model. Originally, dust emissions were imported from the AEROCOM (AEROSol Comparisons between Observations and Models) inventory (Dentener et al., 2006, Marticorena and Bergametti, 1995). Alternatively, an online dust emission scheme can be used in the TM4-ECPL model to

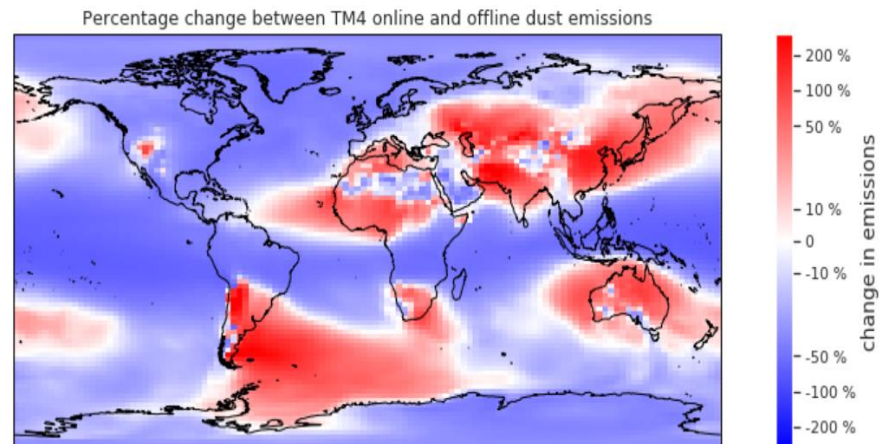


Figure 53: Percentage change in natural dust simulated surface concentration [C] when using online emission scheme with respect to an offline one in the TM4-ECPL model, calculated as: $(\text{online}[C] - \text{offline}[C]) / \text{offline}[C]$. The plotted result is the average over the time period 2000 – 2014.

account for dust production calculated according to physical, geological and meteorological parameters.

We showed (Figure 53) that using an online scheme instead of an offline one leads to major changes in the simulated global dust load distribution. At the present date, the validation of the online emission scheme showed that online emission produces better agreement with observations (Figure 54).

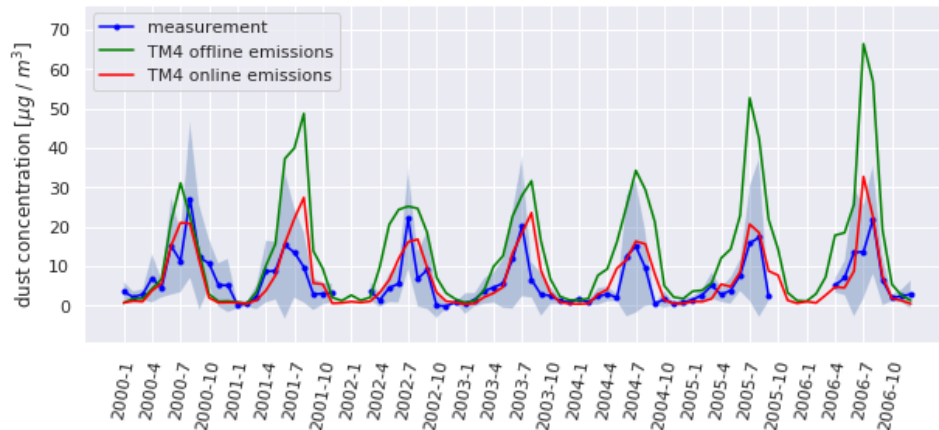


Figure 54: Surface dust concentration in Miami measured by the Rosenstiel School of Marine and Atmospheric Science between the years 2000 and 2006, compared against the values simulated by the online (red) and offline (green) TM4 emissions scheme. The shaded area corresponds to the measurements standard deviations

We intend to use the online version of the TM4-ECPL to study PM_{10} speciation for days on which the European Directives for air quality were not met to assess to which percentage natural dust contributed to the limit exceedance.

References

Mitsakou, C., Kallos, G., Papantoniou, N., Spyrou, C., Solomos, S., Astitha, M., and Housiadas, C.: Saharan dust levels in Greece and received inhalation doses, *Atmos. Chem. Phys.*, 8, 7181–7192, <https://doi.org/10.5194/acp-8-7181-2008>, 2008.

Prospero, J. M., Lamb, P. J., African Droughts and Dust Transport to the Caribbean: Climate Change Implications. *Science*, 302, 1024-1027, 2003.

D. Grin, C. Kellogg, E. Shinn. Dust in the wind: long range transport of dust in the atmosphere and its implications for public and ecosystem health. *Global Change Human Health*. 2001; 2:21-5.

Myriokefalitakis, S., Nenes, A., Baker, A. R., Mihalopoulos, N., and Kanakidou, M.: Bioavailable atmospheric phosphorous supply to the global ocean: a 3-D global modeling study, *Biogeosciences*, 13, 6519–6543, <https://doi.org/10.5194/bg-13-6519-2016>, 2016.

Dentener, F., Kinne, S., Bond, T., Boucher, O., Cofala, J., Generoso, S., Ginoux, P., Gong, S., Hoelzemann, J. J., Ito, A., Marelli, L., Penner, J. E., Putaud, J.-P., Textor, C., Schulz, M., van der Werf, G. R., and Wilson, J.:

Emissions of primary aerosol and precursor gases in the years 2000 and 1750 prescribed data-sets for AeroCom, *Atmos. Chem. Phys.*, 6, 4321–4344, <https://doi.org/10.5194/acp-6-4321-2006>, 2006.

B. Marticorena and G. Bergametti. Modeling the atmospheric dust cycle: 1. Design of a soil-derived dust emission scheme. *JGR*, Vol. 100, No. D8, pag. 16,415-16,430, August 20, 1995

Assessment of the impact of OH's temporal resolution on the global atmosphere

Sofía Gómez Maqueo Anaya, Nikos Daskalakis, and Mihalis Vrekoussis

The hydroxyl radical (OH) is an important oxidizer and a cleansing agent of the atmosphere. OH reacts with several other chemical compounds, being the dominant path for the removal of a variety of halocarbons, hydrocarbons, volatile organic compounds, carbon monoxide, among others. Therefore, modelling its concentration accurately is crucial for the calculations of the concentrations of other atmospheric chemical compounds and the overall description and prediction of atmospheric chemicals.

Since 1990, the set of OH concentrations widely known in the atmospheric modelling community as 'climatological data' has been used in various projects, mostly in those that involve inverse modelling and data assimilation. However, the above dataset has a coarse spatial (10° longitude x 8° latitude) and temporal resolution (monthly means). This study aimed at providing a more accurate description of OH values in the atmosphere than the coarse 'climatological data'. Towards

this direction, we developed a new group of OH mixing ratio values with varying spatial and temporal resolutions. The datasets were calculated assuming that the 'true' values of OH mixing ratio are the ones calculated daily and hourly from the chemistry and transport model, TM5-MP.

An assessment of whether the new OH mixing ratios provide better accuracy or not compared to the climatological data was done through lifetime calculations of methane and isoprene (Figure 57), and a comparison to the literature reported values

March, April & May mean sunrise value

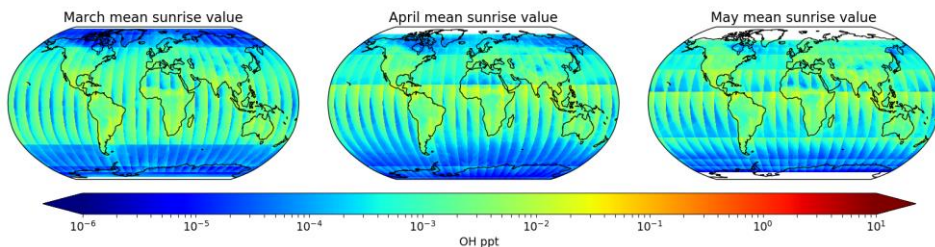


Figure 56: Example of the created OH mixing ratio data sets for sunrise hours per latitudinal band for the months of March, April and May.

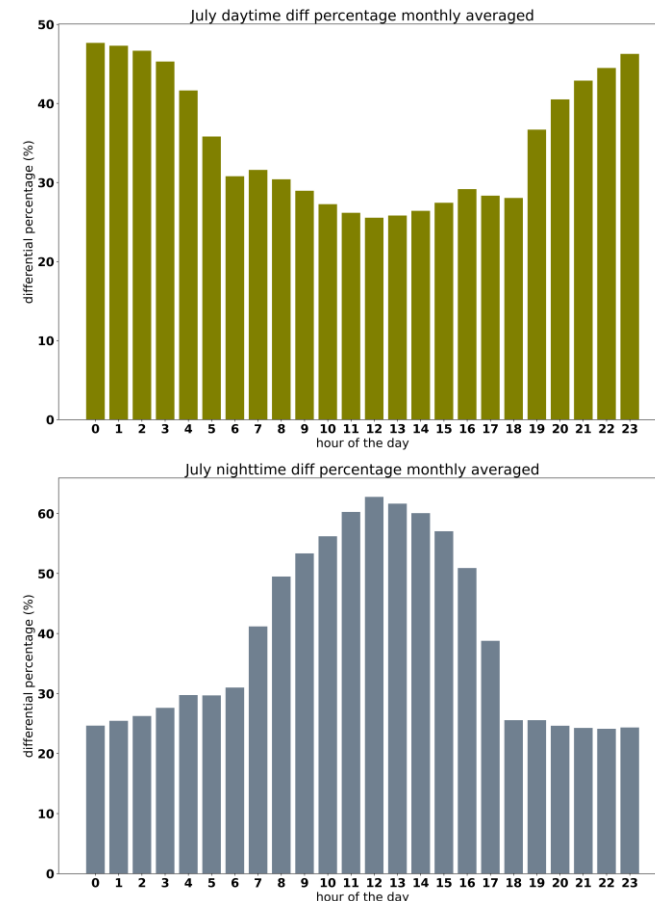


Figure 55: Differences between monthly averaged values per hour and the hourly, daily output provided from the TM5-MP. Higher differences are found during polar night and polar day since small variations on already small values have a higher impact than small variations of relatively bigger values. It is evident that the higher differences (without including polar night/day) are found during the typical sunrise/sunset hours.

Through the analysis of the loss of accuracy from coarsening temporal resolution, the conclusion could be drawn that a more accurate way of representing mixing ratio values for OH than monthly values was a separation between night-time, sunrise, daytime and sunset values per latitudinal band. This separation was done through the calculation of solar zenith angle values.

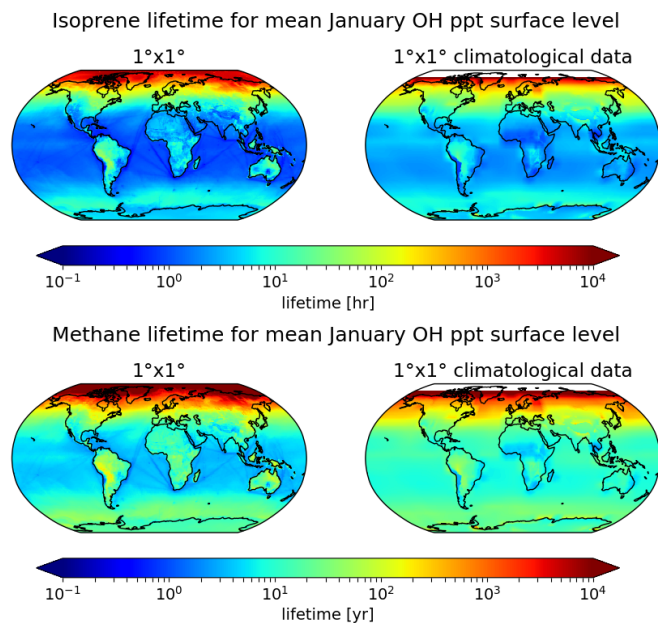


Figure 57: Isoprene (top) and methane (bottom) lifetime calculations using January OH values. On the left: the calculation done with TM5-MP values, on the right: calculations done with the climatological data interpolated to 1°x1° (from their native 10°x8° resolution)

References

- Williams, J. E., Boersma, K. F., Sager, P. L., and Verstraeten, W. W. (2017). The high resolution version of TM5-MP for optimized satellite retrievals: description and validation. *Geoscientific Model Development*, 10(2):721–750.
- Spivakovsky, C.M., Logan, J. A., Montzka S. A., Balkanski Y. J., Foreman-Fowler M., Jones D. B. A., Horowitz L. W., Fusco A.C., Brenninkmeijer C. A. M., Prather M. J., Wofsy S. C. and McElroy M. B. (2000). Three-dimensional climatological distribution of tropospheric OH: Update and evaluation. *Journal of Geophysical Research – Atmospheres*, 105(D7), 8931-8980.

Enhancing chemical schemes accounted in FLEXPART v10.4 transport model using a kinetic pre-processor

Ruben Sousse, Andreas Hilboll, Nikos Daskalakis, and Mihalis Vrekoussis

In this project, two main developments have been performed on the FLEXPART v10.4 atmospheric Lagrangian transport model to enhance its chemical scheme.

First, OH fields from the global CTM TM5-MP have been made available as input for FLEXPART, replacing its default OH fields, coming from the GEOS-Chem model that are outperformed in terms of spatial and temporal resolution, among others (Figure 58). Second, a box model produced using the kinetic pre-processor (KPP) has been coupled to FLEXPART as its chemical solver. It is based on the Rosenbrock Rodas-3 numerical integrator and replaces the previous parametrized chemical reaction based on direct time-discretization (Figure 59).

These developments have been validated in terms of reproducibility with respect to FLEXPART version 10.4 in two different sets of experiments: 1) a set of global simulations for each FLEXPART OH-reacting species (methane, ethane, PCB28 and γ -HCH) where the total mass present in the atmosphere is evaluated and, 2) a validation experiment against observational data is attempted through a simula-

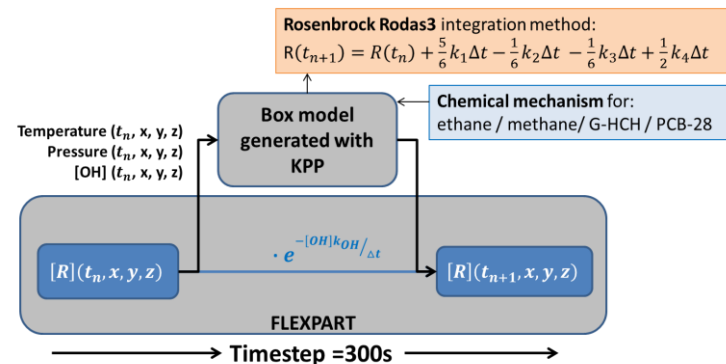


Figure 59: Coupling scheme between the box model generated with KPP and FLEXPART.

tion emulating CMIP6 ethane emissions at European level. All the experiments were performed for each development stage separately (i.e. implementation of TM5-MP OH fields and KPP coupling) in order to evaluate each one of them.

The validation results show that the new developments cause an overall slight increase of the OH sink rate for all the species, especially for those short-lived species like γ -HCH (Figure 60). The detailed analysis of the global ethane simulation shows that most of the differences are region-independent at the surface, and they are caused mainly by the TM5-MP OH fields implementation rather than the change of chemical solver. Finally, no relevant conclusions could be obtained from the observational validation results due to computational limitations that prevented the release of a sufficient number of particles in the simulation (Figure 61). Although the new developments could not be validated against observational data and therefore their effect could not be quantified, the results' reproducibility seems to indicate that the new implementations should not affect simulations' results significantly in future experiments.

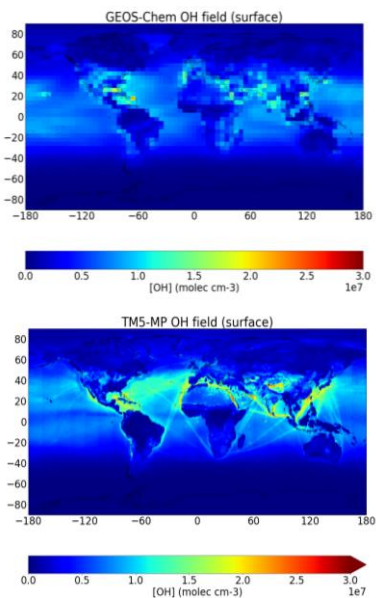


Figure 58: June, July and August averaged surface OH concentration fields from GEOS-Chem simulation (2005, top) used by default in FLEXPART and from the newly implemented TM5-MP simulation (2017, bottom). Noon local time.

Making the TM5-MP concentration fields available as input to FLEXPART together with the coupling of KPP-produced box models signifies an increase in the adaptability of FLEXPART to a wide range of contexts. The developments performed in this project open the doors to expand the FLEXPART chemical mechanism (currently limited to the OH oxidation of four species) to virtually any set of reactions required, setting the path for an enhancement in FLEXPART simulations' quality.

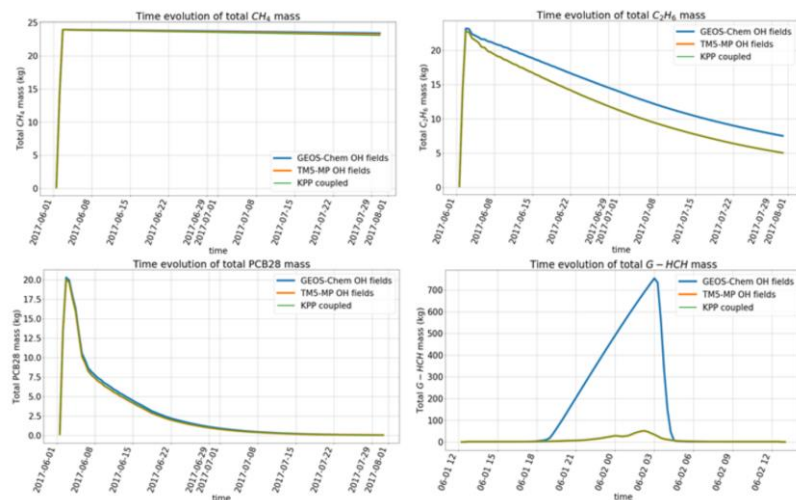


Figure 60: Validation of the KPP coupling for each FLEXPART species reacting with OH. In each figure, three lines are shown corresponding to the three validation simulations: default FLEXPART, FLEXPART using TM5-MP OH fields and FLEXPART using TM5-MP OH fields coupled with KPP. Release of 1kg/h during the first 24h of the simulation. For G-HCH, 24t were released to make the atmospheric concentration observable. Note the change of time scale for the G - HCH case because of this effect.

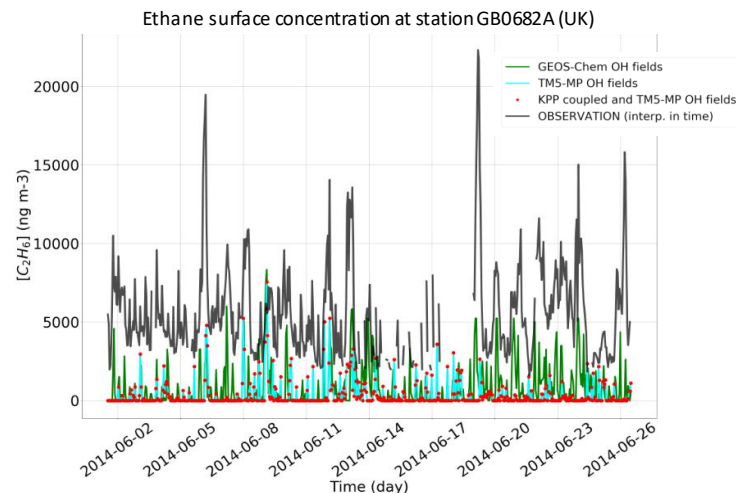


Figure 61: Validation of the KPP coupling with observational data. Observational time series (black), the simulation with default FLEXPART (green), with FLEXPART and only TM5 OH fields (cyan) and with TM5-MP OH fields and coupled KPP (red dots).

References

- Brasseur, G. and Jacob, D., Modeling of Atmospheric Chemistry. Cambridge University Press, 201.
- Damian, V., Sandu, A., Damian, M., Potra, F., and Carmichael, G. R., The kinetic preprocessor KPP – a software environment for solving chemical kinetics. Computers & Chemical Engineering, 26(11):1567–1579, 2002.
- Stohl, A., Hittenberger, M., and Wotawa, G., Validation of the Lagrangian particle dispersion model Flexpart against large-scale tracer experiment data. Atmospheric Environment, 32(24):4245 – 4264, 1998.
- Williams, J. E., Boersma, K. F., Sager, P. L., and Verstraeten, W. W., The high resolution version of TM5-MP for optimized satellite retrievals: description and validation. Geoscientific Model Development, 10(2):721–750, 2017.

Combining HERMESv3 and TM5-MP

Sarah-Lena Meyer, Nikos Daskalakis, and Mihalis Vrekoussis

Atmospheric chemistry models need a variety of input data to work. Among those data, one important category is the emission data that are provided by the several groups that produce them as emission inventories. The various emission inventories do not follow a specific convention on deploying data, resulting in emission data in various file formats, data formats etc. This causes major problems in implementing different emission data in atmospheric models, leading to either delay in incorporation of new data or even limitation on the usage of different data in the model, limiting this way the research opportunities, especially for air quality studies.

In order to resolve the above-mentioned problem, the EARTH Sciences Department at the Barcelona Supercomputing Center developed the ‘High-Selective Resolution Modelling Emission System version 3’ (HERMESv3) (Guevara et al, GMD, 2019). This emission pre-processor promises to unify the format and

structure of several sets of emission databases to a common output for use in a model, simplifying this way the process of including emissions to models, but also the complexity of the emission code of the model itself.

In addition to the simplification in the technical parts, the HERMESv3 provides the opportunity to easily manipulate the final dataset, providing the users with the ability to easily construct “what if” emission scenarios. An illustration of a “what if” scenario is presented in the figures. Figure 62 shows the emission of black carbon from industry and transport as reported by the CMIP 6 emission dataset for the extended region of China and processed by HERMESv3 tool. In

Figure 63, four different emission scenarios were constructed for that region, where we first reduced the emissions from

Emissions for transport and industry from CMIP6

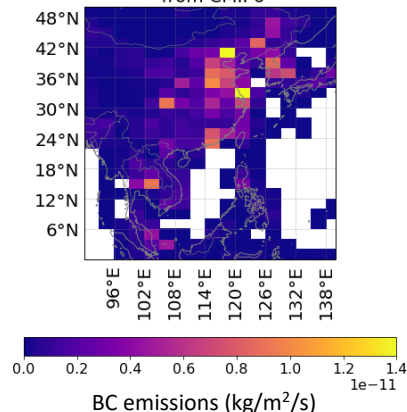


Figure 62: BC emissions over China as provided by the CMIP6 database

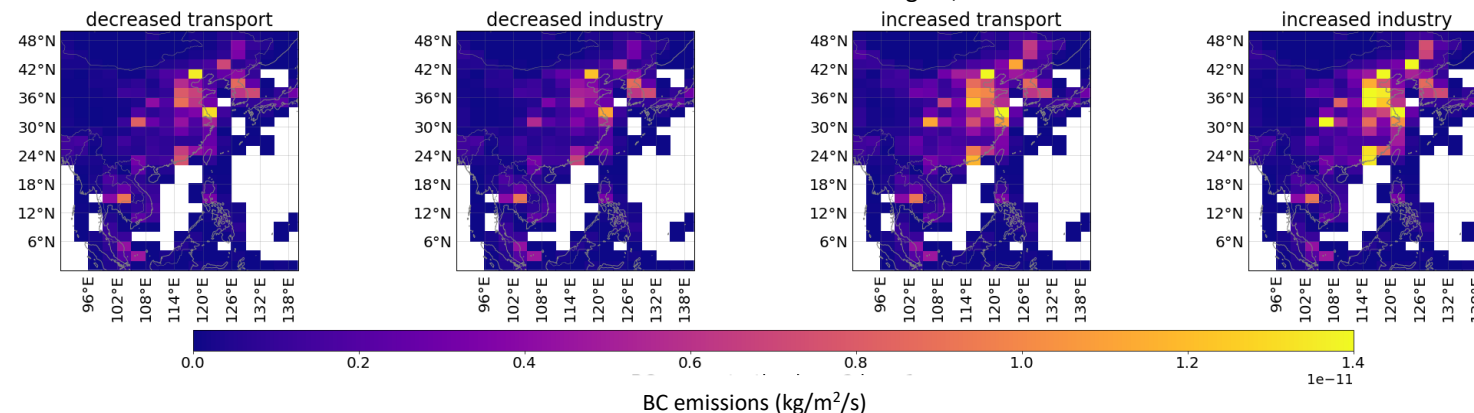


Figure 63: BC emissions over China for different scenarios (decreased transport, decreased industry, increased transport, increased industry)

transport by 20% (left panel), then the emissions from industry by 20% (middle-left panel), then we augmented the emissions from transport by 20% (middle-right panel) and in the final scenario we augmented the emissions from industry by 20% (right panel). The resulting differences in fluxes between the base case (Figure 62) and each emission scenario is presented in Figure 64. The resulting files always have the same, user defined, file and data format. As a result, incorporation of scenarios in the model becomes a trivial task.

The global and regional module of the pre-processor allows to create input data for a variety of models, such as WRF-CHEM, CMAQ and NMMB-MONARCH, by using different emission inventories. For using the tool at LAMOS in the most effective way, it was modified to create input data for TM5-MP. Parallel to this TM5-MP is simplified to only read emissions as produced by HERMES. This way, it will be possible to perform various case studies by editing the input emissions using HERMESv3 and study the effects of these changes using TM5-MP.

References

Guevara, M., Tena, C., Porquet, M., Jorba, O., and Pérez García-Pando, C.: HERMESv3, a stand-alone multi-scale atmospheric emission modelling framework – Part 1: global and regional module, *Geosci. Model Dev.*, 12, 1885-1907, <https://doi.org/10.5194/gmd-12-1885-2019>, 2019.

Williams, J. E., Boersma, K. F., Sager, P. L., and Verstraeten, W. W., The high resolution version of TM5-MP for optimized satellite retrievals: description and validation. *Geoscientific Model Development*, 10(2):721–750, 2017.

Myriokefalitakis, S., Daskalakis, N., Gkouvousis, A., Hilboll, A., van Noije, T., Williams, J. E., Le Sager, P., Huijnen, V., Houweling, S., Bergman, T., Nüß, J. R., Vrekoussis, M., Kanakidou, M., and Krol, M. C.: Description and evaluation of a detailed gas-phase chemistry scheme in the TM5-MP global chemistry transport model (r112), *Geosci. Model Dev.*, 13, 5507–5548, <https://doi.org/10.5194/gmd-13-5507-2020>, 2020.

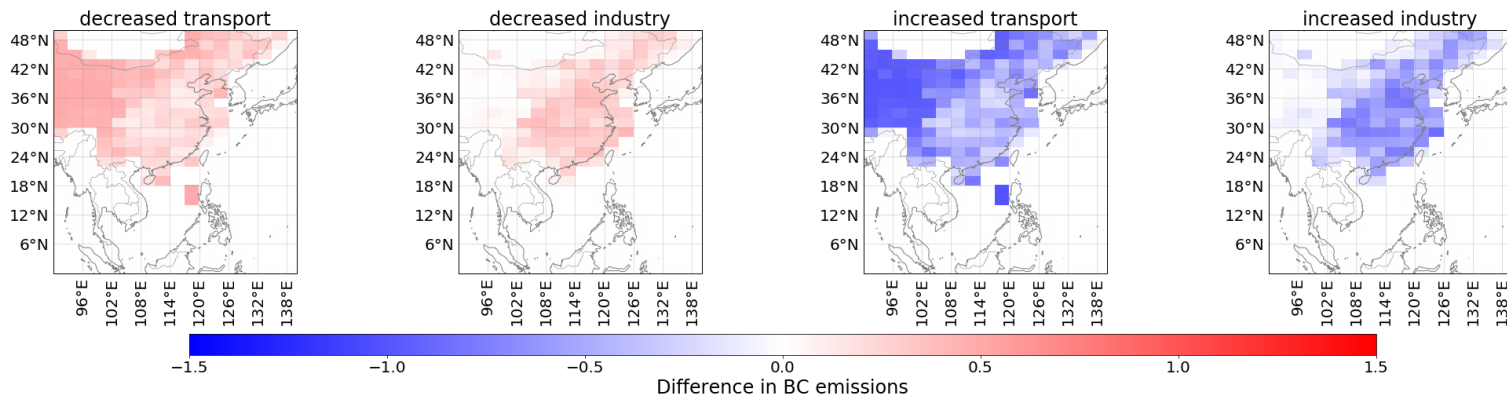


Figure 64: BC emission difference between base case (Figure 62) and scenarios (Figure 63)

Top-down CO emission inversions using TM5-4dvar and TROPOMI

Johann Rasmus Nüß, Nikos Daskalakis, Oliver Schneising, Michael Buchwitz, and Mihalis Vrekoussis

This study aims at optimizing the carbon monoxide (CO) emissions of the two large wildfires in Camp and Woolsey, California, that started on November 8th, 2018 and raged for multiple weeks. To this end, the TM5-4dvar inverse model has been used to optimize the CO emissions from biomass burning, and the CO produced from the oxidation of VOCs and methane (CH₄) on a global scale from October to December 2018.

The Global Fire Emissions Database, Version 4 (GFEDv4.1s, Randerson et al., 2017) has been used as biomass burning a priori, with an a priori error of 50%, whereas the chemical CO production was taken from the TM5-MP model with extended chemistry (Myriokefalitakis et al., 2020) and afflicted with a 10% error. Anthropogenic CO emissions were not optimized and based on CMIP6. The TM5-4dvar model is an offline model, with transport driven by ECMWF era interim meteorology and has a very simplified chemistry scheme that only covers the chemical loss of CO to OH, which in turn was based on the climatological fields by Spivakowsky et al. 2000, scaled by 0.92. Dry deposition was considered as an additional loss term. Initial concentrations fields were obtained from a 5 month spin up inversion from May to September 2018 with an identical setup. A 1° x 1° zooming region was set up over North America, around the region of interest. In comparison, the rest of the globe was simulated at 6° x 4° to save computational resources. This global approach was needed because, considering the relatively long lifetime of CO of about one month, long-range transport is relevant for the local background.

The inversions were constrained by TROPOMI CO satellite observations and NOAA surface flask stations. With this input, the model found, in

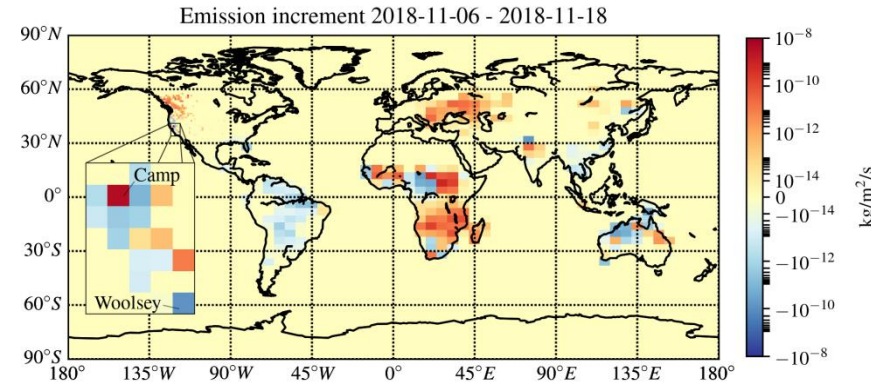


Figure 65: Biomass burning CO increment for the main burning period of the Camp and Woolsey wild fires based on TM5-4dvar and TROPOMI observations.

an iterative process of alternately going forward and backward in time, the set of emissions that lead to concentrations as close as possible to the observations while not differing too much from the initial emissions.

Figure 65 shows the resulting biomass burning emission increment, i.e., the change from the initial (a priori) to the final (a posteriori) emissions. Within the region of interest (highlighted in the inner box), the integrated emission increment over the main burning period (first ten days after either fire, period starts on the 6th for purely technical reasons) shows only a slight increase (~12%) compared to GFED4.1s; however, most of this increment seems to be aggregated in the pixel that contains Camp, while the adjacent pixels, as well as the one containing Woolsey, show minor negative increments.

However, as mentioned initially, not only the biomass burning CO emissions were optimized but also, simultaneously, the CO production from VOCs and CH₄. This approach is necessary because often, discrepancies in the background concentrations can be mostly attributed to an imperfect estimation of the chemical production of CO, while local peaks usually correspond to emissions from biomass burning instead.

Additionally, chemical CO production makes up roughly half of the total atmospheric source, whereas biomass burning contributes only about a quarter, emphasizing the need to consider the former. On the other hand, this makes it somewhat possible to tell the production source apart from the biomass burning source because changes in the former have significantly smaller temporal and spatial frequencies. However, this approach to distinguish them has only limited applicability for prolonged biomass burning events covering large areas.

Therefore, it might be necessary to look at the negative biomass burning increments in the region of interest in the context of the total emission increment (Figure 66). Here, the region of interest is embedded in a large scale negative background correction mostly originating from the production from VOCs and CH₄. Clearly, there is some degree of aliasing in the optimized emissions from both sources, i.e. part of the local negative biomass burning increments may be explained by an initial overestimation in the a priori of the production of CO from VOCs and CH₄, coupled with the models need to correct for this with a few changes to either source as possible. This will be addressed in a later study that will introduce observations of additional tracers like formaldehyde into the model, for which the long term ambient concentrations should give a harder constrain for the chemical production of CO.

References

Myriokefalitakis, S., Daskalakis, N., Gkouvousis, A., Hilboll, A., van Noije, T., Williams, J. E., Le Sager, P., Huijnen, V., Houweling, S., Bergman, T., Nüß, J. R.,

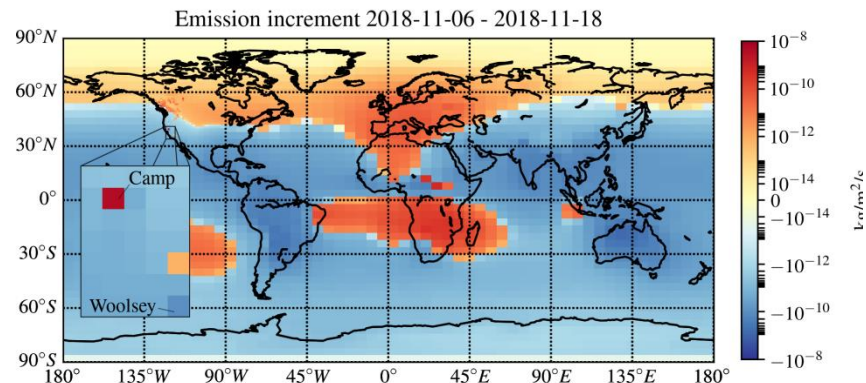


Figure 66: Same as Figure 65, but showing the total CO emission increment ie for biomass burning and production from VOCs and methane combined

Vrekoussis, M., Kanakidou, M., and Krol, M. C.: Description and evaluation of a detailed gas-phase chemistry scheme in the TM5-MP global chemistry transport model. *GMD*, 13, 5507–5548, <https://doi.org/10.5194/gmd-13-5507-2020>, 2020.

Randerson, J.T., et al.: Global Fire Emissions Database, Version 4.1 (GFEDv4). ORNL DAAC, Oak Ridge, TN, USA, <https://doi.org/10.3334/ORNLDAAC/1293>, 2017.

Spivakovsky, C.M., et al.: Three-dimensional climatological distribution of tropospheric OH: Update and evaluation. *Journal of Geophysical Research – Atmospheres*, 105(D7), 8931–8980, 2000.

Release of the Earth System Model Evaluation Tool (ESMValTool) Version 2.0

Veronika Eyring, Bettina K. Gier, and Katja Weigel

Earth System Models (ESMs) are important tools, not only to improve our understanding of present-day climate, but also to project climate change under different plausible future scenarios. For this, ESMs have been continuously improved and extended over the last decades from relatively simple atmosphere-only models to complex state-of-the-art ESMs participating in the latest (sixth) phase of the Coupled Model Intercomparison Project (CMIP, Eyring et al. 2016). This increasing complexity of the models is needed to represent key feedbacks that affect climate change but is also likely to increase the inter-model spread of climate projections within the multi-model ensemble. Innovative and comprehensive model evaluation and analysis approaches are needed to assess the performance of these models, as outlined in a Nature Climate Change paper (Eyring et al. 2019). In response to this need, the Earth System Model Evaluation Tool (ESMValTool) is developed, which makes use of observational data sets and develops and applies new evaluation and analysis techniques for the evaluation of CMIP models.

The ESMValTool is a community diagnostics and performance metrics tool designed to improve comprehensive and routine evaluation of ESMs. It has undergone rapid development since the first release in 2016 and is now a well-tested tool that provides end-to-end provenance tracking to ensure reproducibility of the results. The latest version (v2.0; Righi et al. 2020) of the ESMValTool has been released in 2020. The tool has been developed as a large community effort to specifically target the increased data volume of CMIP6 and the related challenges posed by analysis and evaluation of output from multiple high-resolution and complex ESMs. For this, the core functionalities have been completely rewritten in order to take advantage of

state-of-the-art computational libraries and methods to allow for efficient and user-friendly data processing. Common operations on the input data such as regridding or computation of multi-model statistics are now centralized in a highly optimized preprocessor written in Python. The ESMValTool v2.0, schematically shown in Figure 67, includes an extended set of large-scale diagnostics for quasi-operational and comprehensive evaluation of ESMs, such as diagnostics for atmospheric, oceanic, and terrestrial variables for the mean state, trends, and variability (Eyring et al. 2020). It also includes new diagnostics for extreme events, regional and impact evaluation (Weigel et al. 2020), as well as diagnostics for emergent constraints and analysis of future projections from ESMs in CMIP (Lauer et al. 2020). The tool is currently used to support the upcoming IPCC Working Group I Sixth Assessment

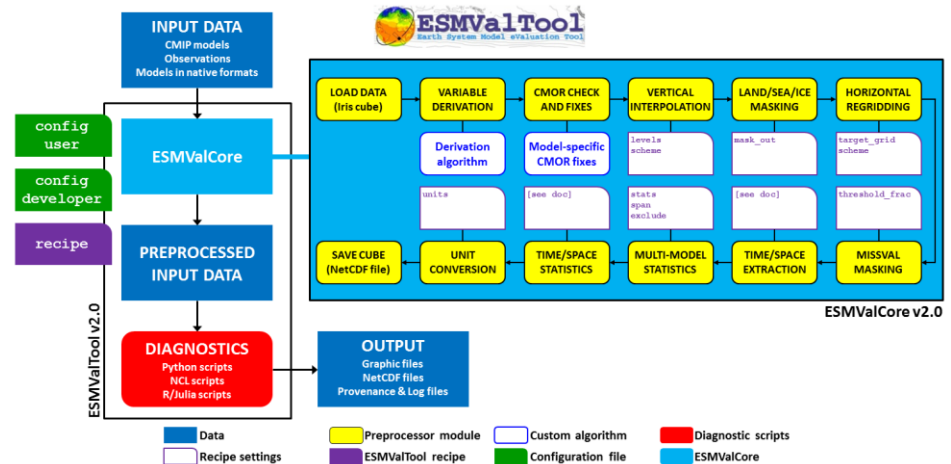


Figure 67: Schematic representation of ESMValTool v2.0 workflow

Report and has been fully integrated into the Earth System Grid Federation (ESGF) infrastructure at the Deutsches Klimarechenzentrum (DKRZ) to provide evaluation results from CMIP6 model simulations shortly after the model output is published to the ESGF. The goal is to continue to support the evaluation and analysis of CMIP and national modelling efforts.

References

Eyring, V., Bony, S., Meehl, G. A., Senior, C. A., Stevens, B., Stouffer, R. J., Taylor, K. E., Overview of the Coupled Model Intercomparison Project Phase 6 (CMIP6) experimental design and organization, *Geosci. Model Dev.*, 9, 1937-1958, doi:10.5194/gmd-9-1937-2016, 2016.

Eyring, V., Bock, L., Lauer, A., Righi, M., Schlund, M., Andela, B., Arnone, E., Bellprat, O., Brötz, B., Caron, L.-P., Carvalhais, N., Cionni, I., Cortesi, N., Crezee, B., Davin, E.L., Davini, P., Debeire, K., de Mora, L., Deser, C., Docquier, D., Earnshaw, P., Ehbrecht, C., Gier, B.K., Gonzalez-Reviriego, N., Goodman, P., Hagemann, S., Hardiman, S., Hassler, B., Hunter, A., Kadow, C., Kindermann, S., Koirala, S., Koldunov, N., Lejeune, Q., Lembo, V., Lovato, T., Lucarini, V., Massonnet, F., Müller, B., Pandde, A., Pérez-Zanón, N., Phillips, A., Predoi, V., Russell, J., Sellar, A., Serva, F., Stacke, T., Swaminathan, R., Torralba, V., Vegas-Regidor, J., von Hardenberg, J., Weigel, K., Zimmermann, K., Earth System Model Evaluation Tool (ESMValTool) v2.0 – an extended set of large-scale diagnostics for quasi-operational and comprehensive evaluation of Earth system models in CMIP. *Geoscientific Model Development*, 13, 3383-3438, 2019.

Eyring, V., Cox, P.M., Flato, G.M., Gleckler, P.J., Abramowitz, G., Caldwell, P., Collins, W.D., Gier, B.K., Hall, A.D., Hoffman, F.M., Hurtt, G.C., Jahn, A., Jones, C.D., Klein, S.A., Krasting, J.P., Kwiatkowski, L., Lorenz, R., Maloney, E., Meehl, G.A., Pendergrass, A.G., Pincus, R., Ruane, A.C., Russell, J.L., Sanderson, B.M.,

Santer, B.D., Sherwood, S.C., Simpson, I.R., Stouffer, R.J., Williamson, M.S., Taking climate model evaluation to the next level. *Nature Climate Change*, 9, 102-110, 2020.

Lauer, A., Eyring, V., Bellprat, O., Bock, L., Gier, B.K., Hunter, A., Lorenz, R., Pérez-Zanón, N., Righi, M., Schlund, M., Senftleben, D., Weigel, K., Zechlau, S., Earth System Model Evaluation Tool (ESMValTool) v2.0 – diagnostics for emergent constraints and future projections from Earth system models in CMIP. *Geoscientific Model Development*, 13, 4205-4228, 2020.

Righi, M., Andela, B., Eyring, V., Lauer, A., Predoi, V., Schlund, M., Vegas-Regidor, J., Bock, L., Brötz, B., de Mora, L., Diblen, F., Dreyer, L., Drost, N., Earnshaw, P., Hassler, B., Koldunov, N., Little, B., Loosveldt Tomas, S., Zimmermann, K., Earth System Model Evaluation Tool (ESMValTool) v2.0 – technical overview. *Geosci. Model Dev.*, 13, 1179-1199, 2020.

Weigel, K., Bock, L., Gier, B.K., Lauer, A., Righi, M., Schlund, M., Adeniyi, K., Andela, B., Arnone, E., Berg, P., Caron, L.-P., Cionni, I., Corti, S., Drost, N., Hunter, A., Lledó, L., Mohr, C.W., Paçal, A., Pérez-Zanón, N., Predoi, V., Sandstad, M., Sillmann, J., Sterl, A., Vegas-Regidor, J., von Hardenberg, J., Eyring, V., Earth System Model Evaluation Tool (ESMValTool) v2.0 – diagnostics for extreme events, regional and impact evaluation and analysis of Earth system models in CMIP. *Geosci. Model Dev. Discuss.*, in review, 2020.

Links

ESMValTool: <http://www.esmvaltool.org/>

Spatially resolved evaluation of Earth system models with satellite column averaged CO₂

Bettina K. Gier, Michael Buchwitz, Veronika Eyring, and Maximilian Reuter

The Intergovernmental Panel on Climate Change (IPCC) Fifth Assessment Report (AR5) confirmed an unequivocal warming of the climate system, with increasing emissions of greenhouse gases as the key drivers of anthropogenic climate change. Therefore, understanding the atmospheric carbon dioxide (CO₂) concentrations, as well as the sources and sinks of carbon is important to improve our ability to predict future CO₂ concentrations and future climate. The carbon content in the atmosphere is rising throughout the years, quantified by the growth rate (GR), with a seasonal cycle due to the absorption of CO₂ by plants for photosynthesis in the summer, and a release of CO₂ through respiration in the winter. Globally this effect is still seen as it is dominated by the larger vegetated areas in the Northern Hemisphere.

Earth System Models (ESMs) participating in the Coupled Model Inter-comparison Project (CMIP) show large uncertainties in simulating atmospheric CO₂ concentrations. Using the Earth System Model Evaluation Tool (ESMValTool), which is developed with contributions of the Climate Modelling Group at IUP, an evaluation of emission driven CMIP simulations from CMIP5 and the newer CMIP6 with satellite data of column-averaged CO₂ mole fractions (XCO₂) from the Greenhouse Gas Group at IUP was performed (Gier et al., 2020). It was found that although the spread remains large in CMIP6 models, the CMIP6 multi-model mean is better able to capture the mean atmospheric content, the growth rate, and the seasonal cycle amplitude (SCA) than the CMIP5 models. Furthermore, as one of the first studies in this field to use satellite data which has a shorter time series than in-situ data, a

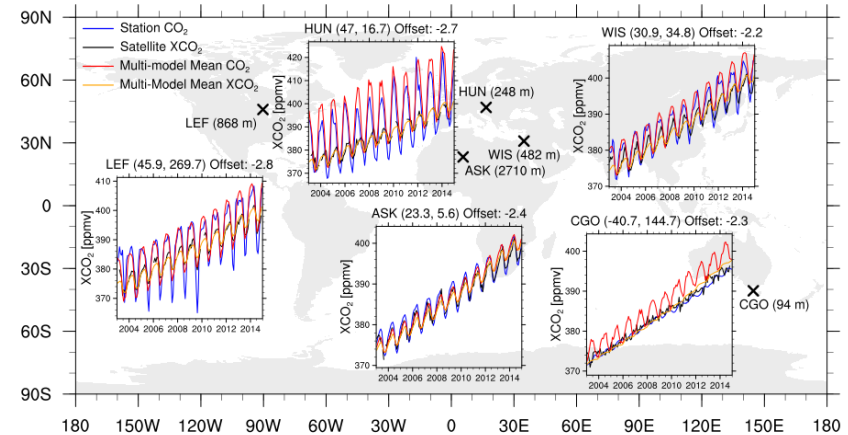


Figure 68: Comparison of time series from satellite XCO₂ (black), CMIP6 multi-model mean XCO₂ (orange) and surface CO₂ (red), and NOAA surface CO₂ station data (blue) at selected sites. The multi-model mean for both XCO₂ and CO₂ was offset to have the same average value as the satellite XCO₂ for better comparison.

comparison between the models ability to reproduce the XCO₂ from satellite data and the surface CO₂ from several in-situ stations in the NOAA/ESRL (National Oceanic and Atmospheric Administration/Earth System Research Laboratory) station network is shown in Figure 68. The multi-model mean is offset so it matches the mean of the XCO₂ satellite data for a better comparison of GR and SCA. The mean and growth rate for both observational datasets is in very good agreement, while the multi-model mean overestimates both. As processes dominating the seasonal cycle originate at the surface, the SCA is higher for the surface CO₂ than the column, which the models are able to reproduce. Another part of this study looked at the influence the observational sampling can have. Figure 69 shows the SCA trend with increasing XCO₂ in the northern mid-latitudes (30-60°N). The top panel shows the unsampled multi-model mean, the middle panel the observations

and the bottom panel the multi-model mean sampled as the observations. The sampling introduces a significant negative trend. This has been attributed to the fact that the satellite dataset in the iteration used in this paper uses two different satellites with overlapping timespans with different spatial sampling. Sampling the models as the first satellite gives a higher mean SCA than sampling the models as the second satellite for the whole time series. This introduces a negative trend when sampling as the combined observational time series.

This study was carried out in close collaboration with the Greenhouse Gas Group at IUP and supported by the Horizon 2020 project Climate-Carbon Interactions in the Current Century (4C) funded by the EU, as well as the Advanced Earth System Model Evaluation for CMIP (EVal4CMIP) project funded by the Helmholtz society.

Reference

Gier, B. K., Buchwitz, M., Reuter, M., Cox, P. M., Friedlingstein, P., and Eyring, V.: Spatially resolved evaluation of Earth system models with satellite column-averaged CO₂, *Biogeosciences*, 17, 6115–6144, <https://doi.org/10.5194/bg-17-6115-2020>, 2020.

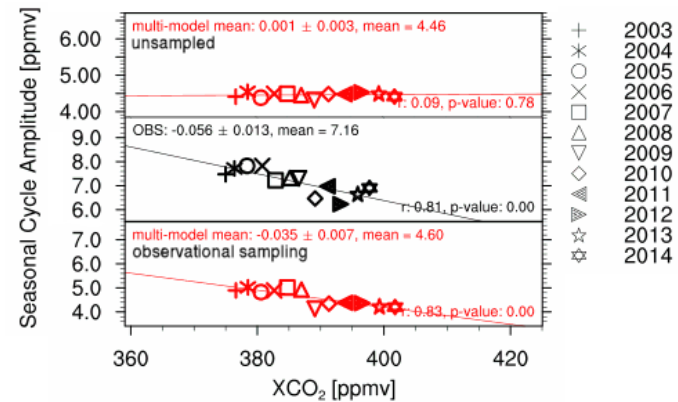


Figure 69: Trend of Seasonal Cycle Amplitude with XCO₂ 2003-2014 for the northern mid-latitudes (30-60°N), including a linear regression. Top panel shows unsampled multi-model mean of CMIP6 emission driven simulations, middle panel satellite observations and lower panel multi-model mean sampled as observations.

Machine learning for process-oriented climate model evaluation

Veronika Eyring, Soufiane Karmouche, and Katja Weigel

Recent advances in machine learning (ML) have enhanced the capacity to reveal causal structures in complex non-linear dynamical systems. Powerful causal discovery methods for climate time series have been developed and some first applications to Earth System Models (ESMs) have now been published with IUP contributions (Nowack et al., 2020). In this work, causal discovery is applied to evaluate models participating in the Coupled Model Intercomparison Project phase 5 (CMIP5). This evaluation is based on the ability of these models to simulate atmospheric dynamical interactions, which are classically measured as lagged correlations between climate variables. Causal discovery algorithms go beyond correlation-based measures by systematically excluding common driver effects and indirect links. Nowack et al., (2020) showed that models with greater skill of representing observed causal fingerprints also better reproduce precipitation in areas like the Indian subcontinent, Africa, East Asia, Europe and North America.

Causal discovery was also used to compare causal links found in reanalysis data with CMIP6 models (Karmouche 2020). Figure 70 shows an example of causal networks derived with a causal discovery algorithm for the NCEP NCAR reanalysis data and a multi-model mean of five CMIP6 models. These causal networks aggregate the information of interdependencies between surface air temperature and surface pressure anomalies over specific remote Pacific Ocean regions (EPAC, CPAC, WPAC). The figure shows the

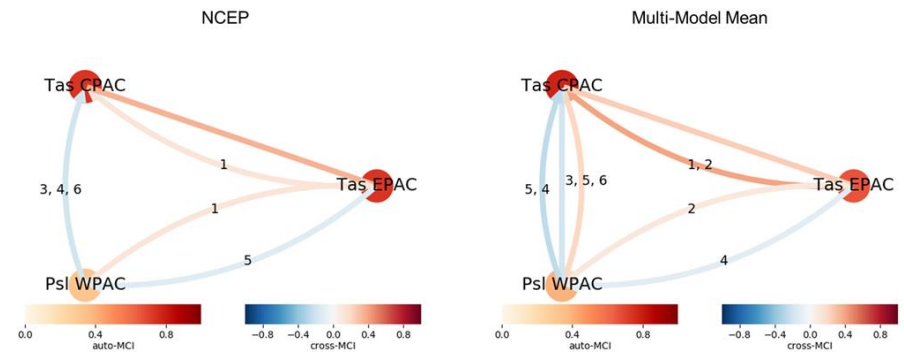


Figure 70: Causal links for the surface air temperature (Tas) and surface pressure (Psl) anomalies over regions in the eastern (EPAC), central (CPAC) and western (WPAC) Pacific for the reanalysis dataset NCEP (left) and the multi-model mean of the five CMIP6 models (right). Node color denotes auto-MCI value, link color cross-MCI value, and link label the time lag (in months) resulting from the causal discovery algorithm. When a link has more than one time-lag label, the link color denotes the link with the highest absolute cross-MCI value; time lags are sorted according to their cross-MCI values. Undirected non-curved links denote contemporaneous connections happening at time lags shorter than 1 month.

ability of CMIP6 models to reproduce the EPAC \rightarrow CPAC \rightarrow WPAC \rightarrow EPAC loop. Interestingly, the models reproduce similar links as the reference reanalysis dataset and closely match the level of autocorrelation (auto-MCI) values and time lags of the links as well as their cross-MCI values.

Additionally, in a changing climate, the frequency, intensity, and the duration of extreme events are expected to change. Major challenges for climate applications need to deal with multivariate, nonlinear, and cause-effect relations occurring on different temporal and spatial scales.

In collaboration with the “Climate Informatics” Group at the DLR Institute of Data Science in Jena, we are working on the exploitation of novel ML methods including causal discovery to tackle the problem of multidimensional and multivariate extreme event identification. ML methods will be further developed to enable an understanding of causal relationships in spatio-temporal multivariate Earth system data with the aim to better project and understand multidecadal climate extremes and their effects.

References

Karmouche, S., Understanding dependency structures in major modes of climate variability with causal discovery, M.Sc. Thesis, University of Bremen, Bremen, Germany, 2020.

Nowack, P., Runge, J., Eyring, V., and Haigh, J. D.: Causal networks for climate model evaluation and constrained projections, *Nat Commun*, 11, ARTN 141510.1038/s41467-020-15195-y, 2020.

Heat and Freshwater Transport by Mesoscale Eddies in the Southern Subpolar North Atlantic

Vasco Müller, Dagmar Kieke, Paul G. Myers, Clark Pennelly, Reiner Steinfeldt, and Ilaria Stendardo

The Mesoscale eddies in the ocean have a typical size of 100 km and a typical lifetime in the order of several days to several months. They cover around 25–30% of the ocean surface at any given moment. Since individual eddies can carry water trapped inside their cores and transport the properties of these waters over long distances, eddies are believed to significantly contribute to the horizontal transport of mass, heat, and salt throughout the ocean.

Sea level anomaly observations obtained from satellite altimetry provide the means of identifying and tracking eddies using automated algorithms. Combining these with sea surface temperature and salinity observations from satellites allows to analyse their surface signatures and to quantify horizontal surface fluxes. However, investigating the vertical structure of eddies and quantifying the respective heat and freshwater transports associated with the eddies are more challenging due to the lack of adequate subsurface observations on mesoscale resolutions.

Temperature (T) and salinity (S) fields for the deeper ocean are typically obtained from ship surveys and profiling Argo floats that are both limited in space and time. In a recent study (Müller et al., 2019) done in collaboration with scientists from the University of Alberta, Edmonton, Canada, we used a new gridded 3-dimensional data set of horizontal and vertical distributions of oceanic T/S fields. These fields were reconstructed from satellite altimetry data for the period

January 1993 to April 2014. This data set, available at daily resolution on a $1/4^\circ$ grid, was combined with sea level anomaly observations from the ocean surface that allowed to identify and track mesoscale eddies in the subpolar North Atlantic between 40°N – 55°N and 43°W – 20.5°W (Figure 71).

The North Atlantic between 40° – 55°N is influenced by two vastly different regimes of currents and water masses: the subpolar gyre, a large-scale cyclonic circulation cell, and the anticyclonic circulation cell of the subtropical gyre. In the Newfoundland Basin, the Western Boundary Current and the North Atlantic Current (NAC), the northward continuation of the Gulf Stream, flow in different directions along the boundary of the two gyres. The Western Boundary Current that originates in the north transports cold and fresh water of subpolar origin towards the tropics. The NAC, on the other hand, carries warmer and saline surface and subsurface waters of subtropical origin into the North Atlantic. It is this exchange of subpolar and subtropical waters that we are interested in.

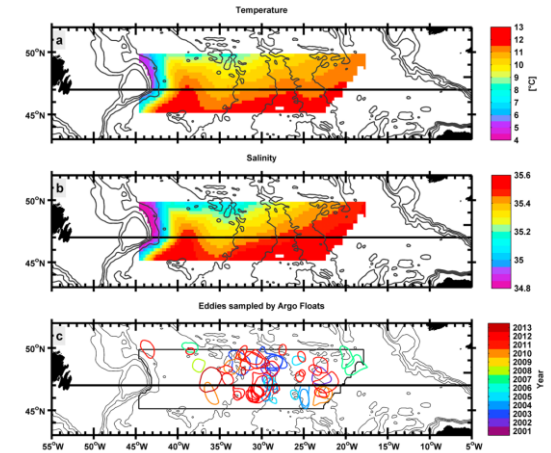


Figure 71: Average upper ocean (surface to 700 m) temperature (a) and salinity (b) in the region of interest shown for the period January 1993 to April 2014. The black line indicates the section at 47°N . Panel (c) shows all eddies that were sampled by individual Argo floats between 2001 and 2013. The limited data coverage as revealed by the Argo floats in (c) demonstrates the need for high-resolution hydrographic data sets as shown in (a) and (b).

We thus identified mesoscale eddies in our region of interest and assigned a vertical temperature and salinity profile to each of the eddies. This way, we were able to quantify the heat and freshwater transports for these eddies as they crossed the latitude of 47°N in northern or southern direction, which marks the approximate boundary between the subtropical and the subpolar regime.

We found that the largest heat and freshwater transports by eddies could be observed in the western part of the Newfoundland Basin. Around 35–45% of the heat and freshwater transports by eddies across 47°N stemmed from individual isolated eddies with large thermohaline signatures. Northward moving cold and fresh cyclonic eddies carrying subpolar water from the Western Boundary Current made a considerable contribution to the overall heat and freshwater transport by eddies crossing 47°N. While the transport by individual eddies was negligible compared to the transport by the mean flow in this region, we found a notable influence on the temporal variability.

We repeated the analysis based on data output obtained from a Canadian ocean model simulation that was based on the Nucleus for European Modelling of the Ocean (NEMO) modelling framework: the Arctic Northern Hemisphere Atlantic configuration with 1/4° horizontal resolution (ANHA4) with a nested 1/12° horizontal resolution encompassing the subpolar North Atlantic, called ANHA4-SPG12. The model simulation covered the period 2002-2013. The results obtained from the observational data sets were well reproduced in the model simulation; in particular, the modelled number of eddies crossing 47°N, the spatial distribution, and the associated heat and freshwater transports across this latitude were consistent with the observations.

Overall, the results from our study helped to provide a better understanding of the contribution of eddies to the transports of heat and freshwater and their variability in a region that is of great relevance for the climate system. The consistency between the observational data set and the model simulation shows that our results are physically meaningful. While there are still limitations regarding the availability of high-quality observations that are well resolved in space and time, model simulations that reasonably well reflect mesoscale dynamics can be used to study thermohaline transports by eddies in regions that may be less well covered by observations.

This study was carried out in the framework of the German-Canadian international research training group ArcTrain, funded by the German Research Foundation (DFG).

References

Müller, V., D. Kieke, P. G. Myers, C. Pennelly, R. Steinfeldt, and I. Stendero, I., Heat and freshwater transport by mesoscale eddies in the southern subpolar North Atlantic, *J. Geophys. Res.*: Oceans, 124, 5565–5585, doi:10.1029/2018JC014697, 2019.

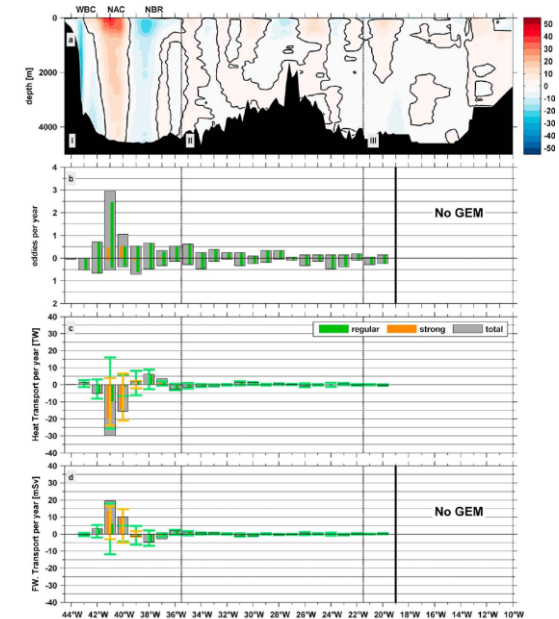


Figure 72: (a) Meridional background velocity obtained from 11 ship surveys conducted nominally along 47°N (from Müller et al., 2017), (b) the number of northward and southward moving eddies from satellite observations (January 1993 to April 2014) per 1° bin crossing 47°N per year, and (c) the sum of the heat and freshwater transports (d) by eddies per 1° bin along 47°N (normalized by the number of years). Vertical bars show the sum of the transports of regular (green) and strong (orange) eddies in either direction. The vertical whiskers represent the standard deviation of the respective transports in either direction. “No GEM” means, the required high-resolution 3D information of temperature and salinity is not available in this region.

Interannual and decadal variability of volume and freshwater transport of the NAC in the subpolar gyre

I. Stendardo, M. Rhein, and R. Steinfeldt

The North Atlantic Current (NAC) supplies the subpolar gyre with warm and saline water from the subtropics as part of the upper branch of the Atlantic Meridional Overturning Circulation (AMOC). Along its northward pathway, the NAC separates into several branches that move eastwards crossing the mid-Atlantic ridge (MAR) and supply the eastern Atlantic with subtropical water from the western basins.

We reconstructed salinity and velocity fields using a transfer function between sea surface height measured by remote sensing and salinity and temperature profiles from Argo floats. The result is a continuous record of salinity and velocity in the upper 1900m on a $1/4^\circ$ Cartesian grid with daily resolution starting in 1993. In general, long-term trends in the data are hidden by the strong interannual variability. As a surprise, the southernmost circulation branches originating near the Mann Eddy occasionally contribute volume and freshwater to the subpolar gyre, and most likely play an important role in the eastern Atlantic salinity distribution (Figure 73). Up to now, these branches were thought to recirculate back to the subtropical gyre and be of no consequence for the subpolar gyre. It turned out that the variability of the NAC-related freshwater transports in the western subpolar North Atlantic is as high, or even higher than the freshwater fluxes from the Arctic Ocean and thus needs to be considered when discussing the impact of freshwater fluxes on the subpolar North Atlantic.

Furthermore, we found that the salinity maximum is usually not found in the NAC but further east in the southward-flowing recirculation. We interpreted this feature being caused by lateral mixing of polar freshwater from the southward flowing western boundary current into the NAC (Figure 75). In this way 0.2 to 0.6 Sv freshwater from the western boundary are reintroduced into the subpolar gyre with the NAC (Figure 74).

Reference

Stendardo, I., Rhein, M., & Steinfeldt, R., The North Atlantic and its volume and freshwater transports in the subpolar North Atlantic, time period 1993-2016. *Journal of Geophysical Research: Oceans*. 125, e2020JC016065, doi:10.1029/2020JC016065, 2020.

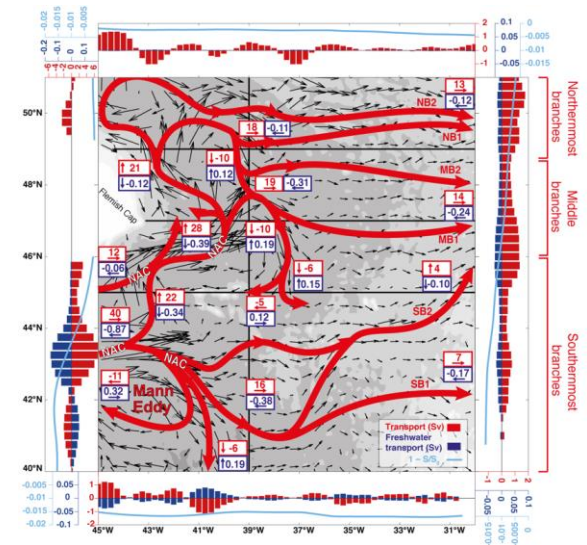


Figure 73: Map of reconstructed mean geostrophic velocities in the upper 700 m averaged over 1993–2015 (black arrows). Red: North Atlantic Current (NAC) branches and recirculation pathways based on these data. Red numbers: mean net northward/eastward (positive) or southward/westward (negative) volume transport for each NAC branch. Blue numbers: corresponding freshwater transports with directions (blue arrows) calculated using a reference salinity $S_0 = 34.80$. At the edges of the map, the zonal/meridional net volume (red bars) and freshwater (blue bars) transports are represented for each latitude/longitude grid point with a bar plot and the term $(1 - S/S_0)$ with a light blue line.

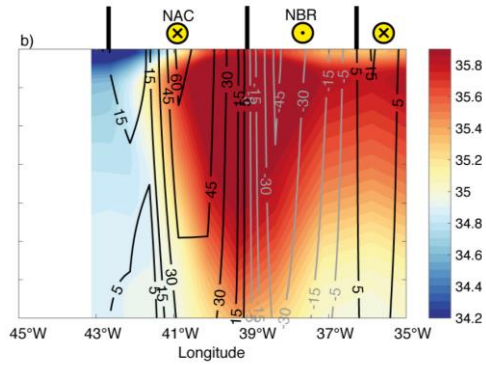


Figure 75: Salinity (contour colour) and velocity (contour lines) at 47°N in 2009 from our reconstructed dataset. Black: northward, grey: southward velocities. The southward flow is named Newfoundland Basin recirculation (NBR). Note that parts of the northward-flowing North Atlantic Current (NAC) are less saline than the recirculation.

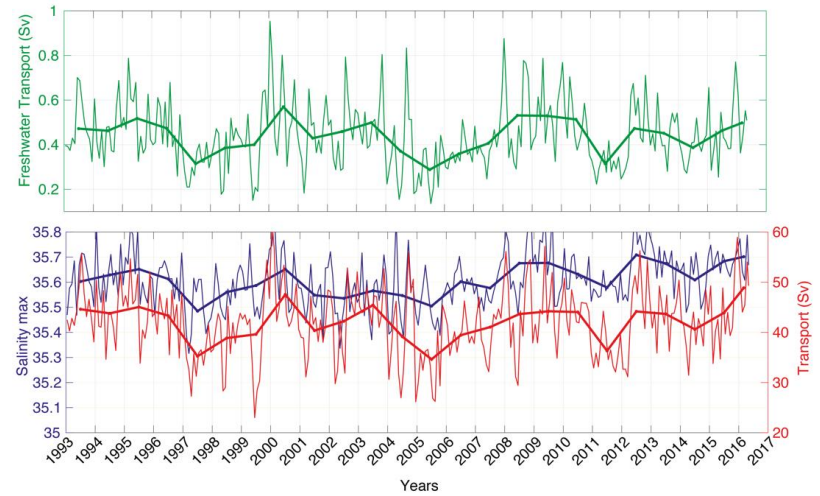


Figure 74: Time series of the NAC freshwater transport (Sv) (green lines, upper panel) at 47°N between 45°W and 37°W. Blue: maximum salinity between 45°W and 37°W in the upper 700 m used as reference salinity to calculate the freshwater transport (green). Red: NAC volume transport (Sv). Thick lines: annual means, thin lines: monthly means.

Wind-driven internal gravity waves

Georg S. Voelker, Dirk Olbers, Christian Mertens, and Maren Walter

Atmospheric cyclones with strong winds significantly impact ocean circulation, regional sea surface temperature, and deep water formation across the global oceans. Thus, they are expected to play a key role in a variety of energy transport mechanisms. Even though wind-generated internal gravity waves are thought to contribute significantly to the energy balance of the deep ocean, their excitation mechanisms are only partly understood. Most of the energy supply by wind is expected to be dissipated in the ocean surface layer and used there for mixing and entrainment.

In an idealized experiment, Voelker et al. (2019) studied the generation of internal gravity waves during a geostrophic adjustment process using an axisymmetric Boussinesq model forced by an idealized pulse of cyclonic wind stress. In this model, internal gravity waves are generated after approximately one inertial period. The outward radial energy flux is dominated by waves having structure close to vertical mode-1 and with frequency close to the inertial frequency. Less energetic higher mode waves are observed to be generated close to the sea floor underneath the storm. The total radiated energy corresponds to approximately 0.02% of the wind input. A deeper mixed-layer or weaker stratification further reduce this fraction. The low energy transfer rates suggest that other processes that drive vertical motion like surface heat fluxes, turbulent motion, mixed region collapse and storm translation are essential for significant energy extraction by internal gravity waves to occur.

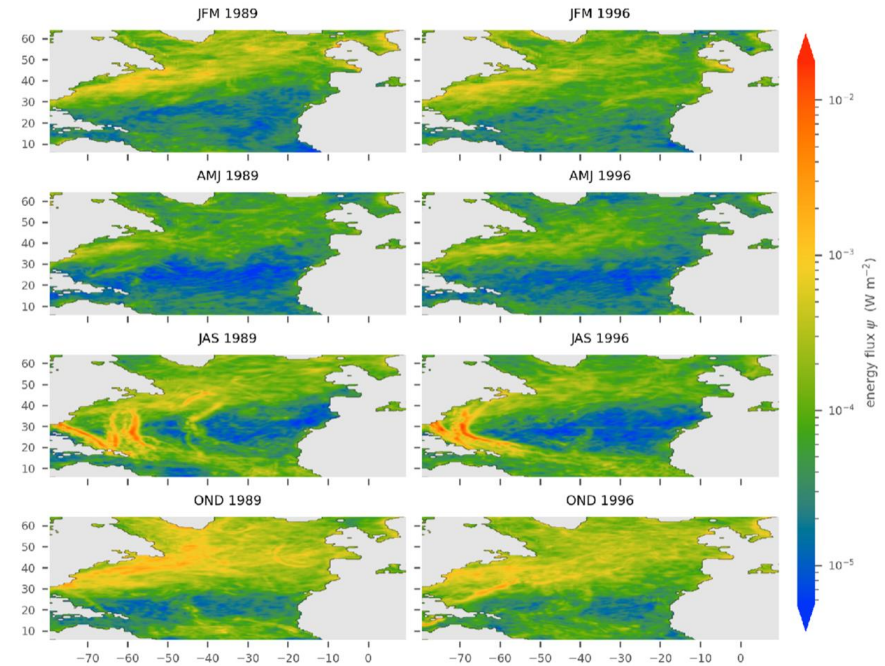


Figure 76: Seasonally averaged energy flux from the mixed layer into the internal wave field for a year with positive (1989, left) and negative (1996, right) NAO index computed with the hybrid extension. Figure from Voelker et al., 2020.

The fraction of the radiated flux to the surface flux of energy is of particular interest to ocean modellers. The radiative energy flux at the mixed layer base determines how much energy can be converted to turbulence in the interior of the ocean and made available for mixing the stratification. An analytical slab model of the mixed layer used before in several studies was extended by consistent physics of wave radiation into the interior. The extended model predicts the energy transfer rates, both in physical and wavenumber-frequency space, associated with the wind forcing, dissipa-

tion in the mixed layer, and wave radiation at the base as function of a few parameters. The results of the model are satisfactorily validated with a realistic numerical model of the North Atlantic Ocean (Olbers et al., 2020). An application of the slab model extension to the North Atlantic using NCEP-CFSR reanalysis wind data (Voelker et al., 2020) shows that the energy transfer into the interior is characterized by a high spatial and temporal variability determined by the wind structure, and dominated by extreme events like storm tracks (Figure 76). The average ratio of radiated energy fluxes from the mixed layer to near-inertial wind power is approximately 12%.

Hydrothermal plume studies using noble gas isotopes

Maren Walter, Florian Schmid, Janna Köhler, Christian Mertens, Maïke Peters, Andreas Türke, and Jürgen Sültenfuß

Helium is one of the gases carried from the Earth's mantle into the ocean by hydrothermal fluids. The absolute concentration of helium is hence much enhanced in the vicinity of hydrothermal vents. Primordial helium is enriched in ^3He compared to atmospheric sources, and the isotopic signature, the $^3\text{He}/^4\text{He}$ ratio, of primordial helium is significantly different from the atmospheric ratio. The concentration and isotopic composition of helium can be identified with high precision in water samples. As an inert noble gas, its concentration in the sea water is only altered by physical processes as mixing, not by biochemical interaction or scavenging. The isotopic signature of the primordial helium is detectable over long distances, which makes helium an ideal tracer to study the dispersal of hydrothermal material.

The oceanic crust is initially cooled and deep-sea chemosynthetic ecosystems are largely fed by hydrothermal circula-

Projects

IRTG ArcTrain (DFG) , TRR 181 Energy Transfer (DFG)

References

Olbers D, Jurgenowski P, Eden C, A wind-driven model of the ocean surface layer with wave radiation. *Ocean Dynamics*, 70, 1067–1088, 2020.

Voelker GS, Olbers D, Walter M, Mertens C, Myers PG, Estimates of wind power and radiative near-inertial internal wave flux —The hybrid slab model and its application to the North Atlantic—. *Ocean Dynamics*, 70, 1357–1376, 2020.

Voelker GS, Myers PG, Walter M, Sutherland BR, Generation of oceanic internal gravity waves by a cyclonic surface stress disturbance. *Dyn. Atmos. Oceans*, 86, 116-133, 2019.

tion and venting on the seafloor. Much of this venting takes place at mid-ocean ridges and in order to both make realistic models of the crust's thermal budget and to understand chemosynthetic biogeography, it is important to have a detailed inventory of vent sites. A major gap in this inventory was the Mid-Atlantic Ridge south of 13°S, a key region for vent fauna biogeography linking the Atlantic to the Indian and Pacific Oceans. During Maria S Merian cruise MSM25 we systematically surveyed the axial region between 13°S and 33°S for hydrothermal signals in the water column (Schmidt et al., 2019). The survey covered more than 2000 km of ridge crest, and we identified previously unknown hydrothermal plumes that indicate 14 new hydrothermal vent fields (Figure 77a). A wide gap in the distribution of vents in

the 19°S-23°S region coincides with the Rio de Janeiro Transform, the maximum southward progression of North Atlantic Deep Waters, and the maximum northwards extent of ^3He -enriched waters with Pacific origins (Figure 77b). Cross-flowing currents in the transform and the large gap between adjacent vents may prevent a meridional connection between the vent fauna communities in the North Atlantic and along the Antarctic Ridges, making this region a prime target for future biogeographical studies.

Compared to mid-ocean-ridge hydrothermal vent fields, those at intra-oceanic island arcs are typically in shallower water depth and have a more variable geochemical fluid composition. Shallow vent sites could influence the photic zone more directly and thus are potentially more relevant for marine primary productivity. The Kermadec arc in the SW Pacific is a very volcanically active part of the Pacific 'Ring of Fire', with more than 80 submarine and subaerial volcanoes. The RV Sonne cruise SO253 was carried out to study the chemically diverse hydrothermal systems hosted by volcanoes with different summit depths and their contribution to the local ecosystem. Helium isotopes in combination with a suite of other tracers as well as current measurements were used to infer the dispersal of the hydrothermal discharge at Brothers volcano, and contributed to one of the first estimates of chemical fluxes from arc systems (Neuholz et al., 2020a,b).

Projects

Hydrothermadec (BMBF), RidgeMix (DFG)

References

Neuholz R, Schnetger B, Kleint C, Koschinsky A, Lettmann K, Sander S, Türke A, Walter M, Zitoun R, Brumsack H-J, Near-field hydrothermal plume dynamics at Brothers Volcano (Kermadec Arc): A short-lived radium isotope study. *Chem. Geol.*, 533, 119379, 2020a.

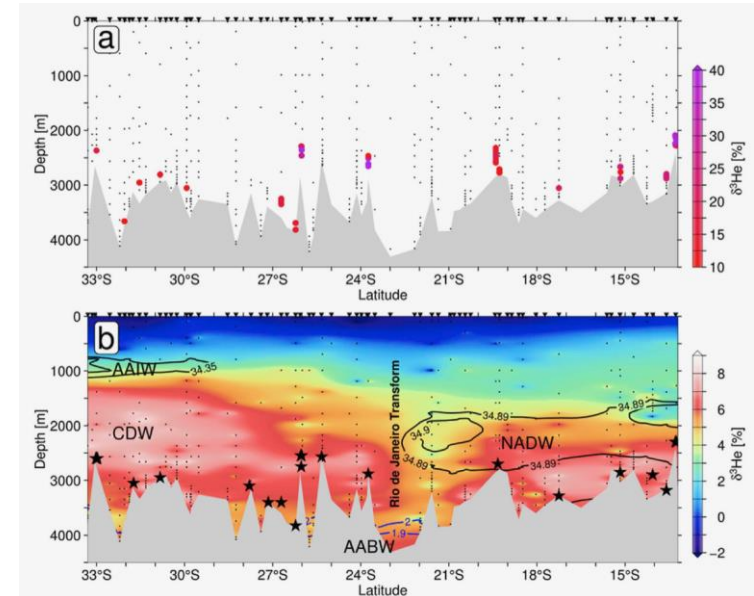


Figure 77: Two aspects of the ^3He distribution above the SMAR. (a) Hydrothermally sourced anomalies with $\delta^3\text{He} > 10\%$. Samples with $\delta^3\text{He} < 10\%$ are shown in black. (b) Gridded meridional section $\delta^3\text{He}$ background (samples with $\delta^3\text{He} > 9\%$ omitted from gridding). Contour lines delineate salinities/temperatures indicative of water mass cores: North Atlantic Deep Water (NADW), Antarctic Bottom Waters (AABW), and Antarctic Intermediate Water (AAIW); CDW denotes Circumpolar Deep Waters carrying excess $\delta^3\text{He}$ from the Pacific. Black stars indicate locations of identified hydrothermal vent sites. Figure from Schmid et al., 2019.

Neuholz R, Kleint C, Schnetger B, Koschinsky A, Laan P, Middag R, Sander S, Thal J, Türke A, Walter M, Zitoun R, Brumsack H-J, Submarine hydrothermal discharge and fluxes of dissolved Fe and Mn, and He isotopes at Brothers Volcano based on radium isotopes. *Minerals*, 10, 969, 2020b.

Schmid F, Peters M, Walter M, Devey C, Petersen S, Yeo I, Köhler J, Jamieson JW, Walker S, Sültenfuß J, Physico-chemical properties of newly discovered hydrothermal plumes above the Southern Mid-Atlantic Ridge (13°-33°S). *Deep Sea Res. I*, 148, 34-52, 2019.

Sensitivity of Labrador Sea Water Formation to Changes in Model Resolution, Atmospheric Forcing, and Freshwater Input

Yarisbel Garcia-Quintana, Peggy Courtois, Xianmin Hu, Clark Pennelly, Dagmar Kieke, and Paul G. Myers

The subpolar North Atlantic is a vital area for heat and freshwater exchange between the low and high latitudes. Within the subpolar North Atlantic, the Labrador Sea, located between the Labrador coast of Canada and Greenland, exerts a significant influence on the climate system. Strong winter cooling of the ocean surface causes the surface waters to lose heat to the atmosphere and to enable a process called deep convection. The Labrador Sea is one of the few regions in the world ocean where winter-time deep convection is known to occur. As a consequence the surface water becomes denser, the mixed layer starts to deepen, and the water sinks to depths between 500 and 2500 m. This sinking brings dissolved gases like oxygen and carbon dioxide into the deep ocean. The resulting water mass is known as Labrador Sea Water (LSW). Once formed, LSW spreads out from its formation region loaded with high concentrations of dissolved oxygen and anthropogenic tracers and can be tracked throughout the entire North Atlantic and beyond.

The process through which LSW is formed is sensitive to freshwater inflow into the formation region and storms passing over the Labrador Sea. While an increase in freshwater would inhibit the densification and sinking of surface water, fewer storms would reduce heat loss also reducing

the ability of the surface waters to gain in density and sink to greater depths. These are all changes projected to occur due to the ongoing anthropogenic climate change.

By using a numerical model, we investigated in our recent study (Garcia-Quintana et al., 2019) how changes in the spatial model resolution, the increase in freshwater discharge from Greenland, changes in the precipitation, and the absence of storms could impact LSW formation. This study was done in collaboration with scientists from the University of Alberta, Edmonton, Canada.

In order to explore the sensitivity of the LSW formation rate on changing conditions, a control simulation and four perturbation experiments were carried out using a Canadian state-of-the-art coupled ocean-sea ice model. The model simulation was based on the Nucleus for European Modelling of the Ocean (NEMO)

modelling framework, in particular the Arctic Northern Hemisphere Atlantic configuration with 1/4° horizontal resolution (ANHA4). Each of the perturbation experiments had a specific alteration compared to the control simulation (Figure 78). LSW formation rates were determined using a

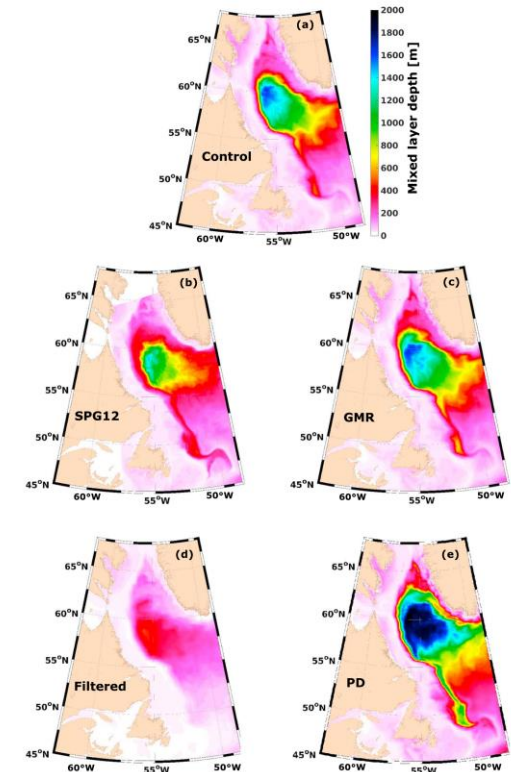


Figure 78: March mixed layer depths in the Labrador Sea, averaged over the years 2004 to 2016, for the control model simulation (a) and four perturbation runs (b-e). SPG12: increased spatial resolution of the model, GMR: Greenland meltwater discharge removed, Filtered: storms removed, PD: precipitation decreased.

kinematic subduction approach. The study considered the period from January 2004 to December 2016.

We found that by having more freshwater going into the formation region the overall LSW formation rate did not decrease, however, the water mass became lighter. Thus, the presence of Greenland meltwater affected mainly the formation of a denser type of LSW. In the absence of the storms, i.e., when removing all storms in the perturbation run, a decrease of 44% in heat loss over the Labrador Sea was noted, strong enough to halt the deep convection and decrease the LSW formation rate by 89%. Even if this exper-

Decay of internal tides

Janna Köhler, Jonas Löb, Maren Walter, Christian Mertens, Dirk Olbers, and Monika Rhein

Low-mode internal waves in the ocean possess a simple vertical structure, and hold a large part of the total energy of the internal wave field. They are able to travel basin-wide before they are dissipated (for a review, see Mertens et al. 2019). The spatial distribution of mixing related to internal wave dissipation affects the global overturning circulation in numerical models, but the observation as well as the representation of internal waves in ocean general circulation models (OGCMs) is still challenging. OGCMs do not resolve the spatial scales of the energy dissipation of internal waves and the resulting mixing. In order to account for mixing in the interior of the ocean, parameterizations have to be used. The module IDEMIX (Internal wave Dissipation Energy and Mixing) is a parameterization that describes the generation, propagation, interaction, and dissipation of the internal gravity wave field developed for the use in OGCMs (Olbers et al., 2019). IDEMIX is central to the concept of energetically consistent ocean models, since it links all sources and sinks of internal wave energy, as well as param-

eterized forms of energy, in a model without spurious sources and sinks.

We studied the radiated low mode internal waves including processes operating along their paths to improve our understanding of the life cycle of internal waves. To identify sources and sinks, as well as to quantify the contribution to local dissipation, in-situ hydrographic measurements were combined with observations of internal wave energy fluxes based on satellite altimetry and STORMTIDE. STORMTIDE is a 1/10°-simulation from the Max-Planck Institute Ocean Model (MPIOM) forced by the full lunisolar tidal potential that resolves low-mode internal waves. A realistic surface forcing with 6-hourly wind stress was included in STORMTIDE2, currently the only global OGCM that is driven by tidal and wind forcing. The region of in-situ observations was south of the Azores in the NE Atlantic, where the satellite altimetry and STORMTIDE show beams of converging low mode internal waves generated at a seamount chain.

Reference

Garcia-Quintana, Y., P. Courtois, X. Hu, C. Pennelly, D. Kieke, and P. G. Myers, Sensitivity of Labrador Sea Water formation to changes in model resolution, atmospheric forcing, and freshwater input, *J. Geophys. Res.: Oceans*, 124. doi:10.1029/2018JC014459, 2019.

The modal structure of the internal tide energy flux is important for the ratio of local (close to the generation site) to remote energy dissipation, as low-mode internal waves are less prone to breaking and more likely to propagate over large distances compared to waves with a complex vertical structure. Our in-situ observations show that even close to the generation site, the energy flux is primarily contained in the first mode and thus likely to propagate over long distances before dissipating (Köhler et al. 2019). Superposition of modes 1 and 2 captures over 84% of the total energy flux, indicating that OGCMs that resolve the first two modes are potentially able to capture the main characteristics of internal tide energy fluxes related to topography on scales typical for seamounts.

The direct comparison of the energy fluxes from the in-situ measurements, satellite altimetry, and OGCM shows that in-situ fluxes are generally higher than the corresponding fluxes in STORMTIDE and those derived from altimetry (Figure 79). Differences between in-situ data and altimetry are expected since the spatial resolution of satellite data limits the resolution of the inferred energy fluxes. The long-range propagation of the internal tides observed in altimetry generally agrees with the results from the in-situ measurements, although the in-situ energy fluxes are more variable and show a less monotonic decrease away from the generation sites. STORMTIDE resolves small scale structures in the energy flux distribution, but high energy fluxes are restricted to the vicinity of the generation sites.

While the study region was chosen because of the unimpaird spreading of internal tides after generation, a mooring time series reveals the presence of eddies during two time periods (Figure 80, Löb et al. 2020): one surface intensified eddy with a maximum horizontal velocity of approx. 20 cm s⁻¹, and a weaker subsurface one. The temporal variability

in the time series of energy flux is dominated by two factors: A strong coupling of the flux magnitude to the spring-neap variability in the barotropic tidal forcing (Figure 80), and the decrease of energy flux during phases of higher eddy kinetic energy. Especially the surface-intensified eddy is correlated with a significant weakening of the energy flux compared to the time period with no eddy activity (Figure 80). A potential transfer of the “missing” internal tide energy in modes 1 and 2 into higher mode internal waves would result in a changed ratio of local to remote energy dissipation and hence be important for the global distribution of internal wave energy.

A theoretical study on the energy transfer from the M2 internal tide to the ambient wave field via nonlinear triad interactions (Olbers et al. 2020) infers a globally integrated energy transfer of less than 0.1 TW for the STORMTIDE simulation, and up to 0.3 TW for a more energetic scenario. This compares reasonably well to 0.5 to 1 TW of global barotropic to baroclinic tidal conversion, but also suggests that other mechanisms such as local dissipation and tide-eddy interaction are important contributors to the global internal M2-tide energy sink. Whether the decrease in the low-mode

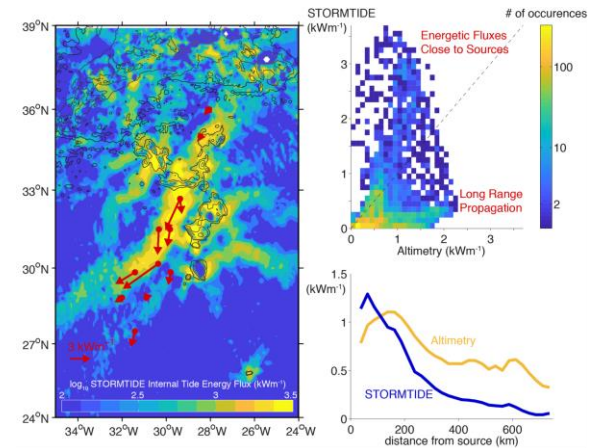


Figure 79: (left) M2 internal tide energy flux from in-situ observations (red arrows) and STORMTIDE (background); (right) comparison of internal tide energy fluxes in STORMTIDE and from satellite altimetry: STORMTIDE shows high values close to the generation sites, while in the altimetry higher fluxes persist over longer distances.

internal tide energy flux observed in the mooring time series is due to increased dissipation, refraction or scattering of energy into higher modes is the subject of a planned future study.

This research was conducted in the framework of the Collaborative Research Centre TRR 181 “Energy Transfer in Atmosphere and Ocean” funded by the Deutsche Forschungsgemeinschaft (DFG, German Research Foundation)—Projektnummer 274762653

References

Löb, J., Köhler, J., Mertens, C., Walter, M., Li, Z., von Storch, J.-S., Zhao, Z., Rhein, M., Observations of the low-mode internal tide and its interaction with mesoscale flow south of the Azores. *J. Geophys. Res. Oceans*, 125(11), e2019JC015879, 2020.

Olbers, D., F. Pollmann, C. Eden, On PSI Interactions in Internal Gravity Wave Fields and the Decay of Baroclinic Tides. *J. Phys. Oceanogr.*, 50, 751–771, 2020.

Köhler, J., Walter, M., Mertens, C., Stiehler, J., Li, Z., Zhao, Z., von Storch, J.-S., and Rhein, M., Energy Flux Observations in an Internal Tide Beam in the Eastern North Atlantic. *J. Geophys. Res. Oceans*, 124(8), 5747-5764, 2019.

Olbers, D., Eden, C., Becker, E., Pollmann, F., Jungclaus, J., The IDEMIX Model: Parameterization of Internal Gravity Waves for Circulation Models of Ocean and Atmosphere. In *Energy Transfers in Atmosphere and Ocean (87- 125)*, Carsten Eden and Armin Iske, Eds., Springer, 2019.

Mertens, C., Köhler, J., Walter, M., von Storch, J.-S., Rhein, M., Observation and models of low mode internal waves in the ocean. In *Energy Transfers in Atmosphere and Ocean (127- 143)*, Carsten Eden and Armin Iske, Eds., Springer, 2019.

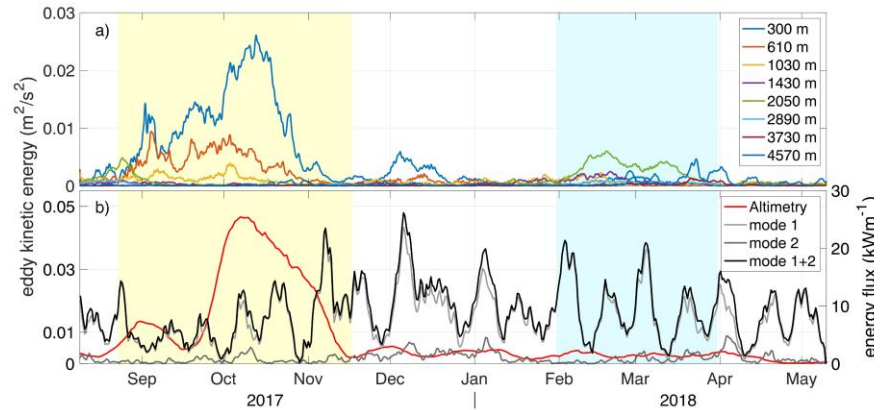


Figure 80: (a) Eddy kinetic energy (EKE) at the mooring location (30.48°N, 30.12°W) from the moored current meters and from CMEMS satellite data (red line in b). (b) Modal decomposition of observed energy flux of the semidiurnal internal tide. Different background colours indicate eddy activity: yellow = surface eddy; blue = subsurface eddy; white = no eddy. From Löb et al. 2020.

Observed transport decline at 47°N in the western North Atlantic

Monika Rhein, Christian Mertens, and Achim Roessler

The flow of warm and saline subtropical water toward the northern North Atlantic, a major component that makes northwestern Europe the warmest place in at these latitudes in winter, is part of the Atlantic meridional overturning circulation (AMOC). Climate models project an AMOC decline between 10% and 50% till 2100 with severe impacts on climate and sea level. Whether the AMOC has already weakened in response to anthropogenic climate change is an open question that motivates multiple sustained observation systems of the AMOC (Rhein 2019; McCarthy et al., 2020; Frajka-Williams et al., 2019).

Despite the importance of the large-scale circulation in the North Atlantic for the climate system and the sea level, most of the interior flow field is only known qualitatively, and neither the mean nor the variability and trends are quantified. In a long-term study, we investigated the current field in the western North Atlantic at 47°N between 44°W and 31°W using a combination of inverted echo sounders deployed at the seafloor and moored current meters (Rhein et al., 2019).

The North Atlantic Current (NAC) is only about 100–150 km wide but imports 106 Sv ($1 \text{ Sv} = 10^6 \text{ m}^3/\text{s}$) into the Newfoundland basin (Figure 81), making the NAC one of the strongest currents in the world ocean. Constrained by the bathymetry, more than half of the northward flow recirculates to the south in close proximity to the NAC (-59 Sv). The

mean transport of the southward boundary current at the continental margin is -23 Sv. The NAC and its return flow are significantly anti-correlated: A stronger NAC inflow corresponds to a stronger recirculation. The mean flow east of 37°W is -28 Sv to the south but much more sluggish than in the west and without permanent local features. This part of the circulation seems to be independent from the NAC system and the boundary current, since no significant correlation with these individual time series was found. The sum of the interior AMOC components results in a northward transport of 19 Sv. Combined with the southward boundary current the mean top-to-bottom transport across the measurement array is -4 Sv.

The temporal variability of the water transports across 47°N that was derived from the shipboard and the moored observations turned out to be highly correlated with sea surface height measurements from satellite altimetry, a result that was then used to calculate a longer time series of transport fluctuations directly from the altimeter measure-

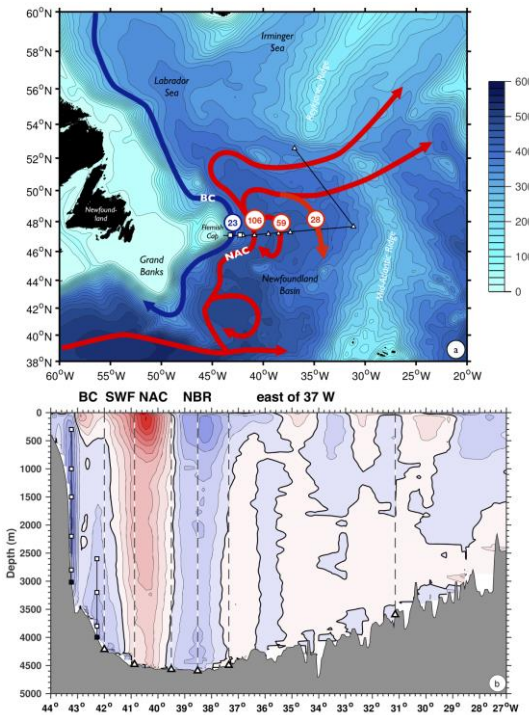


Figure 81: (a) Schematic circulation of the boundary current (blue) and the NAC system (red). Included are the locations of moored instruments and mean volume transports (in $10^6 \text{ m}^3/\text{s}$). (b) Mean meridional velocities at 47°N, based on 12 repeat lowered acoustic Doppler current profiler sections (red: northward, blue: southward velocities, contour lines are every 5 cm/s). The locations of the moorings (black squares) and pressure inverted echo sounders (triangles) are indicated, the current meters in the moorings are shown as white squares. The flow components are: BC = boundary current; SWF = southward flow; NAC = North Atlantic Current; NBR = Newfoundland Basin recirculation; east of 37°W = flow between 37°W and 31°W.

ments (Figure 82). The analysis reveals significant decadal trends (despite the large variability on all time scales), but these trends are found in the interior transport contribution and not in the Gulf Stream/NAC transport as might have been expected. The southward flow east of 37°W increased significantly by -0.44 Sv/year and is the main contributor to the declining interior northward flow of -0.60 Sv/year (Figure 82). Over the period of the analysis, the total transport in the interior decreased by about 10 Sv. The trends of the other individual components are not significant, but the sum of the interior and boundary current transport is -0.71 Sv/year.

The derived transport trends are linked to irregular decadal trends in sea surface height and thus most likely caused by regionally different warming of the water column. The decadal sea surface height trends (1993–2018) in the subpolar North Atlantic are generally positive and, at 47°N, strongest at the western boundary. In the interior, the trends are not significant at many locations, and patches of negative and positive trends are in close proximity along the perceived pathways of the NAC. Combined with the western boundary positive trend, this leads to a weakening horizontal pressure gradient and thus to decreasing interior northward transports from the subtropical to the subpolar western Atlantic.

References

McCarthy, G.D., P.J. Brown, C.N. Flagg, G. Goni, L. Houpert, C.W. Hughes, R. Hummels, M. Inall, K. Jochumsen, K.M.H. Larsen, P. Lherminier, C.S. Meinen, B.I. Moat, D. Rayner, M. Rhein, A. Roessler, C. Schmid, and D.A. Smeed, Sustainable observations of the AMOC: Methodology and Technology. *Reviews of Geophysics*, 58, e2019RG000654, doi:10.1029/2019RG000654, 2020.

Frajka-Williams, E., I.J. Ansorge, J. Baehr, H.L. Bryden, M. Paz Chidichimo, S.A. Cunningham, G. Danabasoglu, S. Dong, K.A. Donohue, S. Elipot, N.P. Holliday, R. Hummels, L.C. Jackson, J.

Karstensen, M. Lankhorst, I. Le Bras, S. Lozier, E.L. McDonough, C.S. Meinen, H. Mercier, B.I. Moat, R.C. Perez, C.G. Piecuch, M. Rhein, M. Skrokoz, K.E. Trenberth, S. Bacon, G. Forget, G. Goni, P. Heimbach, D. Kieke, J. Koelling, T. Lamont, G. McCarthy, C. Mertens, U. Send, D.A. Smeed, M. van den Berg, D. Volkov, and C. Wilson. Atlantic Meridional Overturning Circulation: Observed transports and variability. *Frontiers in Marine Science*, 6:260, doi:10.3389/fmars.2019.00260, 2019.

Rhein, M., Taking a close look at ocean circulation. *Science*, 363, 456-457, doi:10.1126/science.aaw3111, 2019.

Rhein, M., Mertens, C., and A. Roessler, Observed transport decline at 47°N, western Atlantic. *Journal of Geophysical Research: Oceans*, 124, doi:10.1029/2019JC014993, 2019.

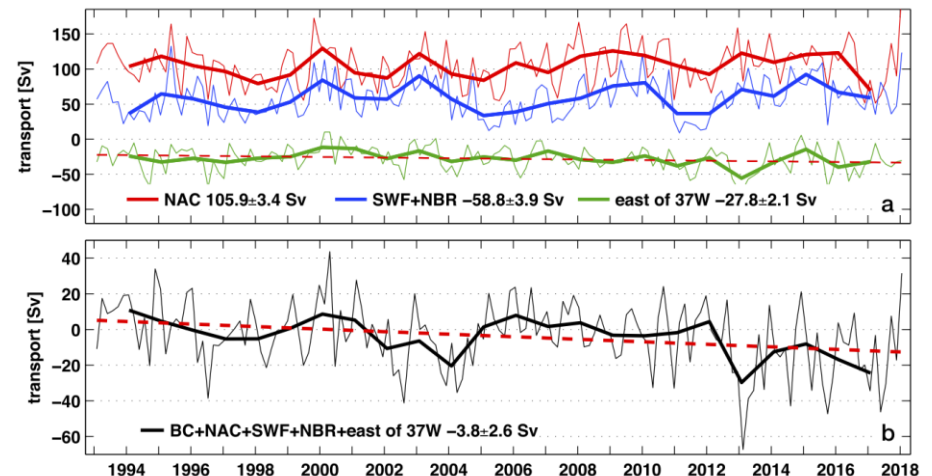


Figure 82: Time series of bimonthly (thin) and annual (bold) top-to-bottom mean transport (Sv) at 47°N. Long-term linear trends are indicated where statistically significant (dashed). (a) NAC (red), return flow (blue), and transport east of 37°W (green). The return flow is inverted to emphasize the high anti-correlation. (b) Sum of all transport contributions. Numbers are the mean transports and the standard error of the mean. NAC = North Atlantic Current; SWF = Southward Flow; NBR = Newfoundland Basin recirculation; BC = boundary current.

The Terrestrial Environmental Physics Group at University of Bremen

Helmut Fischer

The Terrestrial Environmental Physics Group became a member of IUP in the year 2000. It has always operated jointly with the Bremen State Laboratory for Radioactivity Measurements, taking advantage of the available high-sensitive radiometric instrumentation and sharing a large part of the personnel. However, since several years already, the State Laboratory has suffered from severe reduction of staff, obliging the group to abandon most research projects, and teaching as well. Still, some research highlights can be mentioned based on international cooperation, which had started in previous years (projects “Blue carbon studies in

Blue carbon studies in Indonesia

Helmut Fischer and Dana Ransby

Coastal mangrove forests are recognized as an important storage for organic carbon, nowadays often denominated „blue carbon“. C inventories in mangrove ecosystems have frequently been determined experimentally, and are an indicator of the potential C release in case of degradation. Much less is known about the carbon accretion rate (CAR), the key indicator for the effectiveness of C sequestration. Due to the short time scale, the common ^{14}C (half-life 1600 years) age method cannot be applied to determine the age of sediment layers.

Indonesia” and “Origin of atmospheric Ru-106 over Europe”, see below). Furthermore, one third-party funded project is still on the way and active, and it also produced exciting results (“Modelling the partitioning of radionuclides in agricultural soils”). This project goes “back to the roots” of the group, as it has the same topic as its predecessor at the Physics Department. This project group already became active shortly after the foundation of Bremen University in 1971 and worked on the security and safety of nuclear power and the safe storage of its residues (Figure 83).

The radiometric laboratory at IUP took part in a project lead by the Leibniz Centre for Tropical and Marine Research Bremen (ZMT), contributing short time dating for three coastal mangrove forest sediment cores from Indonesia (Kusumaningtyas et al. 2019). The cores were taken from a degraded mangrove forest under riverine influence, a less degraded forest in a tidally influenced lagoon, and a non-degraded tidal coast forest. The dating was based on atmospheric deposition of the natural radioisotope Pb-210 (half-life 22.3 years), with additional information obtained from man-



Figure 83: title page of a book on nuclear waste, published in 1977 by a group of (mainly) physics students at Bremen University, the author among them.

made Cs-137 (half-life 30 years), both detectable by gamma spectroscopy.

High sedimentation rates, typical for mangrove forests, meant high dilution of deposited tracers. Therefore, the experimental conditions were demanding, requiring measurement times of up to one week per sample.

The encountered CAR values were extremely high (Figure 84), proving the importance of mangrove ecosystems as blue carbon sinks. The second finding is that CAR and C inventory are not necessarily correlated. Therefore, one cannot be inferred from the other. Dating of mangrove ecosystem sediments by Pb-210 methods is experimentally demanding, but can provide this valuable information.

Reference

M.A. Kusumaningtyas, A. A. Hutahaeen, H. W. Fischer, M. Pérez-Mayo, D. Ransby, T. C. Jennerjahn: Variability in the organic carbon stocks, sources, and accumulation rates of Indonesian mangrove ecosystems. *Estuarine, Coastal and Shelf Science*, 218, 310-323 <https://doi.org/10.1016/j.ecss.2018.12.007>, 2019.

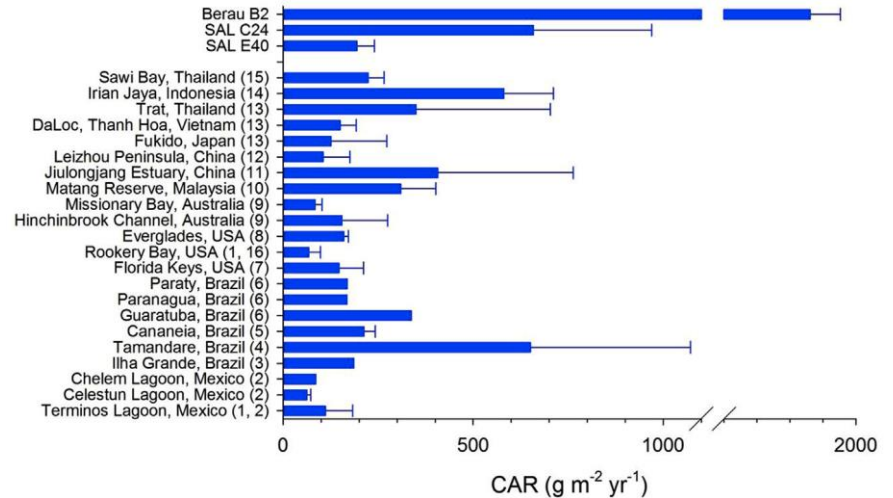


Figure 84: Measured carbon accretion rates in the present study (top), compared to literature values (bottom) (Kusumaningtyas et al. 2019)

Origin of atmospheric Ru-106 over Europe

Helmut Fischer and Dana Ransby

The radioisotope Ru-106 is an important fission product in nuclear power plant operation. Therefore, its appearance and concentration in the ground level atmosphere is monitored worldwide by national laboratories. Its presence can additionally be detected by an international network of monitoring stations serving the Comprehensive Test Ban

Treaty Organization (CTBTO). About 50 state laboratories, located mainly in Europe, maintain an informal network called „Ring of Five“ (from its original number of members), exchanging information by mail. IUP became a member in 2014 due to the group’s work on atmospheric releases of medically used radioactive iodine I-131.

In fall 2017, many Ro5 member laboratories almost simultaneously detected atmospheric Ru-106 (Figure 85). Luckily, the values were all below values requiring protective actions for the population. Ru-106 concentration values increased from west to east, and the then prevailing easterly winds pointed towards a release somewhere in eastern Europe. However, no state declared knowledge about, or responsibility for, a release of Ru-106. As no other typical fission products were found together with the ruthenium, a nuclear fission event could be ruled out, leaving an accidental release of this single isotope, used in medicine and possibly for radiothermal generators, as possible source.

Apart from reporting the data to their national emergency institutions, Ro5 members started retrieving more data, including terrestrial deposits collected also in Bremen and the Czech Republic by IUP members. Ru-106, which the lab's detectors had last encountered in 1986 in Chernobyl fallout, could be detected in several grass samples – grass is a good collector for airborne isotopes attached to aerosols.

Under guidance of IRSN (France) and IRS Hannover, all Ru-106 data from Ro5 member labs and from CTBTO were further analysed and compared to backward trajectories from atmospheric transport models. The results indicate a release point near the southern Ural region in Russia. The Mayak industrial complex, housing a large radioisotope factory, is located there, and this factory had signed a contract for production of a very strong Ce-144 radioisotope source needed for a high-energy physics experiment on neutrino oscillations to be performed at the Gran Sasso Laboratory in Italy. Ce-144 is commonly produced from spent reactor fuel, inevitably also containing Ru-106. The Mayak factory withdrew from the contract shortly after the Ru-106 detections without giving reasons. However, the factory as well as the Russian state deny knowledge about a release of Ru-106.

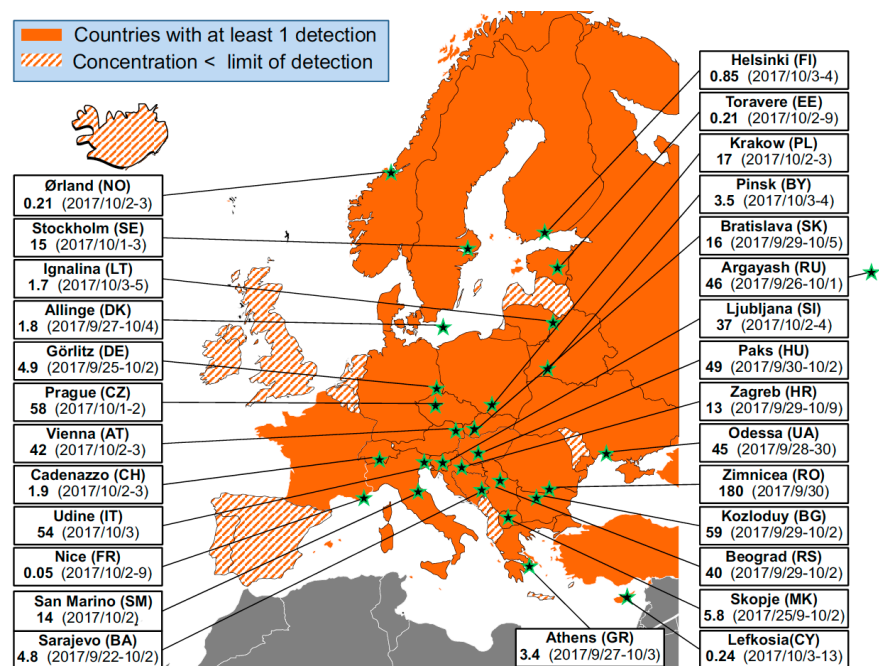


Figure 85: Measurement locations and observed Ru-106 atmospheric concentration in Europe (Masson et al. 2019)

Given this situation, the paper and its conclusions became highly relevant. The publication in PNAS (Masson et al. 2019) was chosen for the journal's title page and caused enormous media interest.

Reference

O. Masson, G. Steinhauser et al.: Airborne concentrations and chemical considerations of radioactive ruthenium from an undeclared major nuclear release in 2017. Proc. Natl. Acad. Sci. USA 116, 16750–16759, <https://doi.org/10.1073/pnas.1907571116>, 2019.

Modelling the partitioning of radionuclides in agricultural soils

Volker Hormann

Contamination of the environment by radionuclides may occur in the course of nuclear accidents as in Chernobyl or Fukushima where the main route is deposition onto plants and into the soil, being transported by rain or irrigation water. Another scenario is the leakage of long-lived radionuclides from a nuclear waste repository (NWR) and their subsequent migration into groundwater and surface soil. The soil can serve as a large reservoir for these nuclides, depending on their chemical properties and the chemical composition of the soil in question. Often a large proportion of the contaminant will be adsorbed to the surface of soil particles, but a certain amount will be present in the liquid phase ("soil solution"). This partitioning is described by the so-called distribution coefficient or K_d (in L/kg) which is defined as the ratio of the activity sorbed to the soil solids (in Bq/kg) to the activity in soil solution (in Bq/L). Plant roots generally do not distinguish between contaminants and nutrients and thus, radionuclides may be taken up from the liquid phase and incorporated into various parts of the plant, depending on the chemical nature of the contaminant. If the plant is edible, the radioactive contaminants enter the food chain and are finally ingested by humans.

Radioecological models like ECOLEGO for the assessment of radiation risks arising from these contaminations usually require information on the K_d of radionuclides in agricultural soils. In most cases, tabulated values are used. As these values have large uncertainties, geochemical models are an attractive alternative, because they can calculate the K_d dependence on the relevant measurable soil parameters.

In the framework of the joint project Trans-LARA* (funded by the BMBF), which is designed to broaden the understanding of radionuclide transport from groundwater to plants, a model has been developed that is simultaneously valid for the long-lived radionuclides americium, plutonium and selenium. These are all relevant in the nuclear waste repository context while their chemistries are considerably different. Using a simplified picture of soil composition (Hormann 2015) and thermodynamic data from the literature for the most relevant soil components, a component additive model for the estimation of radionuclide partitioning and speciation in agricultural soils has been further developed and validated. With the help of this model (called UNiSeCs II), distribution coefficients for Am, Pu and Se can be estimated reasonably well, thus reducing the uncertainty that arises from the use of tabulated values. For these elements, the most important soil parameters have been identified by calculating and comparing single parameter sensitivities of the K_d . UNiSeCs II is a further step towards establishing a set of common assumptions for the geochemical modelling of radionuclide partitioning in agricultural soils that can be applied to as many elements as possible. This will help to improve the estimation of radiation risk after radioactive contamination of the environment.

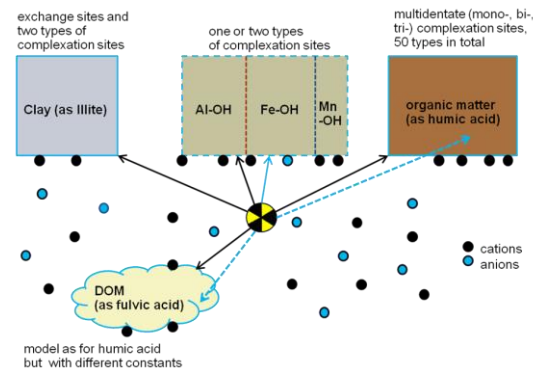


Figure 86: Conceptual model for the sorption of radionuclides in soil (DOM: dissolved organic matter). The solid arrows indicate surface sorption, the dashed arrows indicate covalent binding of elements like I or Se to organic matter (the latter processes are not included in UNiSeCs II)

This work has been submitted to the journal “Environmental Science and Pollution Research” and is currently under review.

This work was supported by the German Federal Ministry of Education and Research (BMBF) under grant FKZ 02NUK051D.

Link

<https://www.trans-lara.de/>

Reference

Hormann V, Modelling Speciation and Distribution of Radionuclides in Agricultural Soils. In: Walther C, Gupta D (eds) Radionuclides in the Environment. Springer, Cham, Switzerland.

https://doi.org/10.1007/978-3-319-22171-7_4, 2015.

Teaching activities

Annette Ladstätter-Weißemayer, Harry Küllmann, and Anja Gatzka

Today's graduate and postgraduate education in the field of Earth System and Environmental Science is a highly interdisciplinary and inter-institutional challenge. The existing research infrastructure at the University of Bremen (UB) and the Alfred Wegener Institute, Helmholtz Centre for Polar and Marine Research, Bremerhaven (AWI) offers a unique research environment in north-western Germany to study past, present and future changes of the Earth system. The education and qualification of Master and PhD students is carried out on an internationally competitive level.

Since 2000, the international Master program "Postgraduate Program Environmental Physics" (PEP) accredited by the German Accreditation Council is offered in collaboration with the AWI, Bremerhaven. Since its start, 138 students successfully finished this program with a Master degree, 15 with a Certificate. The foci of this program are on the atmosphere, ocean, land and climate as well as on remote sensing and dynamics.

In the winter semesters 2019/20 until 2020/21, 50 students started this study-program at the University of Bremen. The students came from Bangladesh, Egypt, Germany, Ghana, India, Iraqi, Italy, Nigeria, Pakistan and Singapore.

In 2006, a very successful collaboration between the University of Bremen and the Ocean University of China (OUC) in Qingdao/China started with the aim to offer Master double degrees of both universities. In this program, Chinese students start their studies in China, participate one year in the PEP program in Bremen and then complete their studies at the OUC. The German students start with one year at the OUC in Qingdao and then study one year in the PEP program.

In addition to these students, 29 so called Wahlfachstudenten from Physics, 31 from Space Sciences and Technologies, and 59 from Space Engineering are participating every year in the PEP program.

In the last 20 years, 69% of our students started - after finalising their master program or their Certificate - their PhD studies at the Institute of Environmental Physics in Bremen, the AWI in Bremerhaven or at another institution, while the remaining 31% applied directly for a job in industry or in climate or weather forecast related agencies.

As Bremen is one of the most important locations for aerospace in Germany, IUP and AWI together with partners from the departments of Electrical Engineering, Mathematics and Production Engineering from the University of Bremen set up a curriculum for an international Master program in Space Sciences and Technologies, which started in winter 2017/18. In the winter semesters 2019/20 until 2020/21, 72 Students from India, Pakistan, Iran, Sudan, Bangladesh, Mexico, Nepal, Germany came to the University of Bremen to study Space Sciences and Technologies – Sensing, Processing and Communication to get trained in experimental methods towards space applications, numerical data analysis and interpretation via sophisticated models.

In 2006 in the context of the excellence initiative, the Bremen International Graduate School for Marine Sciences GLOMAR was launched and funded by the Deutsche Forschungsgemeinschaft (DFG). This Graduate School is carried out with the following partners: University of Bremen, DFG Research Center Ocean Margin (RCOM), Center for Marine Environmental Science (MARUM), Research Center for Sustainability Studies

(ARTEC), AWI, German Maritime Museum (DMS), Max Planck Institute for Marine Microbiology, Center for Tropical Marine Ecology (ZMT). For excellent PhD students GLOMAR provides an optimal student research environment and fosters excellence in education and research. In general, the Graduate School's educational concept allows the PhD students to develop into excellent interdisciplinary researchers, with international contacts and a publication record in peer-reviewed international journals, skills in conducting research and in communication (on disciplinary and interdisciplinary levels to both experts and students as well as to the public), and in project management.

In 2009, the Helmholtz Graduate School POLMAR (Polar and Marine Research) started with the following partners: AWI (host institution), University of Bremen, Jacobs University Bremen, Max Planck Institute Bremen, University of Potsdam, Institute for Marine Resources (IMARE), and Hochschule Bremerhaven.

These programs enable PhD students from a variety of disciplines to cooperate and exchange views on the common theme of linking 'data and modelling', leading to a better understanding of local processes within a global context. It provides a structured framework for education and qualification for excellent PhD students dealing with the challenging questions in Earth System Science and Polar and Marine Research. Developing all categories of skills needed for analysing complex climate and environmental systems and the development of integrated solutions in a supportive network of collaborating research institutions fosters outstanding career options. Structured training and supervision supported by a broad range of soft skill courses is indicative for the entire concept. Up to now, more than 100 PhD students are within POLMAR.

The DFG funded German-Canadian International Research Training Group (IRTG) ArcTrain "Processes and impacts of climate change in the North Atlantic Ocean and the Canadian Arctic", which has been funded since 2013, is a consortium of scientists from the IUP (G. Spreen, J. Notholt, M. Rhein, M. Walter (co-speaker), D. Kieke), MARUM, the AWI and colleagues from 9 Canadian institutes. In 2017, the program was successfully evaluated and funding was assured until the end of 2022. Since 2017, 14 PhD students of the first two cohorts and three associated PhD students graduated successfully.

Since January 2016, the DFG is funding the Transregional Collaborative Research Centre TR 172 (AC³), providing a unique research environment to study the increase of Arctic near-surface temperature during the last decades, which is commonly referred to as Arctic Amplification, from complementary viewpoints, bridging various observations and modelling approaches. University of Leipzig, as the coordinating University has applied together with the University of Bremen (IUP: J. Notholt (co-speaker) and J.P. Burrows), University of Cologne and the Alfred-Wegener Institute for Polar and Marine Research (AWI), and the Leibniz Institute for Tropospheric Research (TROPOS) for support of this research project. In January 2020, the program was successfully evaluated and M. Rhein joined AC³. Funding is assured until the end of 2023.

The IUP Bremen regularly welcomes students from high schools in Bremen carrying out practical exercises. During these internships, the students have the opportunity to work in different research groups together with scientists for a time period of 2 weeks to get a first impression of research work.

In addition, the members of IUP are very active and involved in the "Day of Physics" and "Advents Physics" to give an insight into scientific work at IUP.



IUP Bremen Staff, December 2019 (credit: W. Gurlit)

Visit us on http://www.iup.uni-bremen.de/index_e.html